Residual stress development in a repaired welded connection

T.M.H. de Ruiter

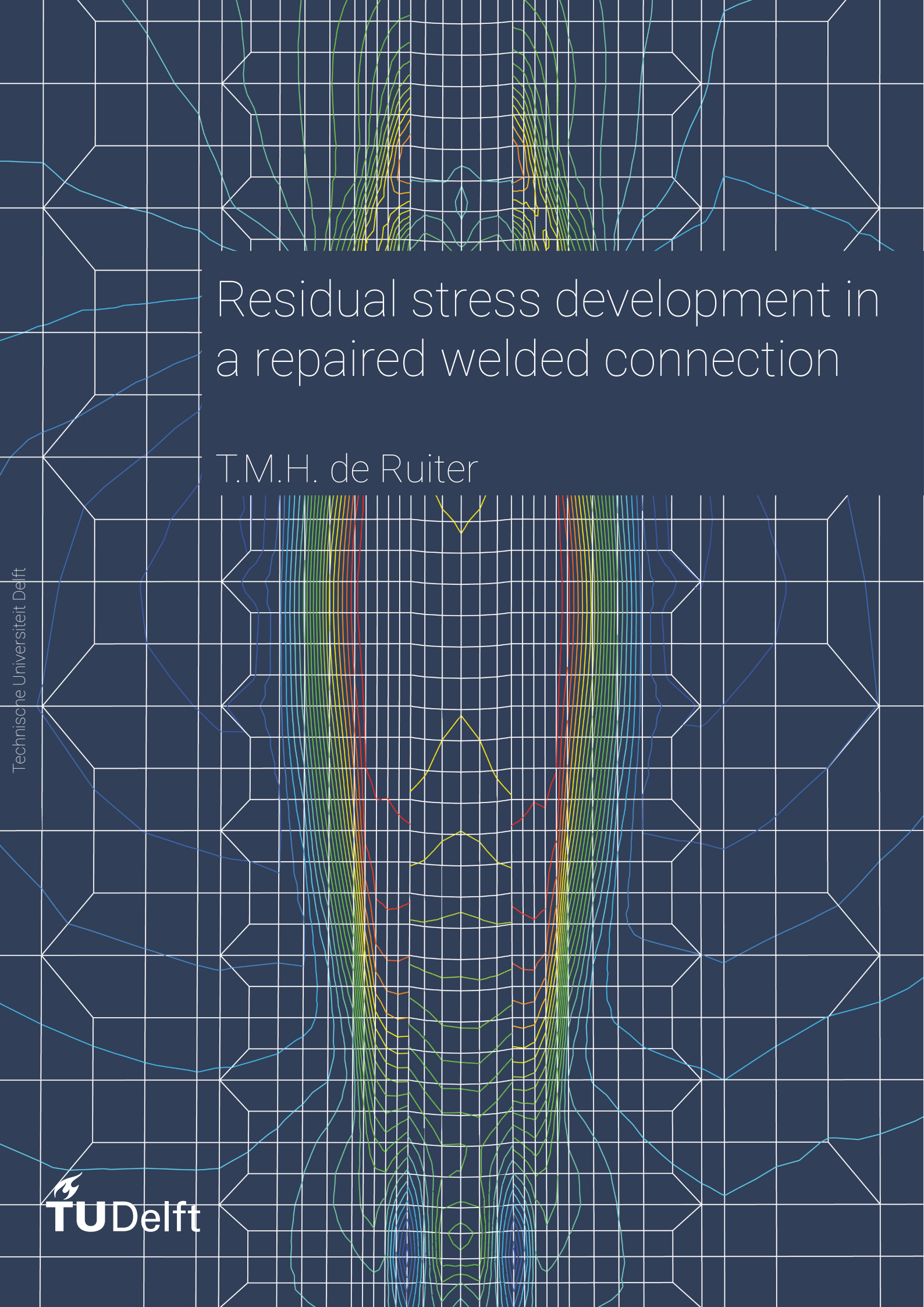

Technische Universiteit Delft

TU Delft

Residual stress development in a repaired welded connection

by

to obtain the degree of Master of Science
at the Delft University of Technology.
to be defended publicly on Friday February 24, 2017 at 16:00.

Student number:	4094999	
Thesis committee:	Prof. dr. M. Veljkovic,	TU Delft, Chairman
	ir. A. Akyel,	TU Delft
	dr. M.J.M. Hermans,	TU Delft
	dr. B. Hu,	Allseas Engineering B.V.

TU Delft

Contents

Abstract

Research shows that the fatigue strength of a Very High Strength Steel (VHSS) can be significantly negatively effected by welds in a structure. The fatigue lifetime may be extended after cracking occurs by means of fatigue crack repair. A better insight by means of Finite Element Modelling (FEM) can help in understanding the effects of a repair procedure in a welded connection which can results in the optimisation of the repairing process. The FEM model needs to be verified with experiment but measurement of residual stresses in a specimen requires either expensive or highly specialised equipment. Therefore, a more simple approach for model verification could aid in the accessibility of modelling of welding. The aim of this thesis is to establish a finite element model for a repair weld in a welded connection, and investigate to what extent the model can be verified by welding distortion.

A weld repair experiment, consisting of an initial weld, segment removal and repair welding, is performed to retrieve experiment data to be used as verification and input for the FEM model. First the modelling of the initial weld is described, consisting of a thermal analysis and subsequent thermo-mechanical analysis. Regarding the thermal analysis, a mesh sensitivity analysis is performed as well as 2D model results are compared with 3D results. The thermal analysis is performed by Goldak heat distribution and after calibration of the heat input, show a good agreement with temperature data retrieved from experiment.

Regarding the thermo-mechanical analysis, an Abaqus subroutine was established to retrieve information of the weld pool during the thermal analysis. This information is used in a subroutine during the thermo-mechanical analysis to assign different material behaviour to different elements of the weld, based on thermal history. In the thermo-mechanical model distortion results show a good agreement with experiment distortion results. As a result of unexpected movement during clamping of the experiment, calibration was required of the mechanical boundary conditions in the model to find matching results.

Modelling of the weld segment removal was performed, and similar trends of distortion between experiment and model results were found. However, further measurement of residual stresses is required to further evaluate the correlation between residual stress and distortion. Results of the thesis show that for a defect or faulty weld section, the measurement of the residual stresses is of great importance. Modelling of the full weld repair procedure proved to be beyond the scope of this thesis, since Finite Element work was more time consuming than initially anticipated.

1 Introduction

1.1. Project Background

Current developments in steel structures results in aesthetically pleasing designs while making optimal use of building materials [1]. Very High Strength Steel (VHSS) is an attractive answer to these modern Civil Engineer challenges as a result of its high strength-to-weight ratio, compared with steels of conventional strength. In the structure higher stresses can be reached, resulting in a reduction of steel volume. This can result in significant savings on material consumption, weight and transportation [2]. Furthermore, the production of VHSS has become more attractive as a consequence of the ongoing development in steel manufacturing processes as well. Within the field of Civil Engineering, actual application of VHSS is however limited since long term experience is lacking and guidelines for VHSS usage in structural application are also not extensively included in current design codes [3].

Research has shown that welding of a VHSS structural element has a significant negative effect on its fatigue strength [4, 5]. The fatigue strength of a welded joint is highly dependent on both local stress concentration and stress range. The negative effect on the fatigue strength can be explained by welding itself as this introduces not only local changes of geometry (affecting local stress concentration) but also tensile residual stresses causing an unfavourable shift of the local stress range. In addition, structural elements of VHSS are generally subjected to relative high stresses and stress ranges, as a smaller cross-sectional area is required compared to elements of conventional steel. The stress strange dominates the influence of geometry on fatigue of a connection [3].

Fatigue crack initiation in steel structures is unavoidable in a fatigue loaded structure [6], and in some cases, fatigue life extension can be performed by repairing fatigue cracks. The analysis of the residual stresses in a weld could aid in the understanding of this fatigue crack development. For this purpose, Finite Element Modelling (FEM) can help to simulate the residual stresses as a result of welding and a weld repair procedure. The effectiveness of fatigue weld repair methods on VHSS welded connections has been studied[1] and a better understanding of residual stresses by means of FEM could result in the optimisation of the welding repair procedure. This in turn can extend the fatigue lifetime of the structure.

[1] Research by Abdulkadir Akyel, PhD. candidate at the Civil Engineering Faculty of the TU Delft.

The residual stresses can be modelled by use of FEM, however the model needs verification by results from conducted experiments. The determination of residual stresses in an experimental set-up commonly needs highly specialised equipment and can be fairly expensive. Finding a more simple method of model verification could prevent the use of expensive equipment in the future.

1.2. Research Objective

The aim of this thesis is to establish a finite element model for a repair weld in a welded connection, and investigate to what extent the model can be verified by welding distortion. The process of a repair weld can be achieved by the following steps: the initial weld, removal of the defect and the execution of a repair weld.

This thesis is intended to provide a clear description of using the Abaqus software to model a residual stress distribution caused by a repair weld. In order to achieve this, the following three steps are taken:

First a single pass weld experiment is executed and is sequentially modelled in the Abaqus software. Measurement data is acquired through the experiment, which in turn is used to verify the modelling results. In relation to the model, the different aspects of the modelling process are explained to be able to evaluate the consequences of different modelling aspects.

The second step is the execution of the repair process. For this, a part of the weld material is removed and repair welded. Both activities are performed in an experiment and modelled through FEM simulation in the Abaqus software. The resulting outcome are compared and discussed.

1.3. General Outline

In Chapter 2, the origin, influence and measurement of residual stresses are discussed. This will give insight in why these stresses are important aspects in steel structures. Chapter 3 presents the properties and production processes of VHSS. Also, an overview of different general aspects of welding is shown, describing how the process works and the effects it has on materials used.

The initial weld experiment of this thesis is described in Chapter 4. The used material and welding set-up is discussed, including the data obtained from the experiment.

Chapter 5 presents different important aspects regarding the welding simulation in the Abaqus software environment. The influence parameters for a thermal and thermo-mechanical analysis are also discussed. In addition, thethe implementation of these parameters in the Abaqus software is discussed.

In Chapter 6 the simulation results are discussed and compared to the experimental results. Mesh sensitivity analysis and selected parameters are discussed as well.

Chapters 7 and Chapter 8 contain the experimental results of the repair procedure. Chapter 9 presents conclusions of this study and recommendations for future research.

2

Background Information

This chapter discusses the general information on residual stresses in a material. The residual stress definition, origins and significance are discussed. Finally different stress measurement methods are discussed in order to give a good overview of the different approaches which are available to retrieve experimental residual stress data from an experiment.

2.1. Residual Stresses

Residual stresses are stresses within a material which exists without the presence of any external loads [7]. The residual stresses within the material are self-equilibrating, the total sum of the stresses is equal to zero. Consequently, a combination of both compressive and tensile stressed zones are present in the material. Residual stresses can be presented at different scales, which can be classified in three different types (see Figure 2.1).

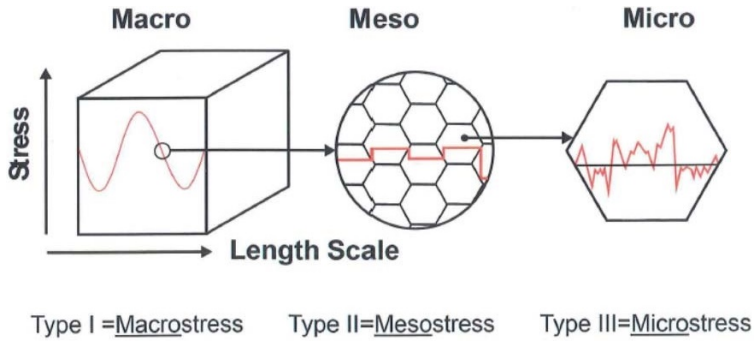

Figure 2.1: The different residual stress scales: Macro, Meso and Micro. [8]

A micro-stress distribution describes the stress present in one material grain, meso-stresses are represent the stress distribution between grains and macro-stresses specify the stress development between a multiple of grains [8, 9]. In a welded connection, stresses are generally regarded at macro-scale.

2.1.1. Origin of Residual Stresses

"Residual stresses are caused by the interaction of material elements within an object with the surrounding material." [9]. The state of this material element causes a shift in position of the surrounding material. The surrounding material reacts by exerting a force against this shift, trying to return to its original place. The different state of the material element, which generates the residual stress, can be induced by a thermal, mechanical or metallurgical process. Of the following phenomena at least one is present in every material or structure [8, 9]:

- Temperature gradients
  Large temperature gradients within a material can cause large residual stresses, in extreme cases even stresses exceeding the yield stress [8, 9]. High thermal gradients may cause residual stresses due to inhomogeneous thermal expansion, for example during a quenching process. During quenching, the surface of the material is rapidly cooled down, inducing thermal shrinkage. The relative large difference between shrinkage of the specimen surface and the material inside, induces compressive residual stresses within the material.

  Residual stresses can also be present when two components with a relative high temperature difference are connected. When these components are cooled down back to room temperature, a misfit due to thermal shrinkage can induce residual forces. A shrink-fit connection makes use of the friction caused by these force to connect different component with each other.

  The effects of temperature gradients of the residual stress state is highly apparent during and after a welding process. High temperatures are reached near the centre of the weld, but relative low temperatures are observable further from the weld. This causes locally for large amounts of plastic deformation, causing high residual stresses.

- Inhomogeneous phase transformation of the material
  Material microstructure can experience a phase transformation at specific temperature level. Consequently, the change of crystalline structure can induce a change of specific volume. However, the surrounding material restrains this volume change which induces residual stresses. Such phenomena can occur after rapid cooling of steel from a relative high temperature. For example during a quenching process.

- Mismatch of the thermo-mechanical properties
  When composite materials are used, a mismatch of thermal-mechanical materials is possible. For example, a volumetric mismatch caused by a thermal expansion coefficient can cause residual stresses when temperatures are changed.

- In-homogeneous plastic deformation
  Plastic deformation may occur as a result of externally applied load. During the service life of a structure this can be caused due to an (accidental) over-load. In some cases the production process induces plastic zones in a material, for example during the manufacturing cold rolled sections.

2.2. Significance of Residual Stress in Structures

The presence of residual stresses in a material can be important regarding the performance of structural members and connections. Several examples are presented in this section to give an insight of the importance of residual stresses.

The effect of these residual stresses can be favourable for parts of the section which act in compression and are susceptible for local buckling. For example, when a cold-formed section is produces, relative thin plates of steel are bend which induces plastic deformation of the section [10]. The effect of the plastically distorted sections on the whole cross-section can be significant. The plastic zone cause local work hardening of the steel, which increases the average yield stress of the section (See Figure 2.2).

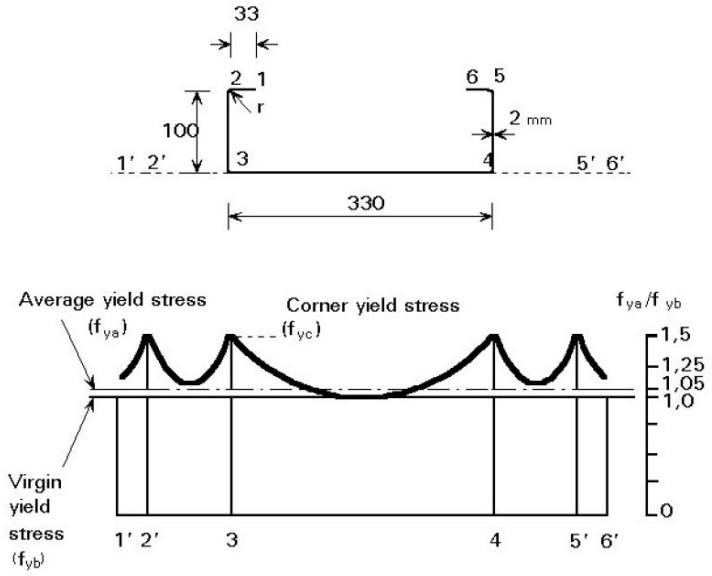

Figure 2.2: Yield stress distribution after introduction of plastic zones, compare to virgin material yield stress [10]

Residual stress of a welding process can cause a distortion of a section, which should be taken into account during production. Welding is a well-known source of residual stresses. The introduction of heat can cause residual stress development as a consequence of plastic zone formation, material phase transformation and large thermal gradients. Dependent on the material properties and specimen geometry this may induce (welding) distortions. Even large structure with small welds are susceptible for welding distortions. Relative small distortions of each weld can add up to a large amount of welding distortion at the end of fabrication.

The fatigue life of structure may be significantly varied due to the presence of residual stresses. Depending on the amount, direction and distribution of residual stresses the fatigue life can be increased or decreased [11]. Compressive residual stresses increase the fatigue life by reducing the tensile stress range. Tensile residual stress decrease the fatigue life by increasing the tensile stress range.

2.3. Residual Stress Measurement

Different residual stress measurement techniques are available. All measurement techniques are based on measuring strain in the material. The strain subsequently is related to the stress, which can be described for example in the elastic region by Hooke's Law ($\sigma = \varepsilon E$). The following techniques are used to measure the residual stresses on a macro scale (See Section 2.1).

2.3.1. Distortion Measurement Methods

Distortion based methods measure the distortion caused by the presence of residual stresses. Residual stresses can be derived by determination of the stresses needed for this distortion to occur. Distortion measurements can be performed by any distance measuring device, from a ruler (see Figure 2.3) to laser measurement. The choice of measurement method depends on the measuring accuracy required and the direction of the distortion: in two or three dimensions.

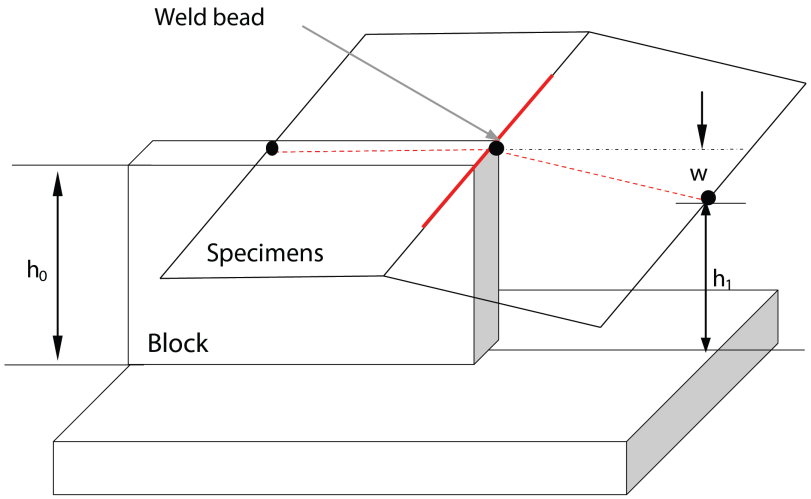

Figure 2.3: This set up is used to ensure a constant reference point while measurements are taken by a hand measurement tool (for example a calliper) [12]

A common and relative simple distance measurement method for a transient analysis is the Linear Variable-Differential Transformer (LVDT), see Figure 2.4. The LVDT is a mechanical device which converts displacement into an electrical signal. Because it is a mechanical device, frequency response during transient measurements is limited [13]. The LVDT has to stay in direct contact with the measured object and its measurable range of displacement is limited. Different sizes are available for different measurement. Deformation has to be estimated before the measurement, to make a correct decision on what size LVDT to use.

Laser displacement sensors (see Figure 2.5) are a more suitable solution for larger deformations, and for deformations which occur very rapidly, since accurate measurement can be made with smaller intervals, compared to the LVDT. A laser displacement sensor measures the distance to an object by recording the time it takes to reflect the laser beam back to the sensor. Laser measurements can be made over a distance of over one kilometre, but it can be limited due to local atmospheric conditions [17]. A distance varying from 4 to 2500 mm between specimen and laser source is required for exact measurements [16].

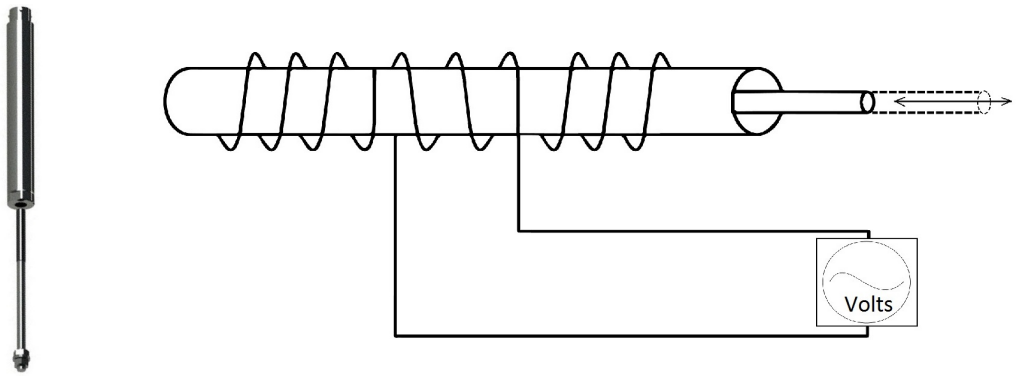

Figure 2.4: A LVDT and schematic representation of a LVDT measurement set-up. [14, 15]

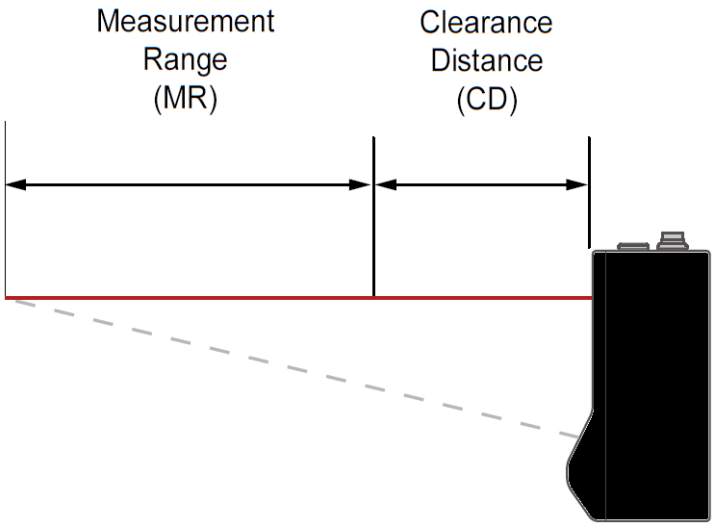

Figure 2.5: A laser distance sensor. Clearance Distance (CD) is the minimum distance needed for measurement. Measurement Range (MR) is the range at which the sensor can operate. [16]

An measurement accuracy can be achieved between ±0.0004 and ±0.06 mm dependent on the distance between laser source and the measured specimen. Either point measurement or 2D line measurements can be made [18]. If measurements are made during a welding process, adequate protection measurements have to be taken to protect the laser sensor from the light produced by the welding; this may compromise the laser measurement accuracy.

2.3.2. Optical Measurement Methods

An optical measurement method measures displacements and can determine the strain by evaluating the relative displacement of two or more points on a surface. Stereoscopic Digital Image Correlation (DIC) [13, 19] correlates the difference between photographic images to determine the relative displacements, see Figure 2.7. Distortion measurements of a larger field can be analysed in three dimensions by use of stereoscopic DIC. Both static and transient measurement can be performed. Different measurement accuracies can be achieved, dependent on the system used. For example, for DIC systems manufactured by Limess, measurement field size can vary from 1 mm^2 to large than 100 m^2. Displacement measurement precision is 100 points per pixel or 0.01 pixel. This relates to a displacement precision of 1 μm, using a measured distance of 100 mm with 1000 pixels evenly distributed over the distance ($0.01 * (100/1000) = 0.001\ mm = 1\ \mu m$). The precision of strain measurement is equal to 200 $\mu\varepsilon$ or 0.02 percent. For strain measurement at least two images are needed of the same specimen with the same reference points. [20]

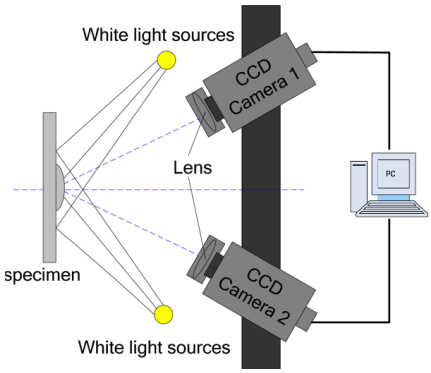

Figure 2.6: A schematic representation of a 3D DIC System [21]

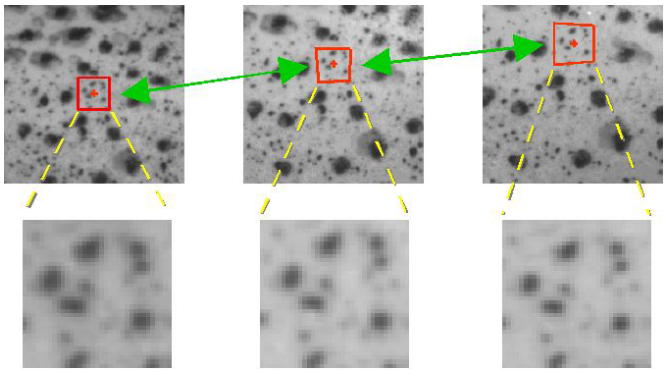

Figure 2.7: Pattern recognition of three different DIC measurement intervals, used to correlate the different images. [22]

A sufficient number and size of reference points are needed to correlate the images correctly, see Figure 2.7. Density and geometry of the reference points will determine the accuracy of the measurements, though the optimal reference point pattern can vary based on the data required from the DIC measurement [23]. A speckled paint pattern can be used to apply a field of reference points to a specimen. Care should be taken if the specimens are subjected to high temperatures; the applied paint could be affected by the heat. Special paints should be used for high temperature applications, such as ceramic paints [13]. When transient measurement are made during welding, special care should be taken to avoid direct or reflected light of the welding process. This light could affect the photo or video quality and consequently leads to inaccurate or useless measurements.

2.3.3. Relaxation Measurement Methods

All relaxation measurement methods rely on the measurement of deformation or strain change after a cutting or material removal process. These destructive methods base the residual stress measurement on the deformation measured, which are typically of elastic nature, and use Hooke's Law to compute the stresses released. For some methods and geometries, analytical calculations are sufficient for stress calculations, other methods need to be used in combination with finite element analyses, to (for example) relate deformation with stresses. The precision of measurement presented in this section are accuracy estimates of measurements taken of stress at ~ 50% of the yield stress. [24, 25]

Splitting Method

The splitting method is a more qualitative approach for residual stress measurement. A deep cut is made in the material, after which deformation due to the residual stresses will occur, see Figure 2.8. The direction and magnitude of the deformation gives an estimate of residual stresses size. A variant of the splitting method is Stoney´s Method. This method can describe the curling effect of thin plate materials, due to the addition or removal of material.

The splitting method is a relative rough measuring method with a precision of 20 to 50% at ~ 50% of the yield stress, and it is generally highly destructive due to the cut depth penetration of the full specimen thickness. Advantages of the method are the quick use and relative cheap costs. However, it provides a relative rough measurement, consequently the method is best used in routine quality control applications.

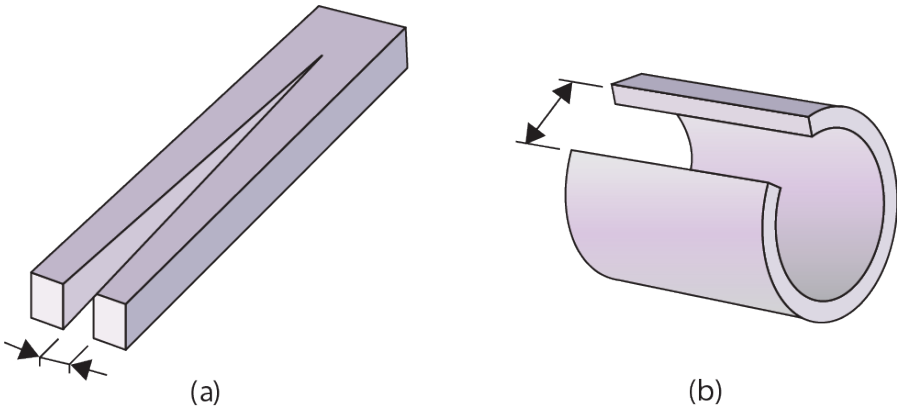

Figure 2.8: The Splitting Method applied to a rod (a) and a tube (b) specimen. [24]

Section Method

For the sectioning method, strain gauges are used to measure the relaxation due to the removal of parts of a section (see Figure 2.9). By cutting the cut surfaces, further information about the residual stress development in the original section is obtained.

This method is a highly destructive measurement technique. It can provide quantitative stress measurements at a precision of 10 to 30% at ~ 50% of the yield stress. Calculation of the stresses may prove to be challenging, especially when many sections in different directions are made. Consequently, this method is best applied on specimens of regular-shaped geometries, for example an I-beam section.

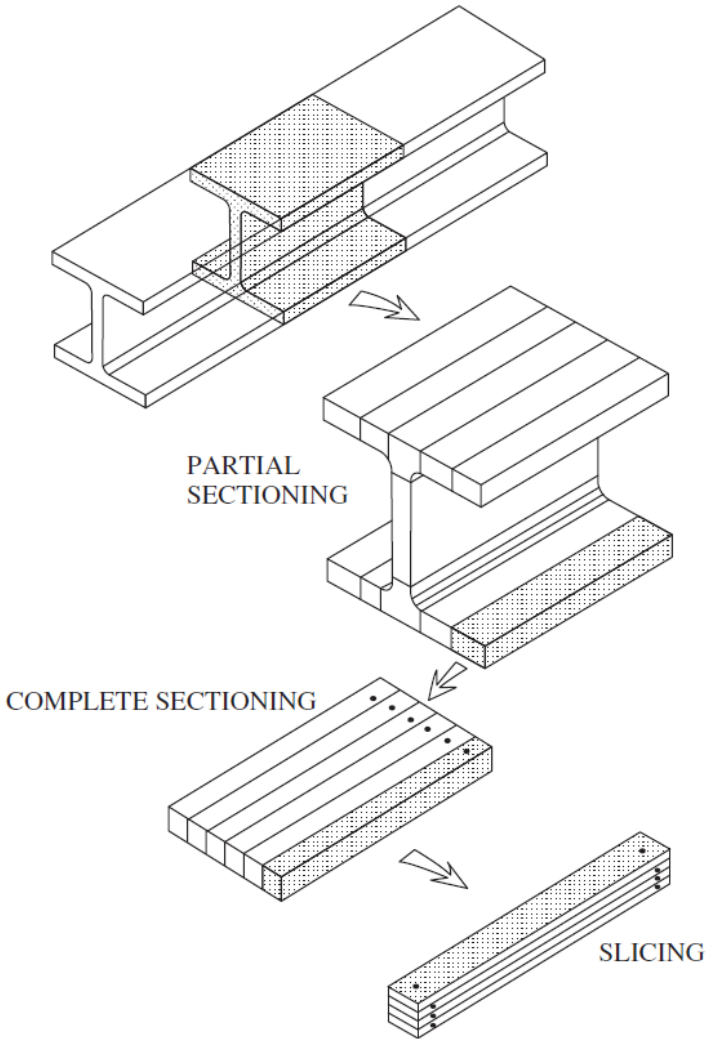

Figure 2.9: The sectioning method at different levels, creating each time smaller specimens. [26]

Layer Removal Method

The layer removal method involves the removal of layers of material, parallel to the measured surface. Strain gauges measure the relaxation due to the removal of each layer, starting with the layer furthest away, see Figure 2.10. A variant of the layer removal method is the Sachs' Method, which is the layer removal method applied on a cylindrical specimen.

For full stress measurement of the specimen, the full thickness of the section has to be removed, making this method fully destructive. This method can achieve a precision of between 10 to 30% at ~ 50% of the yield stress, but is time consuming and measurement drift may occur. It is best suited for specimens of uniform thickness, flat plates or cylinders.

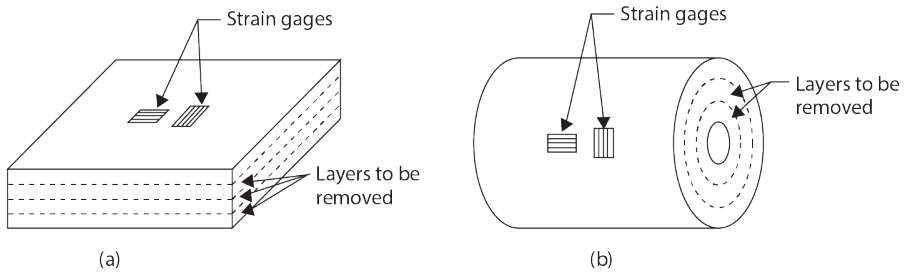

Figure 2.10: The Layer Removal Method for a flat (a) and cylindrical (b) section. [26]

Hole-Drilling Method

Hole-drilling involves the evaluation of in-plane stress relaxation through strain measurement around a drilled hole, see Figure 2.11(A). A rosette strain gauges is used to measure the strain in multiple directions. Rosette strain gauges are multiple gauges situated close to each other and in different directions. The maximum hole drilling depth is approximately equal to the hole diameter size.

Measurement penetration depth is typically up to 2 mm. Consequently, this method is best used for near surface uniform stresses. Measurements may have a precision of 10 to 20% at ~ 50% of the yield stress, but local yield due to the hole drilling limits the specimen maximum stress level of 70% of the yield [25].

Ring Core Method

The ring core method is comparable to the hole-drilling method, but involves drilling a ring and measuring the relaxation of the material located in the ring, see Figure 2.11(B). The relaxation is measured by rosette strain gauges. The ring core method allows for larger strain measurements, relative to the hole-drilling method.

A common measurement penetration depth is 5 mm. Compared to the hole-drilling method, the measurements are generally less sensitive for errors caused by milling or temperature differences [27]. Additionally, relative larger strain and stress values can be measured, stresses up to the yield stress of the material. Application of the ring core method is more difficult and will cause more damage to the specimen, compared to the hole-drilling method.

Deep-Hole Method

The deep-hole method combines aspects of the hole-drilling and ring core method. A deep hole is drilled, after which a ring core around the hole (over-cored) is made. The geometric changes caused by the second ring core are measured within the first hole (see Figure 2.11(C)). This method is used when a large penetration depth is required.

Stress measurements can be made with a precision of between 5 to 15% at ~ 50% of the yield stress, at depths up to the specimen thickness, which makes it more suitable for large specimens. Disadvantage of the method is the relative low speed and the need of a measurement specialist.

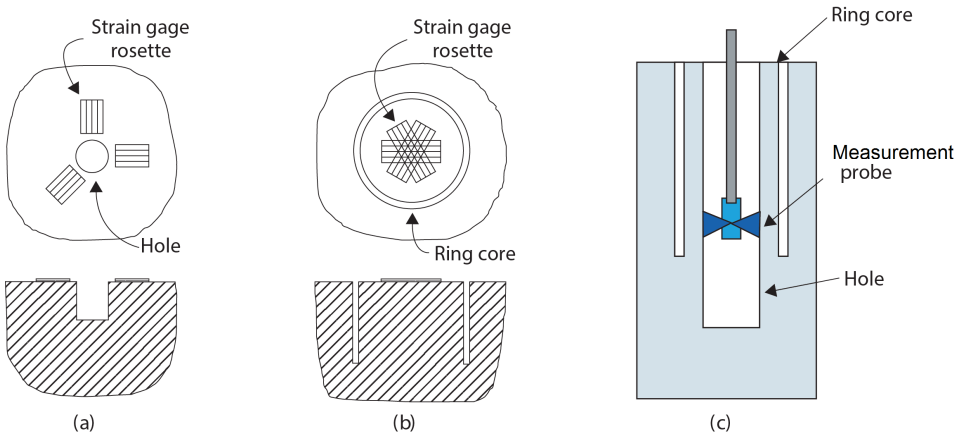

Figure 2.11: A schematic representation of the Hole-drilling Method (a), the Ring Core Method (b) and the Deep-Hole Method (c). [24]

Slitting Method

The slitting method involves cutting a long slit, rather than drilling a hole. Strain measurement perpendicular to the slit direction are taken to measure the relaxation. With the slitting method strain measurement can be made further from the slit, at the other side of the material, this way strain profile over the depth can be obtained (see Figure 2.12).

This method may provide measurements of a precision between 5 to 20% at ~ 50% of the yield stress. A uniform stress distribution over the width of the slit is. Generally, because of the slit size, damage inflicted by the measurement method is relatively high.

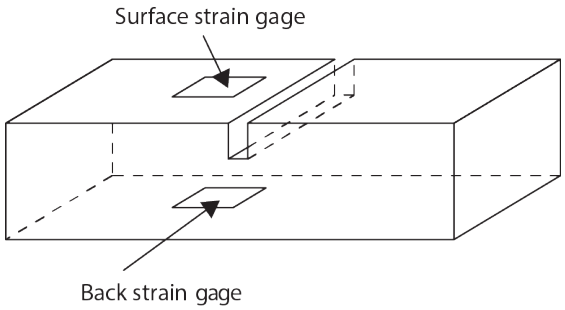

Figure 2.12: A schematic representation of the slitting method applied to a specimen. [24]

Contour Method [28]

For the contour method a cut is made by Electrical Discharge Machining (EDM) in the material. The two formed cutting surfaces will deform due to the presence of residual stresses. Stress measurements are made by measuring the contour of the cutting surface and calculating the forces needed to push the material back (see Figure 2.13). This can be done either by analytical or numerical calculations.

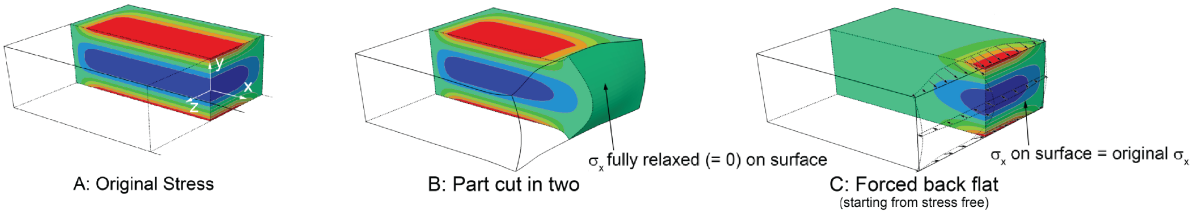

Figure 2.13: An initial stress before cutting is regarded (A). The specimen is cut, allowing for elastic relaxation around the cutting surface (B). Push back of the relaxation deformation induces stresses in the material (C). [24]

This method requires to cut the specimen through the whole thickness, which makes the method fully destructive. A precision may be reached between 5 to 20% at ~ 50% of the yield stress, but it needs an accurate cut of the cross-section too achieve accurate and undistorted deformation measurements.

2.3.4. Diffraction Methods

Diffraction methods measure with electromagnetic radiation the distance between atomic planes of a crystalline or polycrystalline material. The interplanar dimensions are related to the size and direction of the stress in the material. [24, 25]

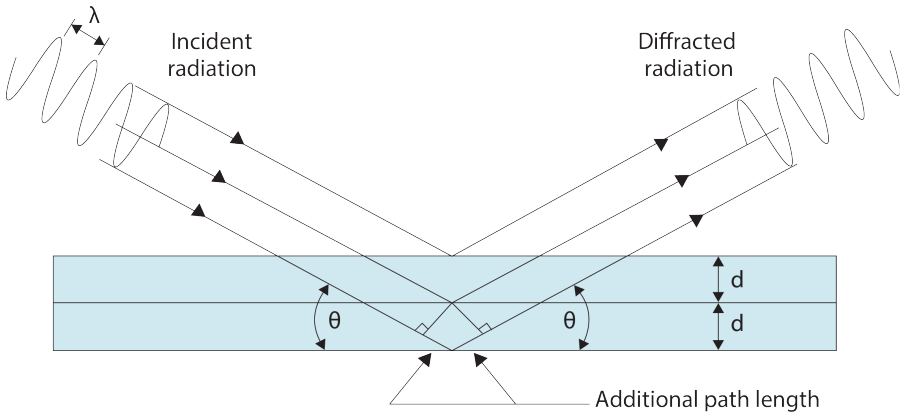

Figure 2.14: A schematic representation of the diffraction of radiation at a Bragg-Angle θ, wavelength λ and the distance between lattice-planes d. Where $2d\sin\theta = n\lambda$ describes the relation between these factors. [8, 24]

Both X-ray and neutron diffraction methods use the same concept to measure diffraction intensities. Electromagnetic radiation is applied at a range of angles relative to the surface, measuring the diffraction radiation (see Figure 2.14). The diffracted radiation will vary in intensity dependent on this angle (see Figure 2.15). The Bragg is the certain angle at which the highest diffraction inten-

sity is measured. Strains between lattice structures can be calculated based on the Bragg angle and radiation wavelength.

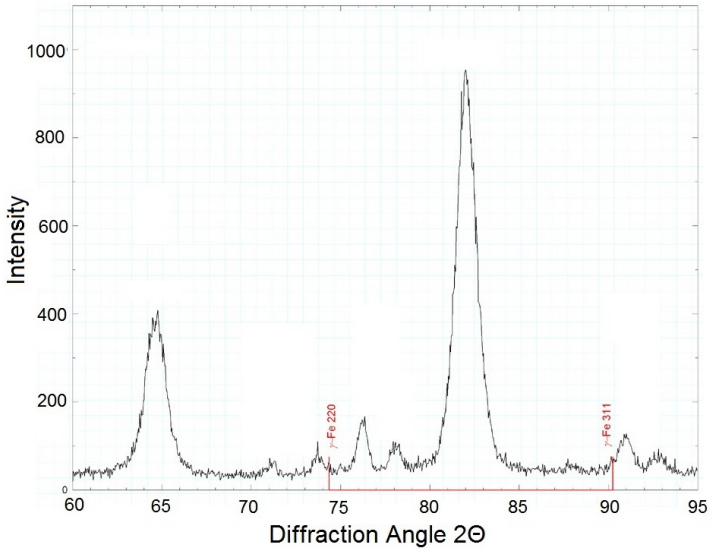

Figure 2.15: An example of results of X-Ray diffraction measurements of a 440C alloy steel. Diffraction intensity is represented as a function of the Bragg angle. [29]

- **X-ray Diffraction**
  X-ray diffraction uses X-rays to penetrate the material and measure the diffraction. X-ray penetration is limited to an order of 0.025 mm, which makes X-ray diffraction to be known as a surface stress measurement method. Due to its shallow depth measurements, stresses normal to the surface are assumed to be zero. Therefore, the measured stress values are considered as plane stresses, which allows for simplified calculations. The stress measurements have the significant advantage of measuring stresses without the need of an initial stress state; the measured values are relative to a zero-strain condition. Measurements can be done in seconds and spatial resolution can be less than one square mm.

- **Synchrotron X-ray Diffraction**
  Synchrotron X-ray diffraction uses more intense and higher energy X-ray radiation to penetrate the material. This allows for a penetration depth in orders of mm. Due to the larger penetration depths, a plane stress approach cannot be used, consequently a three dimensional stress state has to be studied. An un-stressed lattice is required as a reference, this may cause measurement uncertainties. Measurements can be performed in milliseconds and spatial resolution can be of cubic μm range.

- **Neutron Diffraction**
  Neutron diffraction interacts with the nucleus of the atom, allowing for relative deep penetration. Penetrations can be in the range of $0.1 - 1.5\ m$. Similar to the synchrotron diffraction, when using neutron diffraction stress in three dimensions need to be considered. Again an un-stressed lattice is required as a reference. Measurements can be performed in several minutes to over an hour and spatial resolution can be of cubic mm range.

The high advantages of the diffraction methods above almost all other stress measurement method is its non-destructive application. Measurements can have a precision of between 20 to 50 N/mm^2.

Highly specialised equipment is needed to perform measurements, consequently costs are relatively high. Maximum specimen size can be limited by the equipment used for the measurement.

2.3.5. Other Measuring Methods

These methods use the change of property of a material due to the change in strain. Generally these method are not used for quantitative measurement.

- **Magnetic Method**
  The magnetic residual stress measurement method relies on the re-orientation of magnetic domains during a magnetization reversal. Stress measurements are limited to a range of $\pm 300\ N/mm^2$ and are dependent on calibration with a near identical specimen, which restrict the reliability of the method. Measurements can be done in several seconds and spatial resolution can be of below mm range.

- **Ultrasonic Method**
  The ultrasonic method measures how ultrasonic waves are affected by the material. Uncertainty of measurements are caused by other effect, other than residual stresses, which affect the waves like grain size and steel texture. Measurements can be done in seconds and spatial resolution can be of a several cubic mm range.

- **Thermo-elastic Method**
  Measurements are based on the rate of temperature of the material. The thermal reaction of the material is affected by elastic strain, creating small changes in infrared emission of the heated material. The change in thermal behaviour is very small, so thermo-elastic measurements are used for qualitative, comparative purposes.

- **Photo-elastic Method**
  Otherwise known as the birefringent method, this measurement method relies on the diffraction of polarized light through an transparent material. Different diffraction will cause light to shift in colour, making strain fields viewable to the naked eye.

- **Indentation Method**
  Residual stresses have a slight influence on material hardness and can be measured by hardness indentation tests. Though research has been done to improve upon getting quantitative results, accuracy is presently still relatively low. Measurements can be done in several minutes and spatial resolution can be of below square mm range.

3

Material and Welding

3.1. Material

Steel micro-structure has to be altered in order to increase its yield strength. With several processes the increase of strength properties can be achieved, although each process has its own specific effects on other material properties. It is important to realise what some actions on the material can induce. For example, inducing high temperatures to the steel can change the micro-structures. As a consequent, welding can have a significant effect on the material properties.

For this research the term high strength steels (HSS) and very high strength steels (VHSS) have to be defined since an accredited terminology and strength range has of yet not been established. Steel of a yield strength between 235 and 460 N/mm^2 is referred to as conventional or mild strength steel. The term high strength steels will be used for steels exceeding a minimum yield strength of 460 N/mm^2. The term for very high strength steels will be used for steel exceeding a minimum yield strength of 690 N/mm^2.

3.1.1. Micro-structure

The micro-structure of steel depends mainly on the carbon weight content, current material temperature and temperature history [30]. The different micro-structures as a function of the material temperature and carbon weight content is shown in the iron-carbon equilibrium phase diagram (see Figure 3.2). This diagram shows the different stable phases of steel. The main stable solid phases of steel are ferrite (alpha-iron), austenite (gamma-iron), cementite (Fe_3C) and graphite.

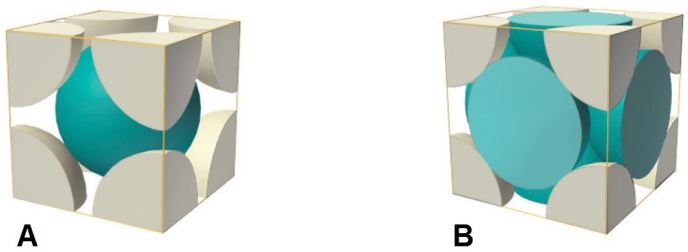

Figure 3.1: A) Body-centered cubic (bcc) atomic arrangement. B) Face-centered (fcc) atomic arrangement. [31]

Ferrite consists of a tightly packed all-iron atom structure in a body-centered cubic (bcc) crystalline arrangement (see Figure 3.1). This is a tight structure, therefore carbon solubility is very low, consequently an all ferrite steel can only be manufactured when very low amounts of carbon are present. When the ferrite is oversaturated by carbon, an iron-carbon compound can be formed called cementite. Cementite is a hard and brittle material, and it will decompose into graphite over time. However, decomposition develops slowly and it can be considered as a 'near equilibrium' phase, which in practice is sufficiently stable [30]. A material with an only cementite micro-structure will only be able to be produced at a carbon content of above 6.7 percent, a carbon content that will never occur in steel manufacturing.

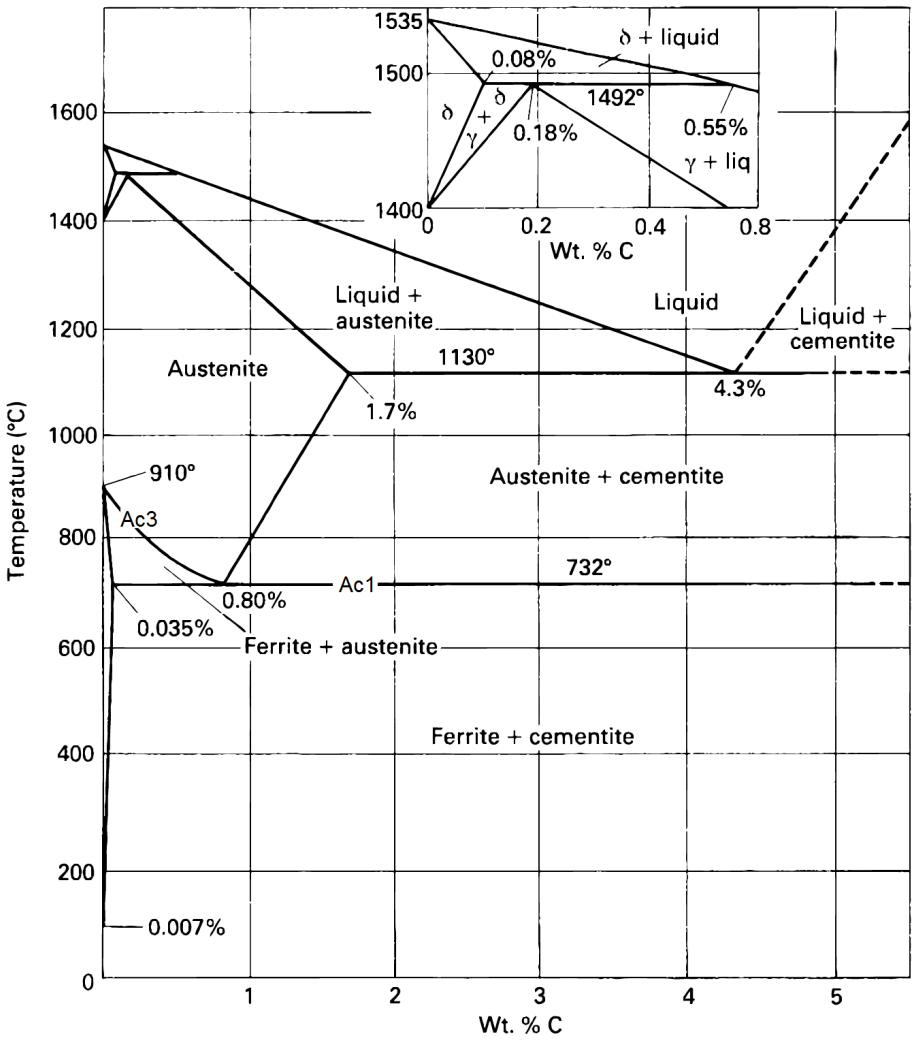

Figure 3.2: Iron-carbon phase diagram [32]

The final stable micro-structure is Austenite. Austenite can only form, in the case of normal steel, above the transformation temperature Ac_3 (at ±732 °C). The austenite micro-structure allows for a higher solubility of carbon, due to larger interstices in the face-centered cube (fcc) structure (see Figure 3.1). During the production of structural steel, an austenite structures is formed to allow for fast carbon diffusion, consequently forming a more homogeneous micro-structure. After cooling this can improve material properties by the resulting homogeneous and fine grained micro-structure. [30]

Fabrication of a homogeneous steel only consisting of a micro-structure of ferrite, cementite or austenite, does in practice not occur. In order to produces such single-phase materials, specific manufacturing conditions are required. Temperatures have to remain constant, or heating and cooling has to happen very slowly during the manufacturing process. Practical fabrication of the steels do not allow for these stable phase to be homogeneously present. Instead metastable phases are formed because of the relative fast heating and cooling rates [30]. Metastable phases are pearlite, martensite and bainite. Pearlite is a specific combination of ferrite and cementite, as an effect of a faster cooling rate of an austenite structure during the manufacturing process. Laminar strips of ferrite and cementite are present in the grains and increases strength but causes poor toughness.[33]

A martensitic structure can be created by relative fast cooling of an austenite structure. The fast cooling prohibits the carbon to diffuse out of the formed ferrite structure. Those carbon atoms remain in a ferrite structure, which causes a distortion, transforming it into martensite. Martensite is a very hard structure and has a very high ultimate tensile strength, but behaves in a brittle manner. [34]

Bainite is formed when cooling rates are not fast enough to form martensite, and not slow enough to form pearlite. The structure is comparable to pearlite, a combination of ferrite and cementite is present, but shapes of the phases are different. The ferrite has an acicular (needle-like) structure, while in pearlite this is a lamellar structure. Cementite is present in discrete form, rather than the laminar form in pearlite. These difference in micro-structures morphology causes the bainite steel to have a high strength, with good toughness.

To impose the formation of particular micro-structures, heat treatments as normalizing, thermo-mechanically rolling and quench and tempering are applied, see Figure 3.3 for a visual representation:

- Normalizing steel consist of heating the steel to a temperature just above the austenitizing temperature (Ac_3), followed by air cooling. The high temperature allows faster carbon diffusion in the material, allowing a more homogeneous austenitic micro-structure. Once the steel is cooled, the austenitic structure will have changed to a more fine ferrite and pearlite microstructure, improving overall material properties. [30] A normalizing process can increase the yield strength of steel up to 460 N/mm^2.

- Thermo-mechanically rolled steel consist of hot rolling the steel during the cooling process, at temperature lower than the conventional steel rolling process (lower than 900 °C) but above 700 °C. The still high temperature allows a more homogeneous micro-structure, similar to the effects during normalizing. The hot rolling causes the austenite grains to stretch and when cooled, the grains change to a fine, predominantly ferrite structure. The thermo-mechanically rolled steels have yield strength ranging from 355 to 700 N/mm^2.[35]

- Quenched and tempered steel consists of heating the steel above austenitizing temperature, Ac_3, followed by rapid cooling. After this process the steel is tempered, which is heating the steel just below Ac_3 and cooling it down, to reduce hardness and increase toughness. To ensure proper hardening of the material during the rapid cooling, chromium, molybdenum or nickel has been added to the steel alloy. Quenched and tempered steels have a yield strength ranging from 690 to 1300 N/mm^2.[30, 36]

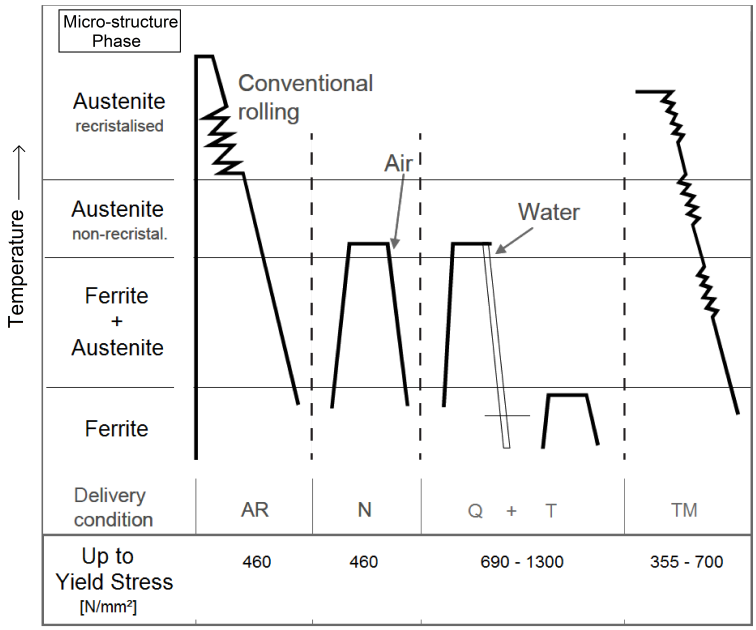

Figure 3.3: The different manufacturing process for conventional and higher strength steels. AR is a conventional or 'as rolled' process. N is a Normalizing Process, $Q+T$ a Quenching and Tempering process and TM a Thermal-Mechanical rolling process. [37]

3.1.2. Conventional Steel

To create steel products of conventional strength generally semi-finished steel products like blooms, billets or slabs are heated to above their recrystallisation temperature, followed by a rolling process [30]. The elevated temperature allows the steel to recrystallise after working the metal, minimising negative effects like strain-hardening and non-constant plastic flow. To achieve a higher yield strength than 460 N/mm^2, different material and manufacturing processes have to be applied.

3.1.3. Higher Strength Steel

To increase yield strength while keeping a sufficiently ductile behaviour, primarily two choices have to be made: choice of manufacturing treatment and chemical composition of the steel [35]. The most important treatments are normalizing, thermo-mechanical rolling, and quenching and tempering. At the same time chemical composition of the steel is thoroughly controlled, this way the effects of treatment on the steel can be adjusted. The different manufacturing processes will change the micro-structure of the steel; decreasing grain size and consequently altering its properties. In general, a decrease in grain size means an increase in strength and good toughness. This correlation between grain size and yield strength is described by the Hall-Petch relationship (equation 3.1):

$$\sigma_y = \sigma_0 + \frac{k}{\sqrt{d}} \tag{3.1}$$

where σ_y is equal to the yield stress, σ_0 a material constant for the stress at which dislocation movement starts, k a material dependent Hall-Petch coefficient and d the average grain diameter [38]. It should be noted that due to lack of a clear transition from elastic to plastic behaviour in higher strength materials the yield strength has been specified as the offset yield strength, also known as the 0.2 percent proof strength. This is the stress of which after relaxation a plastic strain deformation remains of 0.2 (see Figure 3.4).

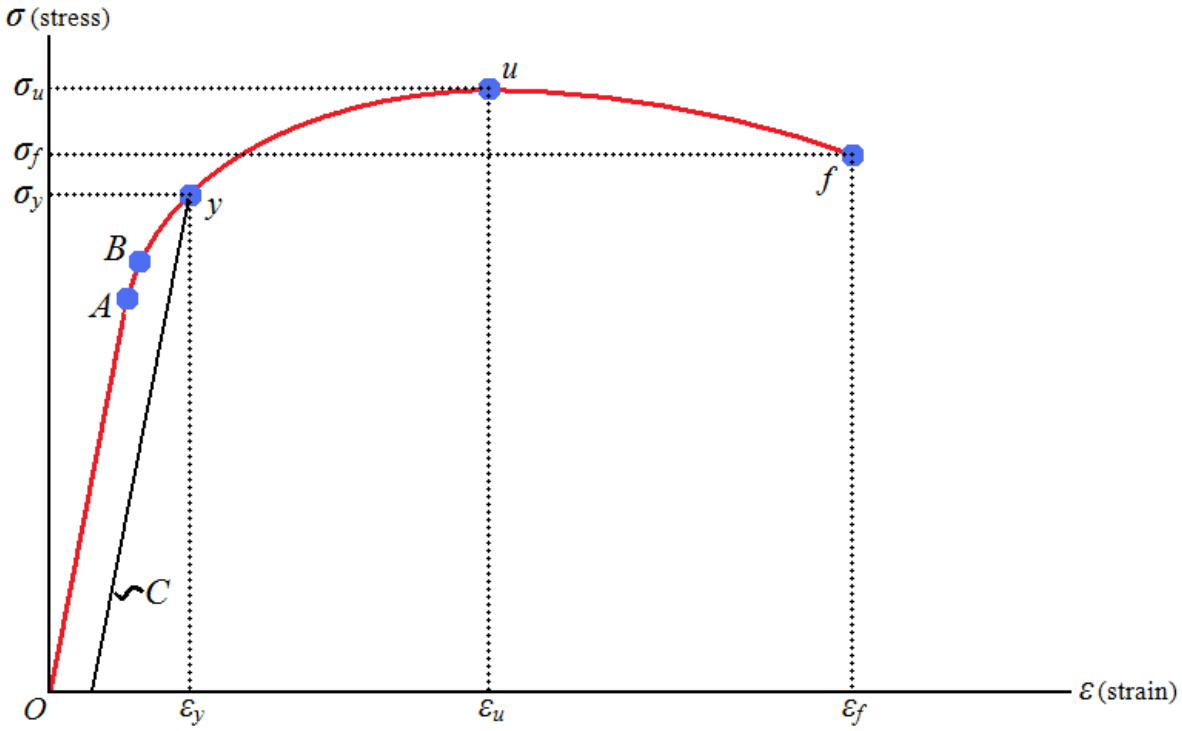

Figure 3.4: Stress strain relationship of high strength steel. *A* is the proportionality limit, *B* is the elastic limit, *y* the yield point. Line C indicates the point of 0.2% strain for yield point *y*. [18, 39]

3.2. Welding

Welding is a localised joining technique which makes use of material fusion to bond two materials together [40]. It is performed by applying heat, with or without pressure and with or without a filler material. The most common welding processes make use of the liquid state of the material. The liquid materials mix and fuse together, consequently forming a strong bond after cooling. Different welding processes such as arc welding, gas welding, resistance welding, laser welding and solid-state welding are available. Arc welding is the most common welding practice used in steel structures, and is therefore further discussed in this section.

The arc welding process makes use of a high energy electric arc to melt the different materials. The welded workpiece is connected to the welding equipment, so that a closed circuit can be formed between the welding electrode and the welded material. The circuit is closed by forming the arc between the welding gun electrode and the welded material. An welding arc is formed between an electrode and the welded workpiece when a sufficient amount of energy is available [8, 41]. The high energy causes the ionisation of the gasses between the electrode and workpieces, which creates free electrons. The free electrons provide conduction of the energy, making the formation of the arc possible. [40]

3.2.1. Gas Metal Arc Welding

A very common arc welding method is Gas Metal Arc Welding (GMAW), which is subdivided in Metal Inert Gas (MIG) or Metal Active Gas (MAG) welding. It is a common method because of a relative fast application and is able to perform large continuous welds, by manual or mechanical application [40]. The welding arc is formed between the base metal and the automatically fed welding wire, which acts as the electrode. The consumable is automatically fed through the welding torch as depicted in Figure 3.5.

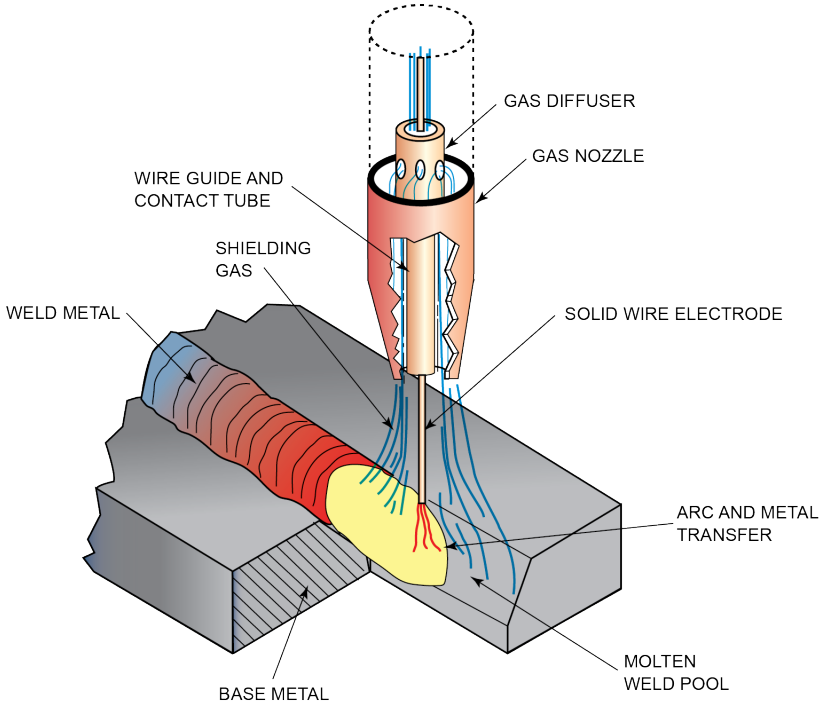

Figure 3.5: Cut-out of a GMAW nozzle during welding and feed-through of the electrode. [40]

Two main types of welding wires are available for the GMAW welding. The wire can either be a solid metal or may contain powder core such as a flux-cored or metal-cored wire. In case of necessity, a shielding gas can be used during the welding process. Commonly a mix of an inert gas (for example Argon) and a limited amount of active gas (oxygen, CO_2) is used as shielding gas. The gas stabilises the arc, limits weld spatter, and reduces external contamination of the weld [41]. The exact composition of the shielding gas depends on the filler wire and welded material. The advantage of using the powder cored wires is that the composition of power can relatively easily be altered during manufacturing. It can provide, for example, material to form a protective slag on the weld during welding.

Two main types of weld material transfer modes can be distinguished when applying GMAW; short-circuit welding and open-arc welding [8, 40]. During short-circuit welding the electrode short-circuits while material transfer occurs, which causes the arc to extinguish (see Figure 3.6). Consequently, short-circuit welding introduces a relative small heat input, which makes it suitable for thin sections and root welds of multi-pass welding. The disadvantage of the low heat input is the higher risk of lack of fusion. Furthermore, during this process relative more spatter can occur. Open-arc welding uses a higher heat input and consequently forms a larger weld pool area. Welding metal is transferred by metal droplets, known as globules. When current increases, the globules will decrease in size. If current is further increased, globule size will decrease further, eventually forming a vaporized spray of metal. Usage of open-arc welding is limited to thicker workpieces (above 8 mm) and the position of the weld. For example, welding upside down with a large weldpool is not possible without precautions, since the weld metal may flow out of the welding area.

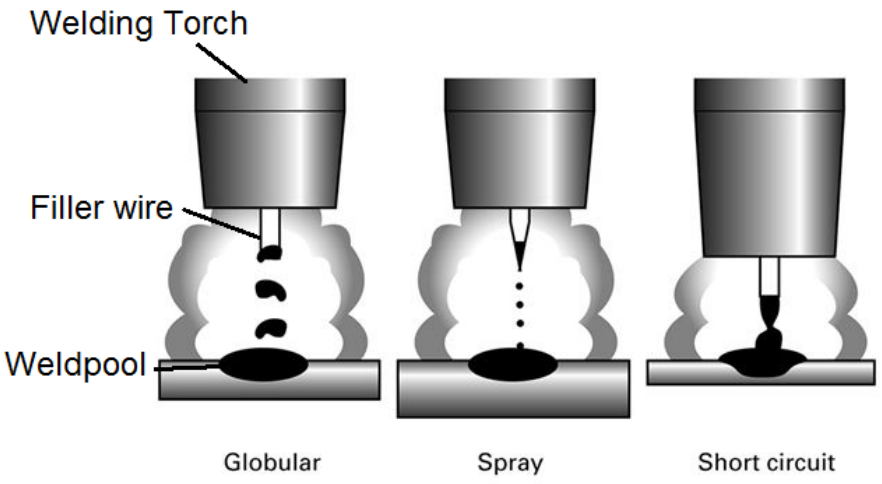

Figure 3.6: Three types weld metal transfer. [42]

3.2.2. Constrainment during Welding

In some cases, the welded workpieces need to be clamped before welding. The purpose of constrainment is to prevent movement of the pieces during the welding process. The clamping provides the advantage to keep the distance between workpieces constant and avoid large deformation at the welding location. Consequently it provides good conditions for continuous welding.

If a workpiece is not sufficiently clamped, two main types of welding distortion can occur: out-of-plane distortion and in-plane distortion. Out-of-plane distortion can be caused by three distortion mechanisms (see Figure 3.7: C, D and F). The first can be caused due to transverse shrinkage of the weld which cause an angular distortion. The second causes bending of the plate due to the build-up of longitudinal stresses. The third and last out-of-plane distortion may be caused by plate buckling due to the longitudinal stresses.

In-plane distortion can be caused by longitudinal, transverse and rotational distortion of the plate (see Figure 3.7: A, B and E). Longitudinal in-plane distortion is caused due to the shrinkage of the weld in longitudinal direction. Transverse stresses cause a similar behaviour but in transverse direction. Rotational distortion can be caused due the partial build-up of stresses during welding. Consequently, the specimen may rotate in-plane.

Removing constrainment after welding may have a significant effect on the deformation. Not only due to the relaxation of stresses but also due to a possible buckling behaviour of the clamping [19, 43]. The deformation after unclamping should be taken into account when a clamping system is designed.

The constrainment hinders deformation of the workpiece, which causes high plastic strains in the molten material. This will result in higher residual stresses. Vice versa, lowering the constrainment will result in lower residual stresses but higher distortions during welding [43].

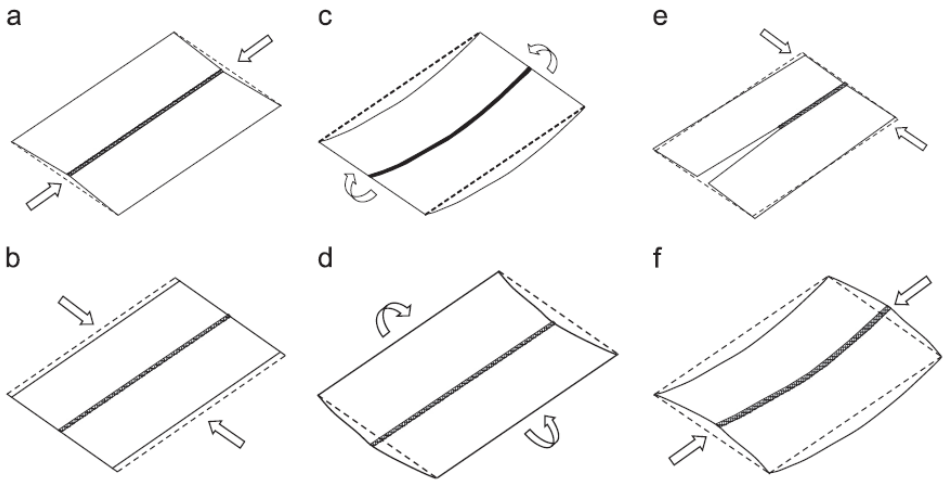

Figure 3.7: Different forms of out-of-plane and in-plane welding distortion. A) Longitudinal in-plane distortion. B) Transverse in-plane distortion. C) Bending out-of-plane distortion. D) Transverse angular out-of-plane distortion. E) Rotational in-plane distortion. F) Buckling distortion. [44]

3.2.3. Residual Stress formation in a Welded Connection

As stated in Section 3.2.2, constrainment of a workpiece during welding will increase the residual stresses in the specimen. The effect of constrainment and the overall effect of residual stresses in a welded plate can be demonstrated by the use of a three-bar system [8, 43].

The three-bar system demonstrates the elastic residual stresses formed by partial heating of the system. The system describes the stress distribution in longitudinal direction of the weld. Three bars are of equal size and are connect by two rigid transfer bars, see Figure 3.8:

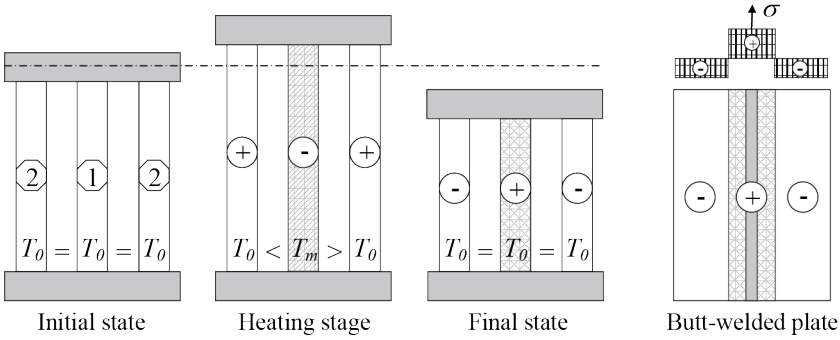

Figure 3.8: The Three-bar analogy system, in which the system resembles an temperature cycle of a Butt-welded plate [43, 45]

During the heating stage only the middle bar is exposed to a heat source, which causes thermal expansion according to

$$\frac{\Delta l}{l} = \alpha \Delta T \tag{3.2}$$

where Δl is the length increase and l the length of the element. α is the thermal expansion coefficient of the material and ΔT the temperature increment. Because of the rigid interconnection of the bars, lengths of the bar should be kept equal. Consequently, strains should be kept in equilibrium, which leads to a stress equilibrium as equation 3.3:

$$\sigma_1 = 2\sigma_2 \tag{3.3}$$

where σ_1 is the stress in bar one and σ_2 the stress in the bars two. The strain caused by the thermal expansion of the middle bar are imposed on the outer bars. The strain equilibrium of the system can be expressed as:

$$\frac{\sigma_1}{E(T)} + \alpha \Delta T + \frac{\sigma_2}{E(T_0)} = 0 \tag{3.4}$$

where $E(T)$ is the modulus of elasticity at temperature T and $E(T_0)$ the modulus of elasticity at room temperature. By rewriting equation 3.4 the stress of the heated bar can be described:

$$\sigma_1 = -\alpha \Delta T \frac{2E(T_0)}{1 + (2E(T_0)/E(T))} \tag{3.5}$$

The three bar model and the stress equation only describe stress development in the elastic region. However, as temperature increases, the yield point decreases which will cause large amounts of plastic zones. The plastic zone will lead to an additional effect on the residual stress state of the material.

3.2.4. Heat Affected Zone

The base material close to the weld will be affected by the local concentrated heat input. This region is called the Heat Affected Zone (HAZ). The HAZ experiences a large variance of temperature in a relative short time, which cause local micro-structural changes. Therefore, the HAZ has different material properties (see Section 3.1.1). This issue effects the performance of the welded connection, accordingly care should be taken for material uncertainties at the HAZ. The difference in micro-structure can also provide information of temperature history, as specific micro-structures can be assigned to the temperatures reached of the material.

The HAZ is the zone between weld and base material. From the weld to the base material different zones can be identified (see Figure 3.9). The weld material and the fusion zone are the only areas where steel in liquid state had been present. The composition of the weld metal region is highly dependent on the used welding consumables. The fusion zone is where liquid weld metal and liquid base metal mix and form a bond, which remains bonded after cooling. Further from the weld, after the fusion zone the HAZ starts. The HAZ can be subdivided in the following zones [8, 46];

- Coarse Grained Heat Affected Zone (CGHAZ): The zone closest to the heat sources and thus experiences the highest temperature peak. The high peak temperature has been just below the melting point, this allows for relative large grain growth.
- Fine Grained Heat Affected Zone (FGHAZ): This zone has reached temperatures just above the austenitizing temperature (Ac_3). Limited amount of grain growth is present.
- InterCritical Heat Affected Zone (ICHAZ): Peak temperature value reach between the austenitizing (Ac_3) and eutectoid (Ac_1) temperatures. Micro-structure is very similar to base material.
- SubCritical Heat Affected Zone (SCHAZ): This is where the material has reached a temperature below the eutectoid (Ac_1) temperature. Effects of this zone are very similar to effects of the ICHAZ, difference between SCHAZ and ICHAZ are hard to identify. Properties are the same as the ICHAZ.

Any material further from the weld and past the fusion zone will not have reached the liquid phase and will only have experience changes of micro-structure in the solid phase.

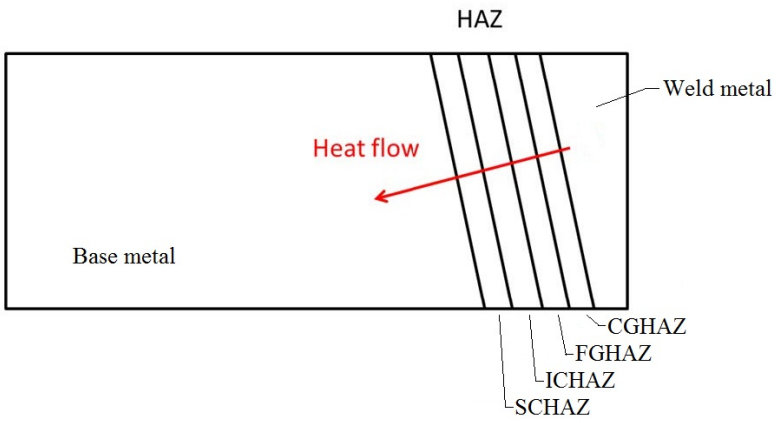

Figure 3.9: Schematic visualisation of the different zones from weld to HAZ and base material. Adopted from Gao [8].

4

Experiment

4.1. Material

Steel of grade S700MC is used the experiments in this thesis. A steel of grade S700MC must have a yield strength of at least 700 N/mm^2 and a maximum tensile strength between 750 and 950 N/mm^2 [47]. This thermo-mechanically rolled high strength steel is produced in different forms of plates and profiles. It can be found in the automotive industry, large mobile machinery (excavators, mobile cranes, trains, etc.), civil engineering (bridges) and can be used for application in extreme cold weather conditions [48, 49]. The steel is well suited for low temperatures since it can retain toughness behaviour at low temperatures. Micro-alloying is typically applied with Titanium (Ti), Niobium (Nb) and Vanadium (V) to ensure good toughness behaviour, proper grain refinement and good hardening properties [50]. In addition, the micro-alloying and the low carbon content of the steel decreases the softening behaviour due to a thermal cycle of a welding process.

However, thermal cycles during welding still cause softening of the Heat Affected Zone (HAZ) which reduces the strength of the material. Therefore, energy input during welding should be limited, reducing the peak temperatures. Pre-heating or post-weld heat treatment is not recommended for this steel grade, to avoid reduction of mechanical and plastic properties of the HAZ. [51, 52]

4.2. Material Properties

The chemical composition of the steel (see Table 4.1) is taken from the material certificate [8]. Corresponding material properties (see Figure 4.1) are determined by Gao [8] by use of the JMatPro software. JMatPro can provide thermally dependant material properties based on the chemical composition of the material, which are calculated by use of extensive material property databases and relations between properties [53]. The same material is used and the work of Gao has shown that selected material values give satisfying results when simulated. Therefore, these material properties are assumed to describe the correct material behaviour in the models of this thesis. No plastic strain information was available for the material, therefore the plastic behaviour is assumed to experience no strain hardening.

Table 4.1: The chemical composition of S700MC according to manufacturing specification [8]

	C	Si	Mn	P	S	Al	B	Cr
wt %-Average	0.049	0.109	1.934	0.009	0.001	0.041	0.0001	0.017
	Cu	Mo	N	Nb	Ni	Ti	V	Sn
wt %-Average	0.011	0.004	0.0049	0.068	0.019	0.121	0.007	0.001

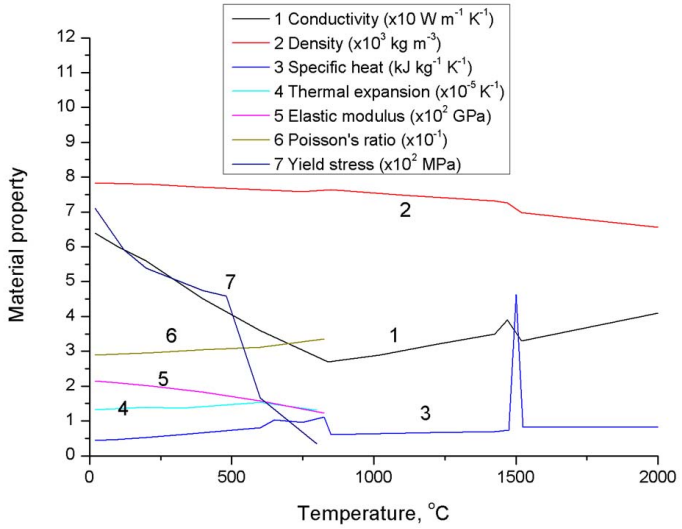

Figure 4.1: Thermal and mechanical properties as a function of temperature, JMatPro results as acquired by Gao [8]

4.3. Welding Specification

Two steel plates of $250 \times 100 \times 4$ mm^3 in size, were welded together by a GMAW process. The weld is executed along the long side of the plate. The joint was made in a V-shaped butt weld connection (see Figure 4.2). At the root of the weld, ceramic backing was placed for insulation, provide support for the molten weld metal and prevent adhesion of the weld metal to other surfaces [54].

Böhler UNION NiMoCr is used as the filler wire. This solid core welding wire has a diameter of 1.2 mm and is classified as a ER100S-G wire [55]. The GMAW welding process was powered by a Fronius TransPuls Synergic 3200 CMT R welding power source. The Short-Circuit metal transfer method was used to perform the welding. The shielding gas was a combination of 85% Ar and 15% CO_2, at a shielding gas flow rate of 15 L/min.

The welding torch was set at an angle of 10° of the normal to the weld specimen, or 100° relative to the welding direction. Contact tube to weld distance (CTWD) was taken to be 15 mm, and the shielding cup edge to weld distance was equal to 7.5 mm, on average (see Figure 4.3). The welding wire feed speed is set equal to 5.7 m/min, and the welding speed is set to 5.0 mm/sec. An overview of these welding parameters is given in Table 4.2. The power source was set to a fixed wire feed speed. Voltage and current were determined automatically by the power source during the welding process.

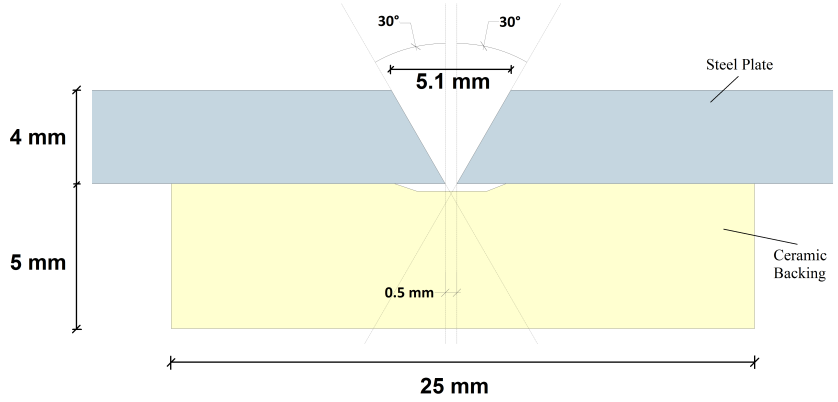

Figure 4.2: The V-shape geometry of the butt joint.

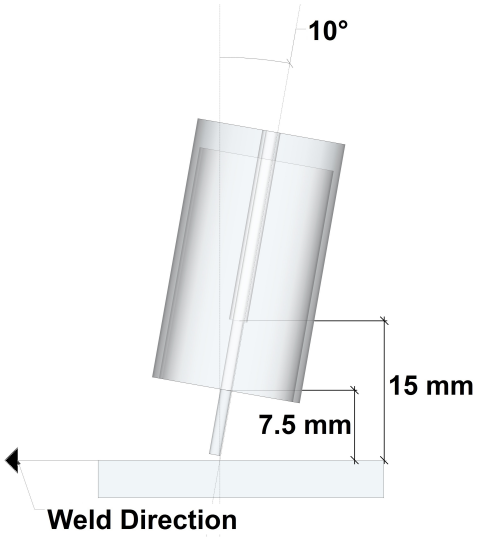

Figure 4.3: Schematisation of the welding torch setup.

Table 4.2: Overview of the welding specification of the first welding test

Steel Grade	S700MC	
Workpiece Dimension	250 × 100 × 4	mm^3
Welding Process	GMAW	
Weld Transfer Mode	Short-Circuit	
Weld Type	Butt Weld	
Weld Shape	V-shape	
Contact Tube to Workpiece Distance	15	mm
Weld Gun Angle	10	°
Shielding Cup to Workpiece Distance	7.5	mm
Wire	Böhler UNION NiMoCr	
Wire Classification	ER100S-G	
Wire Diameter	1.2	mm
Wire Feed Speed	5.7	m/min
Shielding Gas	85% Ar - 15% CO2	
Shielding Gas Flow Rate	15	L/min

4.3.1. Constrainment

The used constrainment on the weld experiment allowed for partial free movement of the plate (see Figures 4.4 and 4.5). Consequently, welding distortion is able to form in a magnitude of millimetres. In such manner, distortions measurement can be performed with relative basic equipment, such as a calliper. The bolts which clamp the specimen together have been fastened firmly, but 'hand-tight' in a cross pattern sequence. The clamping set-up was designed such that un-clamping during different stages of the experimental work was prevented. This consists of the welding of the plate, the removal of material and the repair weld. Unclamping of the specimen can induce significant deformation changes (see Section 3.2.2). By use of this clamping setup, the modelling of the effects of clamping and un-clamping can be avoided in the FEM simulation. To maintain the distance between the plates of 0.5 mm, two tack welds have been placed on each end of the to be welded edge. Both tack welds had a size of 7 mm in the longitudinal direction of the weld. On the clamping bracket, room has been made to accommodate the ceramic backing (see Figure 4.4).

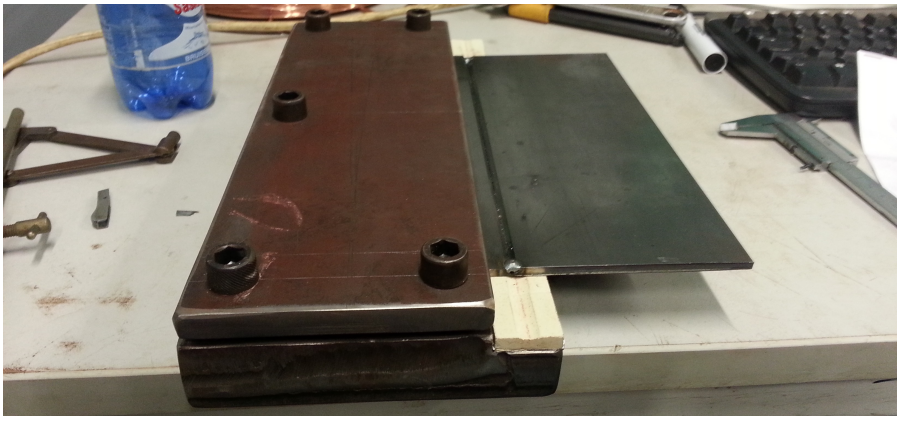

Figure 4.4: Picture of the realised clamping system.

4.3.2. Measurement Setup

During the welding thermal, power and deformation measurement were performed. Six thermocouples were placed to measure the temperature distribution on the plate. K-type thermocouples were used, which can withstand a temperature of 1300 °C maximum with an accuracy of ±1 °C [8]. They were placed perpendicular to the welding direction at the bottom side of the free plate (see Figure 4.5). Deformation during welding is measured by a LVDT, which was placed 7.4 mm from the outer edge (see Figure 4.5). The LVDT measures displacement at 0.39375 V/mm. Voltage during welding is measured between welding table and the contact tube. Current is measured with use of a current clamp [56]. The current clamp measures the magnetic field caused by the current passing through the welding contact cable. The clamp returns a voltage which can be measured, with a measurement value of 1 mV/A.

Two Yokogawa oscilloscopes record the measurement data. A Yokogawa DL716 records the LVDT and thermocouple values at a recording rate of 2 Hz. LVDT will be recorded in volts, the thermocouples are measured directly in degrees Celsius, through temperature modules in the oscilloscope. A Yokogawa DL750 records the voltage and current at a rate of 200 Hz. Both measurements were recorded in volts.

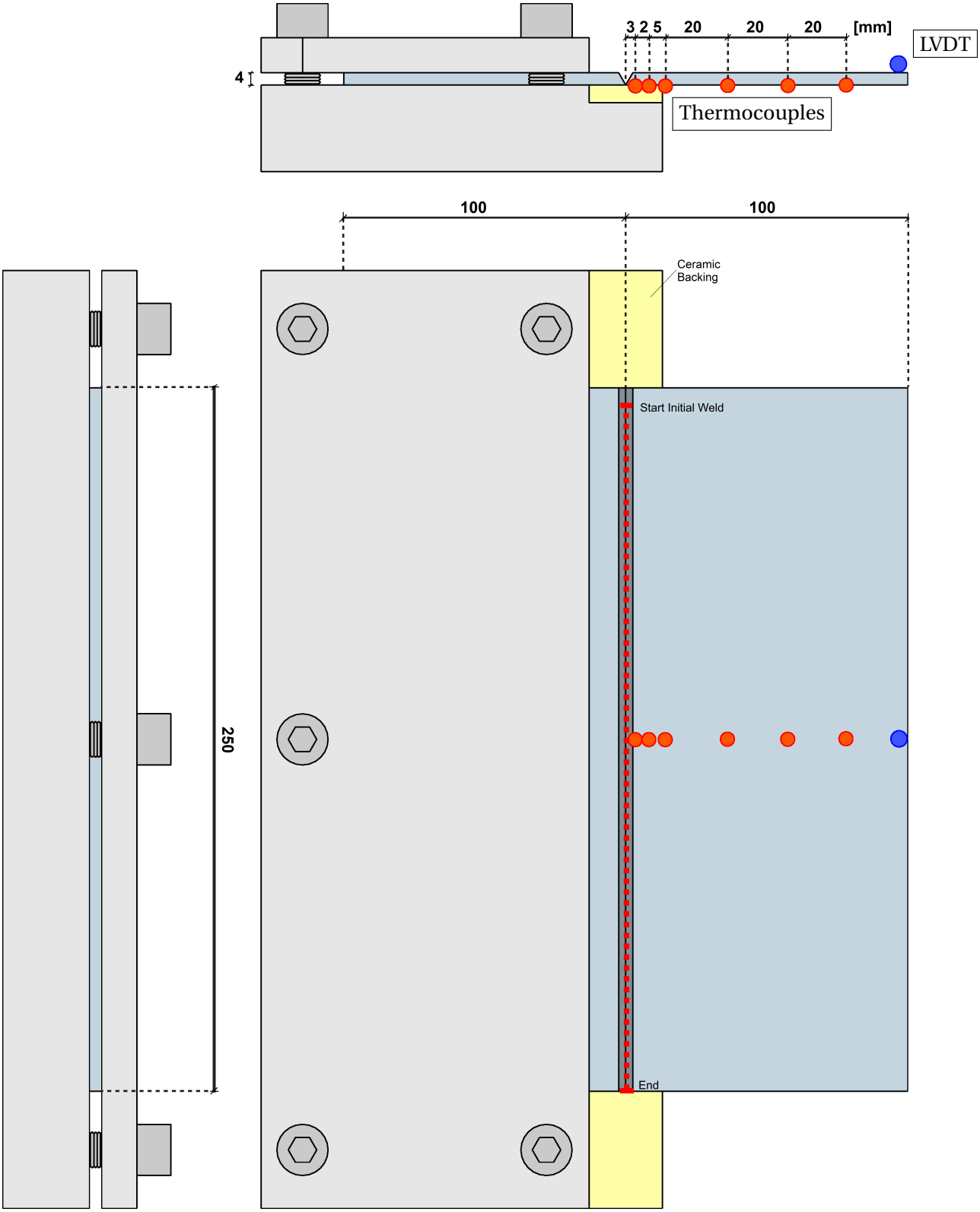

Figure 4.5: Sketch of the clamping system. The red dots indicate the thermal couples locations, the blue the LVDT location.

4.4. Experiment Results

During the experiment, a faulty wire feeding mechanism caused problems to initiate an appropriate arc for welding. The welding procedure was prematurely stopped to investigate this issue. As a result, liquid metal was deposited at the first 44 mm of the weld. LVDT measurement showed no distortion of the plates, but temperature measurement showed a slight increase on the plate. The weld was continues after the problem had been fixed.

Since no welding distortion was measured and no appropriate arc was formed, it is assumed to have no effect on the stress state on the plate. The assumption is made that the effect of the deposited weld metal of the faulty section forms a (new) constrainment of the plate. This constraining effect and the temperature increase of the plate are later taken into account during simulation.

4.4.1. Welding Power Measurement Results

As stated in Section 4.3, welding power input has been automatically determined by the power source. After the welding process, the machine feeds back the voltage and current used during the welding process. In this experiment a voltage of 22.1 volts and a current of 170 ampere was put on display by the power source.

Experimental measurement of voltage and current show large fluctuations during measurement, which is typical for a Short Circuit Transfer Welding (see Section 3.2.1). Measurement have been taken at a rate of 200 Hz on a total duration of 50 seconds. However, due to an unknown error, data measurements were exported at 40 Hz.

The difference of the power input displayed by the power source and the measured power parameters are investigated. Large fluctuations of the experimental measurement make it difficult to determine an average of voltage or current from the measurements (See Figures 4.6 and 4.7). Therefore, the total energy input is compared instead of average power. A comparison has been made at successive time intervals of 5 seconds, see Table 4.3. An overall energy input of approximately +10% was found for the experimental measurement data, compared to the power source data.

Table 4.3: Overview of welding energy input of 6 successive, 5 second intervals.

Interval [sec]	Total Energy - Measurement [Joule]	Total Energy - Power Source [Joule]	Difference [%]
2.5 - 7.5	20299	18785	~ +8
7.5 - 12.5	21413	18785	~ +14
12.5 - 17.5	20390	18785	~ +8.5
17.5 - 22.5	21208	18785	~ +13
22.5 - 27.5	21058	18785	~ +12
27.5 - 32.5	20181	18785	~ +7.5
		Average	~ +10.5

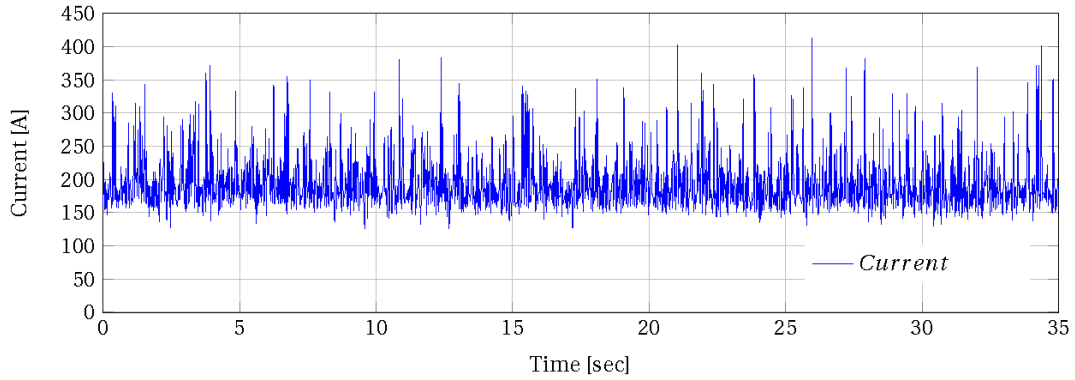

Figure 4.6: Current measurements during the welding process. The results shown are measurement points of 40 Hz instead of the real-time measurement rate of 200 Hz.

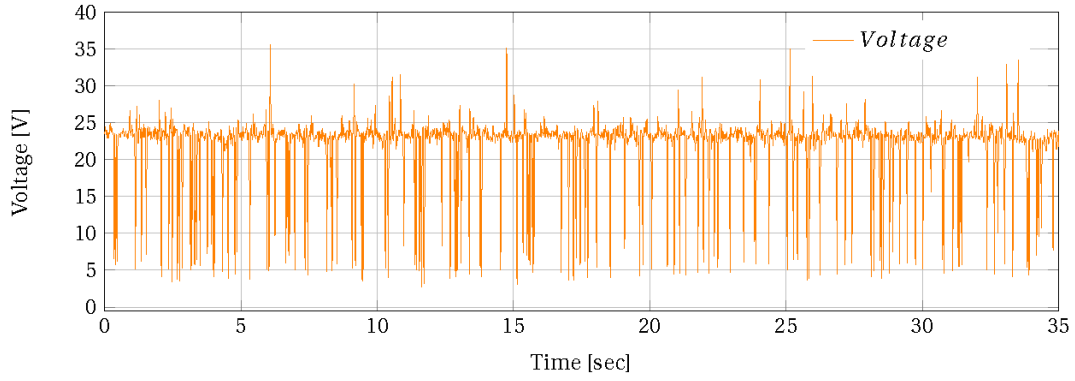

Figure 4.7: Voltage measurements during the welding process. The results shown are measurement points of 40 Hz instead of the real-time measurement rate of 200 Hz.

4.4.2. Transient Heat Measurement Results

The thermal couple measurements are given in Figure 4.8 and Figure 4.9, for the first 400 seconds and between 940 and 1450 seconds after welding, respectively. During cooling, around 500 °C a clear temporary decrease of cooling can be observed. This has most likely occurred due to latent heat which is formed during some kind of phase transformation.

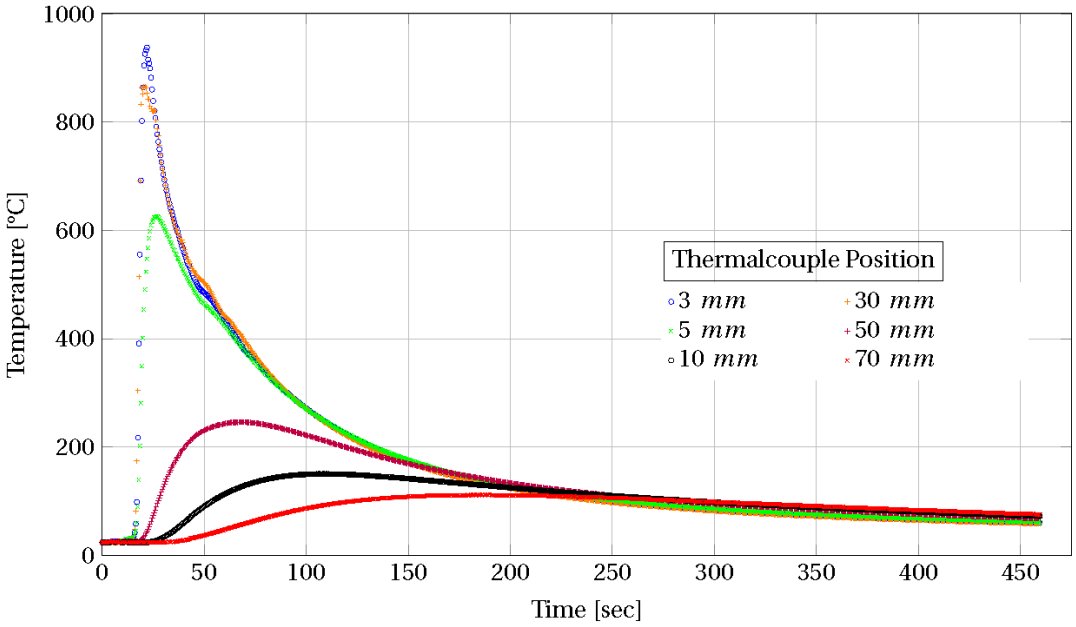

Figure 4.8: The thermal results of the first welding test, between the period of 0 and 400 seconds after start of welding

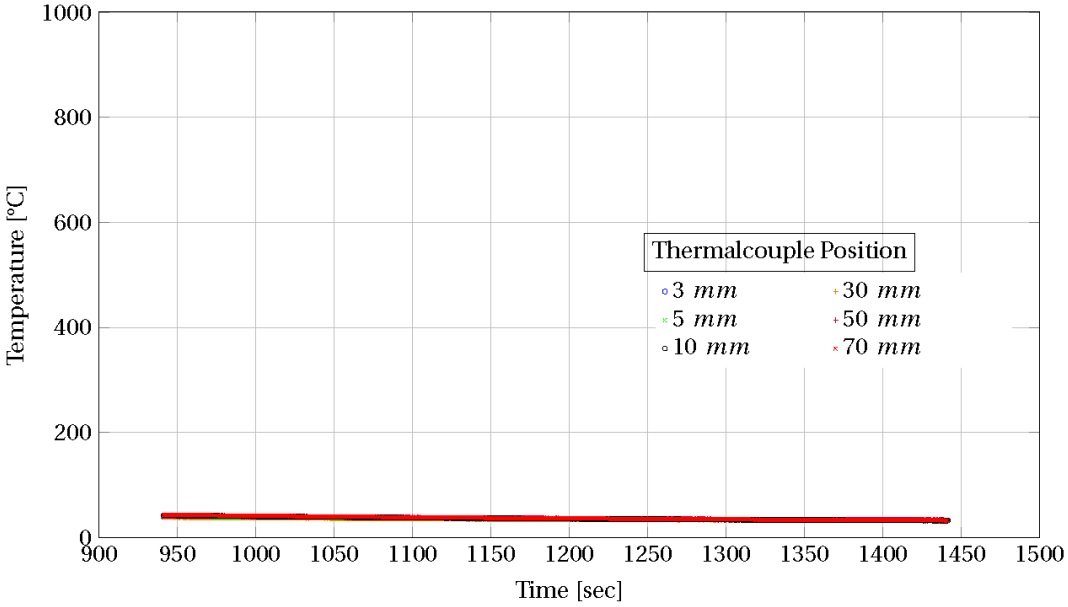

Figure 4.9: The thermal results of the first welding test, between the period of 940 and 1450 seconds after start of welding

4.4.3. Deformation Measurement Results

For reliable information of deformation measurement, three measurement techniques were used; LVDT measurement, contact measurement and image correlation measurement.

Transient Deformation Measurement

Two recordings have been made of distortion LVDT measurement, as similar to the thermal measurement. The first recording at the beginning of the welding procedure, of about 450 seconds (see Figure 4.10). A second recording was made, approximately 1000 seconds after the start of the welding process. No additional distortion was found at this time after welding. Final result show a deformation of approximately 3.74 mm.

The transient LVDT measurement results show continuous noise during measurement, and some sudden peak values can be observed. This may be caused by the LVDT power supply; the wiring of the power supply has been customised in the past to suit two LVDT measurement devices, instead of one.

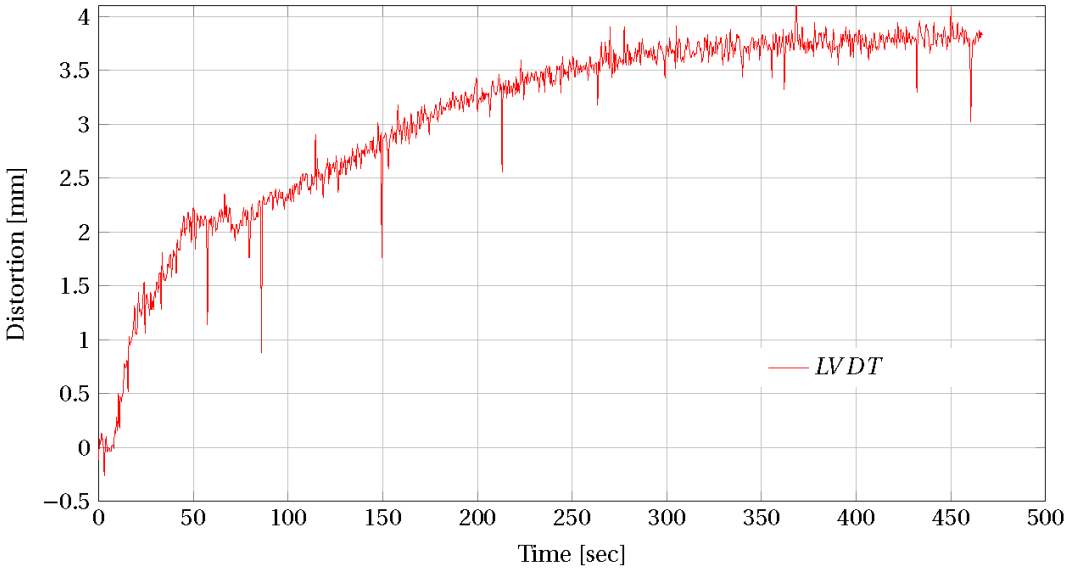

Figure 4.10: The LVDT deformation results of the first welding test, between the period of 0 and 500 seconds after start of welding.

Contact Measurement

Before and after the welding process contact deformation measurements were performed by use of a calliper. The top of the clamping plate has been used as a reference surface for deformation measurement. The clamping plate was assumed to experience no significant distortion after the welding process. This assumption was verified with image correlation measurement. A leveler was placed on the clamping plate to provide a convenient reference point for the measurements (see Figure 4.11). A three by seven size grid has been set up, where measurement are taken, ensuring full coverage of the plate deformation, see Figure 4.12 for the measuring points. The measurement results are given in Table 4.4.

LVDT measurement is compared with the calliper contact measurement results. The deformation

data is interpolated to approximate the deformation at the location of the LVDT. A deformation of 3.99 mm was found, where it was measured as 3.74 mm by LVDT. Taking into account the relative rough measurements of the contact measuring and the precision of the LVDT measurement point; measurements are sufficiently close to say that measurements have been performed accurately.

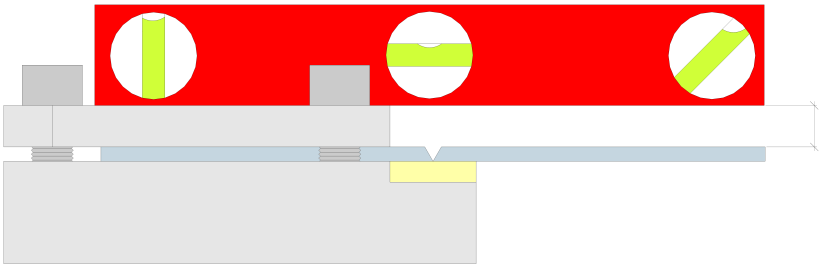

Figure 4.11: Contact measurement setup, side view. The clamping top plate is used as a reference for a leveler. Distance between the leveler and plate is measured with a calliper.

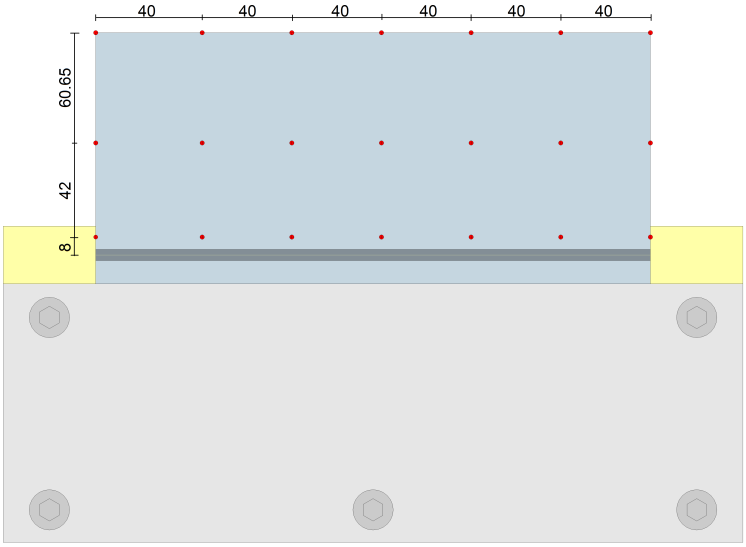

Figure 4.12: All the measurement points for the contact measurement. Horizontal counts 7 points, from 0 to 240 mm in steps of 40 mm. Vertically three measurement points have been measured, starting from 8 mm to 102.65 mm from the weld centre.

Table 4.4: Deformation by contact measurement

[mm]	8	50	102.65
240	+1.40	+0.78	+2.49
200	-0.62	+0.95	+3.07
160	-0.26	+0.37	+3.57
120	-0.24	+0.53	+3.75
80	+0.16	+1.95	+3.88
40	+0.08	+2.12	+3.76
0	+0.15	+1.43	+3.24

Digital Image Correlation Measurement Results

Measurement by Digital Image Correlation (DIC) have been performed to get an accurate field image welding distortion. A Limess 400 DIC system [20] was used for the image correlation measurement. It is mounted on a tripod and pointed towards the floor and it is calibrated before taking measurement. This resulted in a measurement with the maximum standard deviation of 0.908 μm on a measurement point measuring 2.8 mm in deviation. Hence, high accuracy distortion measurement was achieved.

The correlation system needs sufficiently clear reference points to relate the different measurements with each other. A reference surface is created by applying a high contrast painted pattern. First a full covering white base layer is applied, after which a paint speckle pattern is created with an airbrush and diluted black paint. This paint pattern provides correlation reference points which are of high contrast, and thus relatively easy to trace for the system. The paint is not suitable for higher temperatures, thus damage of the paint was expected during the welding process. Measurement of distortion was focussed on the area further from the weld, where the paint was not affected. The speckle pattern applied to the specimen is an evenly distributed pattern, with paint speckles varying from approximately 0.3 to 1.7 mm in size. See Figure 4.13 for a zoom of the speckle pattern.

Two images were made; before and after welding. The reference points on the plates were correlated to find the distortion due to the welding process. After welding, also the paint further from the weld was partially damaged (see Figure 4.14). This was due to the weld spatter during welding. As can be seen in the figure, the image correlation software ignores these areas and correlated the surrounding paint pattern.

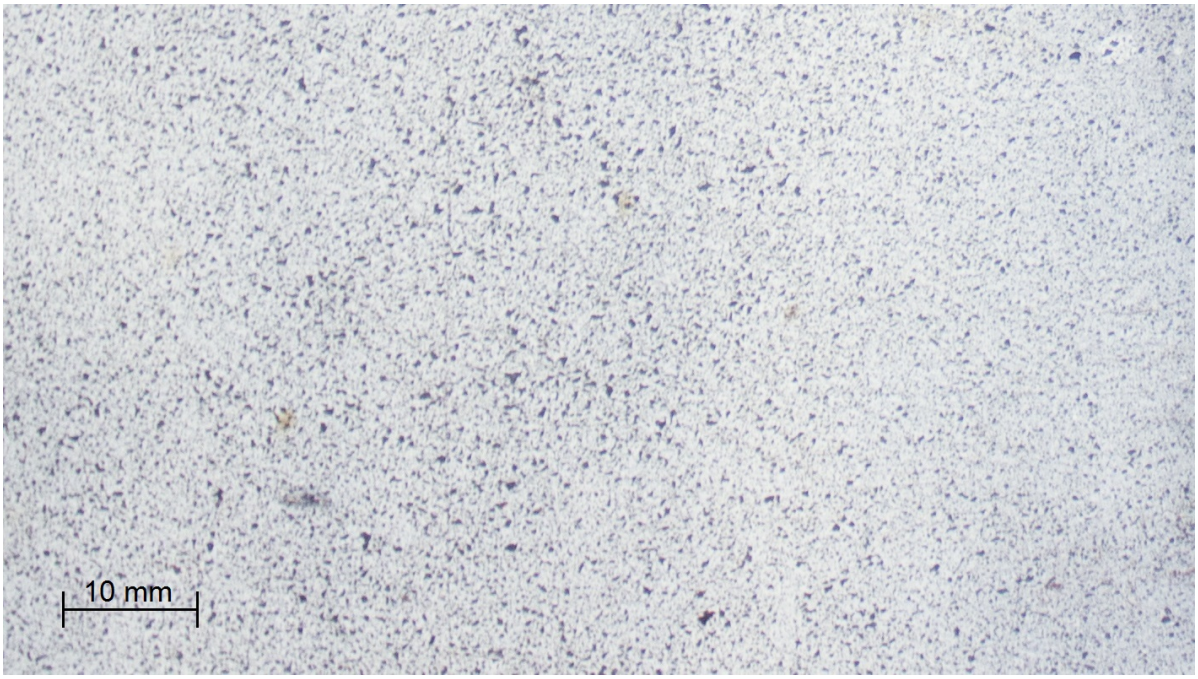

Figure 4.13: A zoom of the speckle pattern applied on the specimen. Speckle size varies from 0.3 to 1.7 mm.

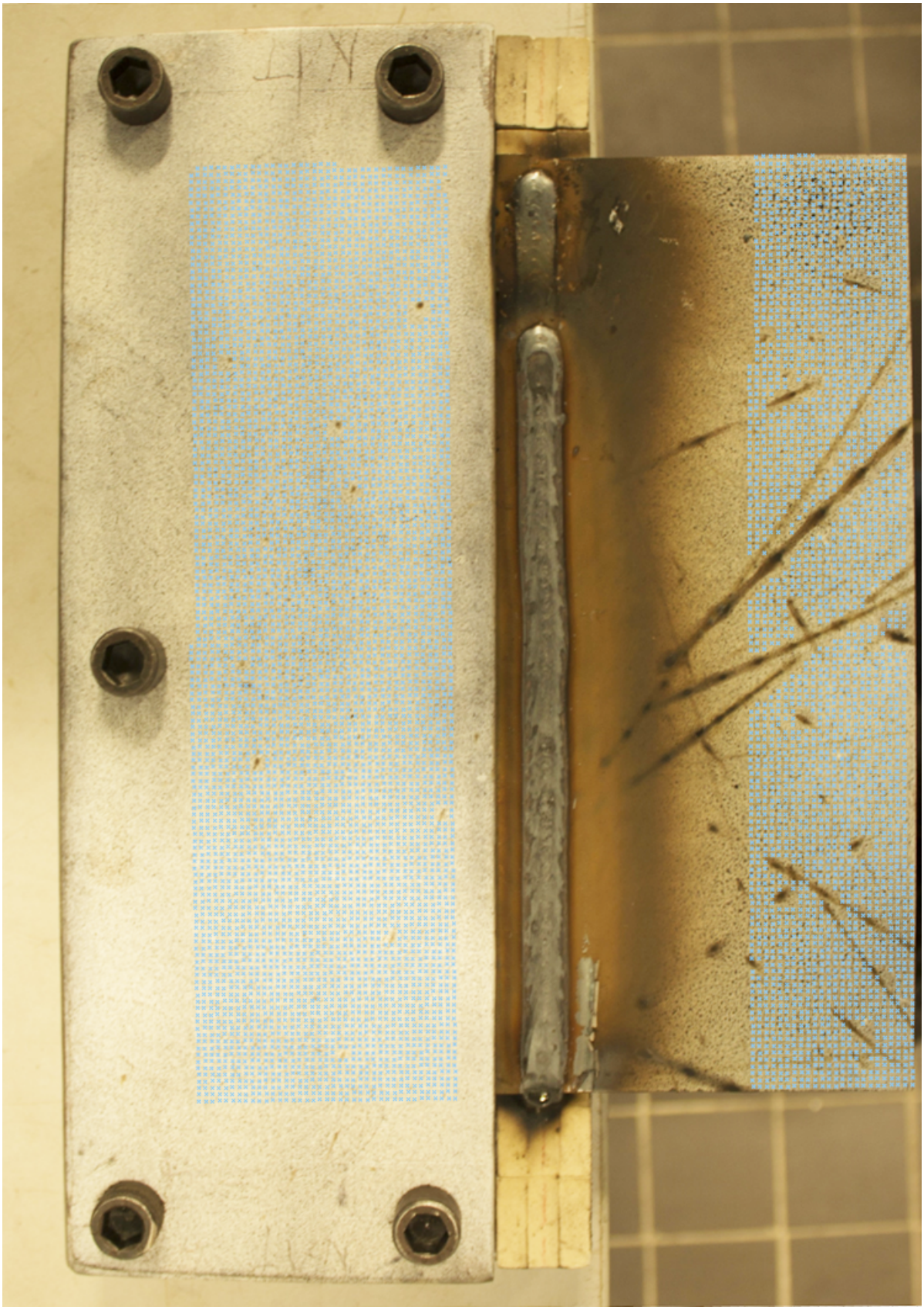

Figure 4.14: The DIC reference measurement point are depicted as blue crosses on the plate. Close to the weld the paint is burned due to the increase in temperature. Further from the weld, traces of weld metal shot off during the welding process can be found, leaving a burned or discoloured trail of paint.

5

Simulation

In Section 3.2 several important aspects of a welding process were discussed. It is possible to model all these aspects of a welding process by the use of an finite element analysis [57]. For example, accurate modelling can be used to simulate the weld pool, including fluid dynamics of the liquid metal and the simulation of different forces acting on the material [58, 59]. Another example for detailed simulation is to model the micro-structural evolution of the material [60–62]. From this micro-structural analysis and the temperature data, the residual stress fields due to the welding process may be derived.

In reality the detailed simulation of all the aspects of a welding process is very difficult to execute. The difficulty is a result of high complexity of the problem, the required computation time, large amount of input data which has to be known, and the ability to perform required measurements for this input data. [57]. In order to simplify the simulation problem, focus in this thesis will be on temperature-dependent properties of the material. Therefore, a thermo-mechanical analysis is performed to model the welding distortion.

A thermo-mechanical analysis is the mechanical analysis of a specimen which is subjected to a certain temperature distribution. The temperature changes material properties, which in turn have a mechanical effect on the model. In the model of this thesis the welding simulation is performed in a decoupled thermal and thermo-mechanical analysis. In the thermal analysis, the temperature distribution is simulated by subjecting the model to a direct heat source. This heat source represent the thermal effects of the weld pool. In the thermo-mechanical analysis, temperature-dependent material properties are used to simulated the material response of a thermal load.

The finite element simulation software Abaqus [63] is used to model the thermal and thermo-mechanical analysis of the welding distortion. Within the Abaqus software, several Fortran based user specified subroutines are utilised to implement the behaviour of the material. The different modelling procedures in the Abaqus software are presented in Figure 5.1.

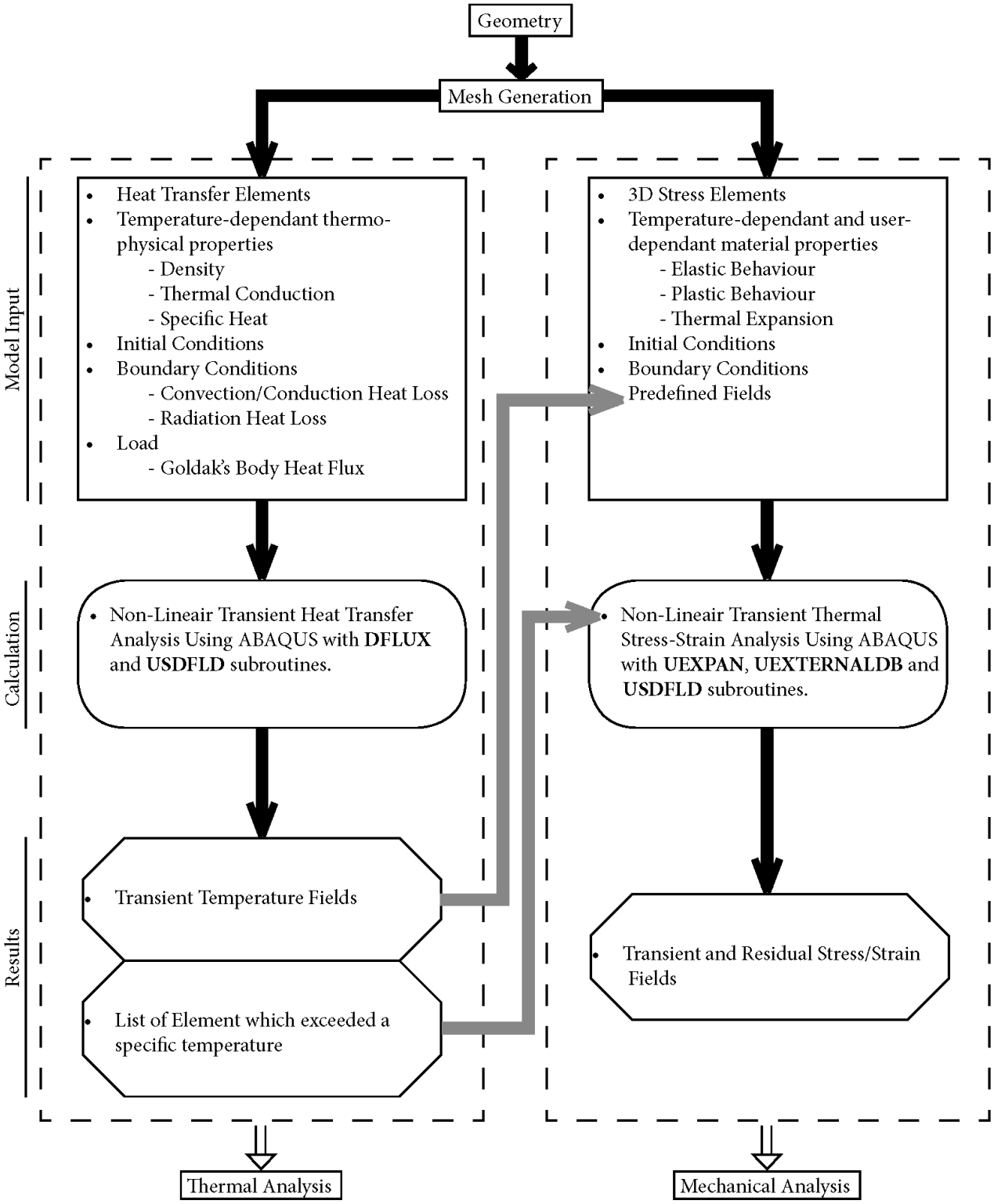

Figure 5.1: Visual representation of the different procedures performed in the Abaqus software environment. Adopted from [57].

Sections 5.1 and 5.2 of this chapter will discuss the different physical welding phenomena which are implemented in the model to ensure a correct simulation of the welding process. After which the implementation in the Abaqus software of these phenomena are explained in Section 5.3.

5.1. Thermal Behaviour Modelling

5.1.1. Energy Transfer Mechanism

During a weld heat cycle, the base material will heat up, experience a peak temperature value, and cool down. Thermal conduction through the material causes heat to be internally distributed over the workpiece. The heat is lost through convection, conduction and radiation, cooling the material down to room temperature.

Under conventional, non-hyperbaric, welding conditions, convection can be defined identical to conduction. The first thin layer of air close to the material exchanges heat by ways of conduction [64]. Consequently, surface heat losses due to conduction and convection can be described as: [8, 65]

$$q_{l,c} = h(T - T_0) \tag{5.1}$$

where $q_{l,c}$ is the surface heat loss flux in W/m^2. h is the heat transfer coefficient in W/m^2K, which can be a combination of the thermal conduction coefficient and convective heat transfer coefficient. This dependence on whether convection and/or conduction is applicable. T is the surface temperature and T_0 the room temperature. Heat losses due to thermal radiation can be described as

$$q_{l,r} = \varepsilon\sigma_B(T^4 - T_0^4) \tag{5.2}$$

where $q_{l,r}$ is the surface radiation heat loss flux in W/m^2, ε is the radiation emissivity, σ_B the Stefan-Boltzmann constant. And finally, for heat conduction within the material, Fourier's isotropic heat conduction is used

$$\boldsymbol{q_c} = -\lambda\nabla T \tag{5.3}$$

where $\boldsymbol{q_c}$ is the heat flux vector and λ the thermal conductivity matrix. During the thermal modelling process the heat conduction and losses are modelled, to simulate the heat flow through and out of the material. To implement the heat flow through the material special heat transfer element have to be used, which contain degree of freedom regarding the energy distribution. For the modelling of the heat losses, thermal boundary conditions are applied where heat losses can occur.

5.1.2. Heat Application Method

In this section the two main possibilities for the simulation of a heat source are described. These are the heat distribution method and the segment method.

Heat Distribution

For numerical simulating purposes, a volumetric heat flux can be used to simulate the thermal distribution in a workpiece [8, 66–68]. A widely used volumetric power density distribution is the Goldak distribution [66]. It describes a double ellipsoidal shaped function to represent a heat density distribution induced by a welding process. The front and back of the distribution are defined

separately as $q_f(x,y,z,t)$ (equation 5.4) and $q_r(x,y,z,t)$ (equation 5.5) respectively.

$$q_f(x,y,z,t) = \frac{6\sqrt{3}Qf_f}{abc_f\pi\sqrt{\pi}} e^{-3\left(\frac{x^2}{a^2}+\frac{y^2}{b^2}+\frac{(z-vt)^2}{c_f^2}\right)} \tag{5.4}$$

$$q_r(x,y,z,t) = \frac{6\sqrt{3}Qf_r}{abc_r\pi\sqrt{\pi}} e^{-3\left(\frac{x^2}{a^2}+\frac{y^2}{b^2}+\frac{(z-vt)^2}{c_r^2}\right)} \tag{5.5}$$

where q_f and q_r are the body heat flux in W/m^3. a, b, c_f and c_r define the size and shape of the distribution in meters, Q is the power input rate in Watts. f_f and f_r describe the distribution of the power input to the front and rear quadrant respectively, where $f_f + f_r = 2$ must hold. v describes the welding speed in m/s, and x, y, z the position coordinates of the distribution (see Figure 5.2). It is important to note that the factors which describe the shape and heat distribution (a, b, c_f, c_r, f_f, f_r) cannot be directly related to a physical welding arc. However, these factors are commonly determined by measurements of the weld pool area [8, 19, 43, 67]. In the simulation adjustment of the shape parameter may be required, to find a good agreement with the measured temperature distribution during a welding process.

$$Q = \eta V I \tag{5.6}$$

The Goldak heat distribution has proven to show results which are in good agreement with experimental results. [8, 19, 43, 67]. However, applying the aforementioned parameters of the distribution does not guaranty a good agreement with experimental measured temperature distribution. Different factors, such a material density and material conduction coefficient material density, are dependent on the temperature and will influence the thermal distribution through the material. Goldak represent the heat input, not the resulting temperature distribution of the material. Therefore, care should be taken to choose the correct parameters, in order to find an appropriate numerical solution.

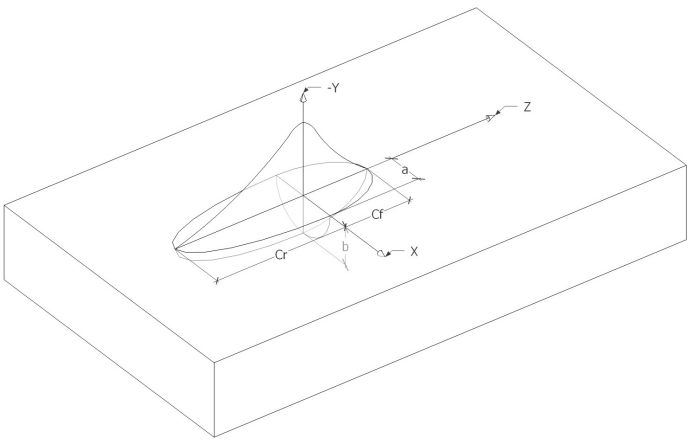

Figure 5.2: Visual representation of the Goldak double ellipsoidal heat distribution function [8, 66]

Segment Method

The segment method combines the thermal and mechanical influence of the molten weld metal by simulating the filling of filler material and temperature at the same time [69–71]. The addition of filler material is simulated by activating elements in separate chunks. These elements have a predescribed temperature, representing the induced heat due to the welding. When compared with the Goldak heat flux method, the segment method resembles more closely the welding process and could give a better representation of the thermal distribution during welding [72]. However, applied parameters need calibration and cannot be derived from experimental measurement, this makes the method highly dependent on the used parameters.

The main parameters to be chosen are the chunk boundary temperature and internal temperature [73]. The chuck is held at an uniform temperature for a certain amount of time (soaking period) to distributed the heat to the adjacent material (see Figure 5.3). The parameters for temperature magnitude and soaking period have to be determined. A trial-and-error based approach has to be implemented to find these parameters, an approximate cannot be determined based on experimentally obtained data. This makes the parameters difficult to determine [69]. The method has proven to find sufficient results for stress analysis [70, 71], but the usage in field of the segment method is low, compared to the relative popular Goldak heat transfer method.

A plug-in is available for Abaqus named the Abaqus Welding Interface (AWI). The plug-in provides an user interface to implement the segment method within the Abaqus environment.[70]

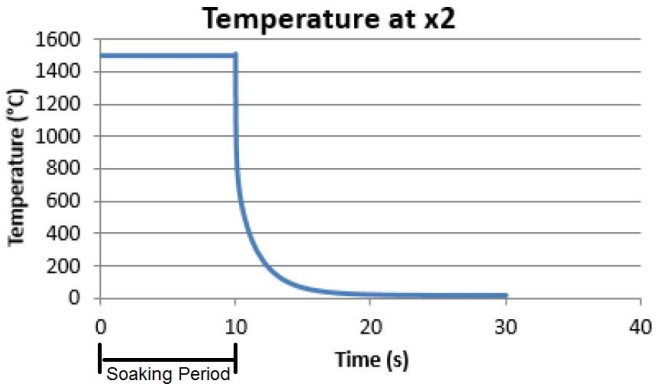

Figure 5.3: Transient temperature behaviour of element which represent the molten welding metal, when using the segment simulation method. [69]

5.2. Mechanical Behaviour Modelling

5.2.1. Element Activation

The constrainment of a specimen is continuously changing during a welding process. As the weld progresses, the material is connected in a gradual manner. This progressive connection prohibits the movement of the specimen more and more, therefore introducing continuously a new constraining condition. This effect is especially apparent when relative large amount of welding distortion can occur, for example with specimens of a thin plate material and limited constraining clamping conditions [12, 74].

Material activation is required to simulate the addition of the weld material, and consequently simulating the changing constrainment condition. The modelling of this process is generally performed by either of the following two approaches: the quiet element activation method or the element birth-and-death method [72].

The quiet element activation method involves lowering stiffness properties during 'in-active' state of the element, limiting its effect on the surrounding 'active' elements. Once the element is regarded 'active', material properties are restored to values corresponding with the current temperature of the material. The method is relatively easily implemented in most FEM software [75]. In the software, material properties can often be made dependent on user specified parameters. Furthermore, the continuous presence of 'in-active' nodes makes a nodal coordinate mismatch (see Figure 5.4) at the moment of element activation is impossible.

By lowering the stiffness, higher strains can be reached with relative low stresses. However, a too low element stiffness may result in an ill-conditioned calculation matrix [72]. Moreover, sudden changes in material properties may also results in numerical solutions problem. Therefore an implementation is required which activates the elements in a smooth manner.

The element birth-and-death technique involves the full de-activation and activation of FEM elements. De-activated elements are excluded out of the model and out of the system of equation of the numerical calculations. Once the elements are regarded 'active' they will be included in the model and the system of equations once again. This method requires the FEM software to allow for the re-computation of the calculation matrices. The birth-and-death method is computational more efficient since it only includes the active nodes in the model. The full model is only considered at the end of the computation, when all elements have been activated.

Nodal position may change during the analysis, due to distortions caused by the welding process (see Figure 5.4). When de-activating elements at the beginning of the analysis, the original or last known position of the nodes is saved. When activating the de-activated elements, the nodal position is loaded again. Due to distortion during the welding process, original node locations may be significantly been changed, which may lead to a nodal mismatch. For smaller distortions, this is not a problem, but large distortions may lead to numerical calculation problems [63].

In this thesis the quiet element activation method is applied. The possibility of altering material properties by an user subroutine, makes this method well suited for the Abaqus software. Moreover, the lack of control of element removal and addition in the Abaqus software makes the quiet element activation are more practical approach.

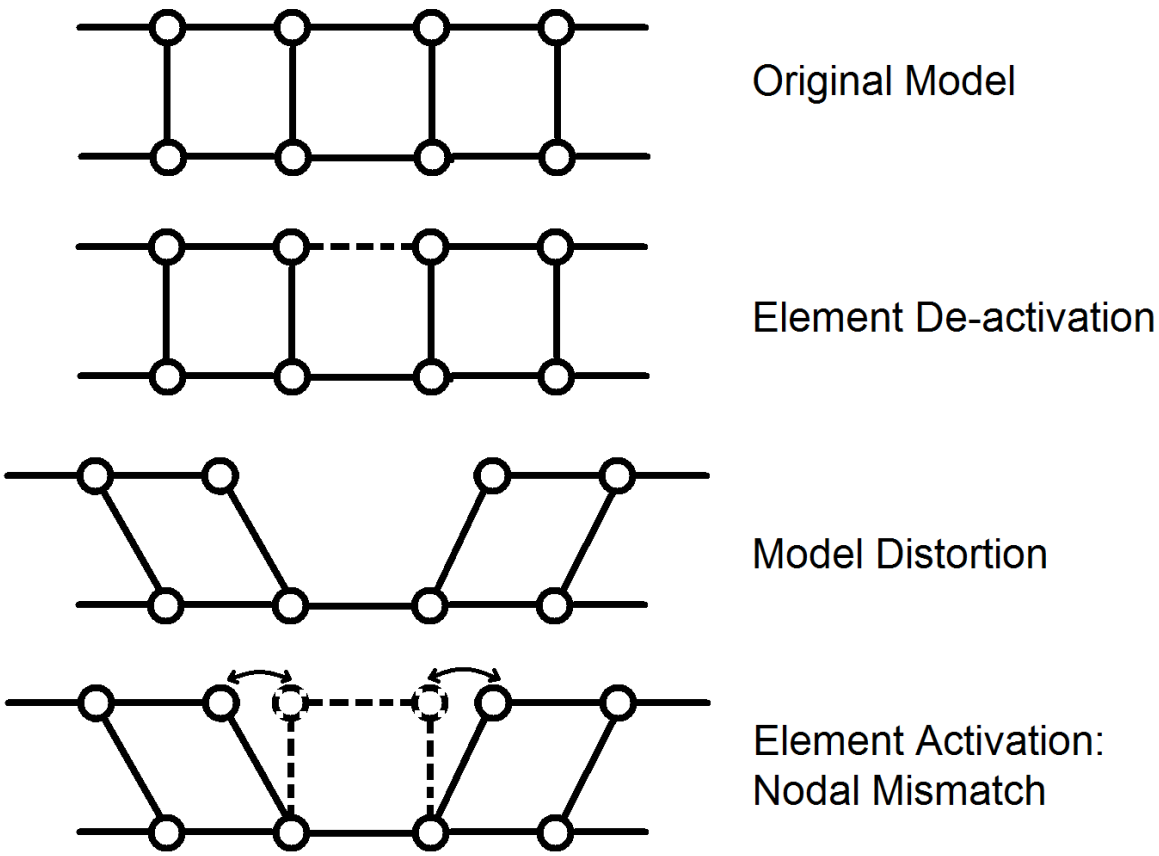

Figure 5.4: Nodal mismatch during birth-and-death technique element activation

5.2.2. Solid-Solid Phase Transformation

Some form of phase transformation will generally be present, when high temperatures are reached during heating and cooling of steel [30]. This phase change transforms the crystalline structure and can induces significant residual stresses by occurrence of a local volumetric expansion. The effects of the solid phase transformation on the volumetric change can be derived from material properties and be incorporated in FEA models.

The volumetric change due to the phase transformation during heating is a results of the transition of a (predominantly) ferrite structure to an austenitic structure. The change of a body-centered cubic (bcc) to face-centered cubic (fcc) structure increases the material density, and therefore lowering its volume. This may induce plastic strains, due to the lowered yield conditions of the steel at higher temperatures. On the other hand, during (rapid) cooling, the austenitic structure may transform back to a martensitic, ferrite, beanite and/or pearlite structure, which induces a decrease of density, increasing the material volume again. This martensitic change occurs at lower temperatures. Consequently, relative high residual stress changes occur, as a results of the relative high stiffness of the material at these low temperatures. [30, 76, 77]

To implement the effects of these phase transition the volumetric changes have to be known. This can be obtained by an explicit and implicit method [8]. The explicit method uses the fraction of different crystalline structures within the metal, obtained by using a continuous cooling transformation (CTT) diagram, to calculate the volumetric changes of the material. These fraction may be a combination of ferritic, beanitic, pearlitic, martensitic and austenitic structures. The diffusion-controlled phase transformations (austenite to ferrite or austenite to perlite and beanite) can be described by the LeBlond equation [8, 78]. Using a constant temperature change rate, this phase fraction can be described with the equation: [8]

$$P_i(T,t) = P_i^{EQ}(T)[1 - exp(\frac{-t}{\tau})] \tag{5.7}$$

where τ represents the phase growth parameter. When the temperature is above Ac_3 the steel fraction is considered fully austenitic. To describe the phase fraction during non-diffusive phase transformations (austenite to martensite) the Koistinen-Marburger equation can be used: [79]

$$P_M(T,t) = P_i^{EQ}(1 - exp(-b(M_s - T))) \tag{5.8}$$

where b is the martensite growth parameter, and M_s the start temperature of the Martensitic transformation. Based on these fractions and using the specific volume of each separate structure the volumetric changes can be described during the phase transformations.

The other method of describing volumetric changes is the implicit method. This method is based on experimental data from dilation tests of steel specimens. The expansion of the steel specimens is tested at different temperatures. In the expansion curves of the steel, thermal expansion behaves linearly (see Figure 5.5). A phase transformation causes a volumetric shift, which is clearly visible in the figure.

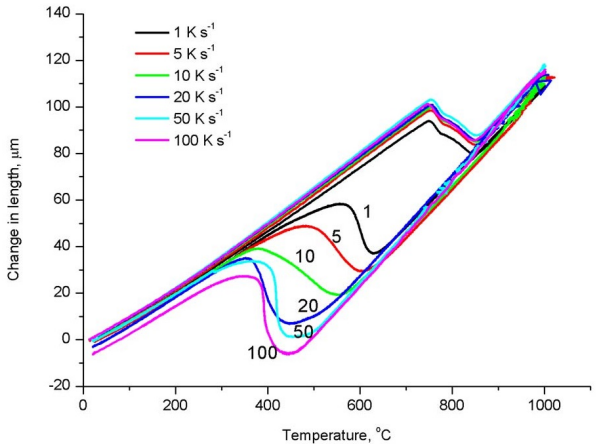

Figure 5.5: Dilatometer result of a S690QL1 quenched and tempered steel specimens. Tests have been performed at different cooling rates. [8]

5.2.3. Solid-Liquid Phase Transformation

Base material near the welding arc will liquefy and become part of the weld pool. During heating of this base material, plastic strain can rapidly build up. This is because of thermal expansion, local constrainment and relative high temperature of the material. The liquefaction, or Solid to Liquid transformation, a virgin state of the material is reset; resetting all previously accumulated strains, transforming to a strain-free (liquid) state. The strain removal has to be considered in FEA model to prevent incorrect build-up of plastic strains, which will lead to incorrect welding distortions. The plastic strains build up during the heating of the material are of compressive nature (see Figure 5.8). This will lead, if incorrectly included in the model, to smaller distortion predictions of the model. [57]

After solidification of the liquid material, strains are able to build up again, starting from a strain free state. To demonstrate the effects of strain reset of the material during heating, liquid state and cooling, a simple FEA bar model was created. This 1D bar model, as depicted in Figure 5.6, is fully fixed at its ends, to allow for a stress during heating of the material. For demonstrative purposes a simple linear heating and cooling cycle is applied to the model. A cycle of 30 seconds is used, beginning at a temperature of 0 °C and reaching a maximum temperature of 1800 °C at 15 seconds, after returning again to a temperature of 0 °C (see Figure 5.7). For this model an arbitrary temperature of 1500 °C is used to depict the temperature above which the material will be in liquid state and should experience a strain reset. Material properties are equal to the material properties used for the simulations in this thesis, which can be found in Section 4.2.

The results of the thermo-mechanical process are shown in Figure 5.8. A clear difference can be seen in the final amount of plastic strain, both in magnitude and direction of the strain. The bar without strain reset ends up with a plastic strain of compressive nature, where as the bar with reset ends up with a plastic strain of tensile nature.

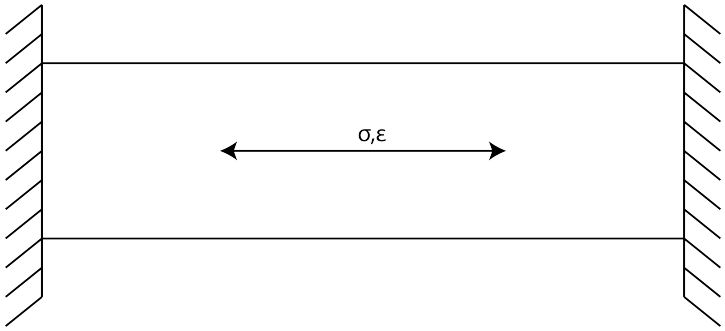

Figure 5.6: A model of a bar fully constrained on both ends. Strains will only act in the axial direction.

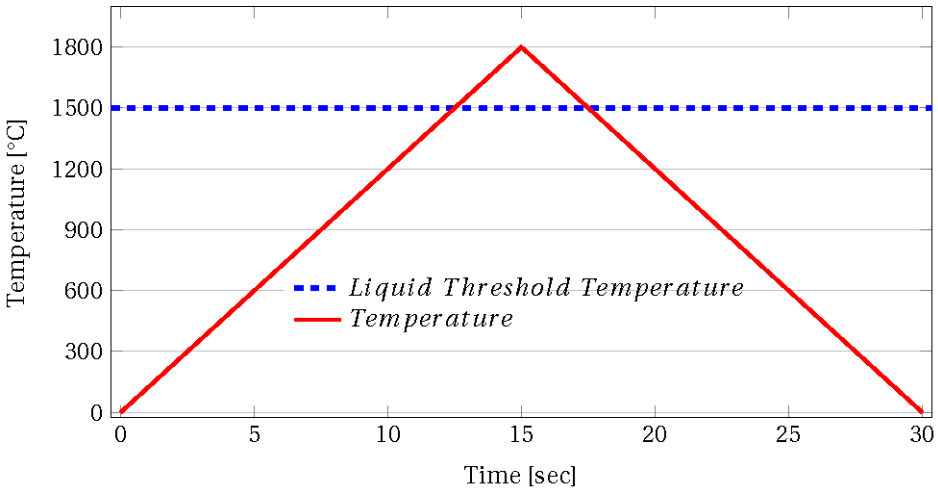

Figure 5.7: The applied thermal cycle for the bar model. A maximum temperature of 1800 °C is reached, while a temperature of 1500 °C depicts the temperature at which the metal is in liquid state.

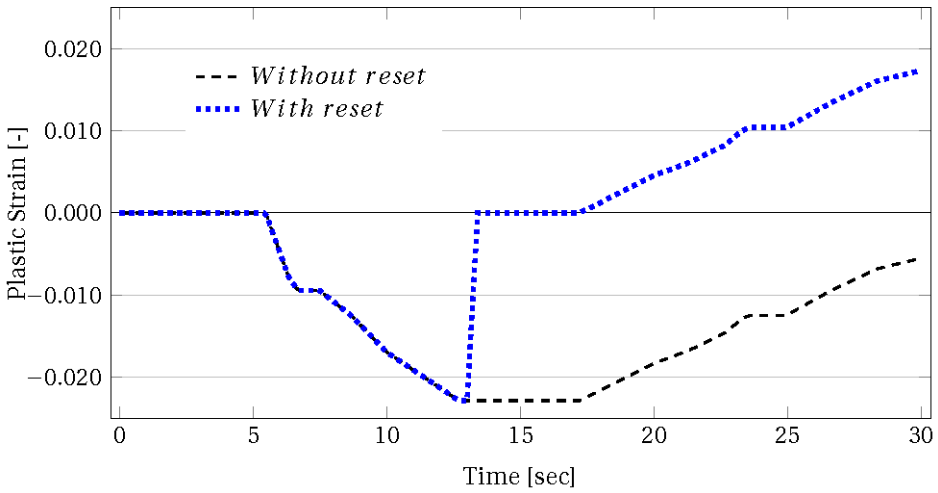

Figure 5.8: The plastic strain build up during the thermal cycle depicted in Figure 5.7 of a bar with and without strain reset.

5.3. Implementation

5.3.1. Element Activation of the Model

To get a correct strain and stress distribution during the simulation, a form of (plastic) strain reset is needed during the heating process (see Section 5.2.3). It was found that a plastic strain reset function was not readily available within the Abaqus software. However, the user is able to develop an User Defined Material Behaviour subroutine (UMAT-subroutine), in which specific material behaviour can be described [63] by controlling the constitutive equations of the elements. A plastic strain reset can be incorporated [57, 80–82] by use of this subroutine, but *"implementation of a realistic constitutive model requires extensive development and testing"* [83]

Accordingly, it was decided that the solid-to-liquid transformation would not be modelled at all, simulating only the mechanical effect from the solidification state onwards. In such manner, mechanical analysis of the weld pool is only modelled in the cooling phase, simulating from solidification the shrinkage of the weld. By neglecting the thermal expansion in the heating phase, any mechanical effect due to expansion is also neglected. This effect however is assumed to be low in this model, since the welded plates are separated at the weld location (see Figure 4.2). The plates are free to move and expand where limited amounts of compressive stresses are build up.

The (separate) mechanical behaviour of the elements which represent the weld pool is implemented in the following manner. During the thermal analysis a database is created to collect elements which have reached a certain threshold temperature. This threshold temperature can for example be set equal to (approximately) the liquefaction temperature of 1480 °C. The database records the element number and this is written to a text file.

During the mechanical analysis, this text file is read out by a database subroutine (UEXTERNALDB-subroutine [63]) within the Abaqus subroutine environment, to use it for the mechanical analysis. This way, the code can determine which elements should follow a specific mechanical behaviour. Where the main two factors of the activation of the weld pool elements in the mechanical analysis are the stiffness properties and the thermal expansion. See Appendix C.3.3 for an example of the subroutine used in this thesis.

The following sections will discuss the implementation in the model of the physical phenomena discussed in Section 5.1 and 5.2.

5.3.2. Implementation of the Thermal Analysis

An user defined subroutine is required for the implementation of the Goldak heat distribution in an Abaqus model. The DFLUX-subroutine is used to describe a heat density function [63]. Equations 5.4 and 5.5 are implemented in the subroutine code, which is a relative easy procedure. In Appendix C.2.2 the full DFLUX-subroutine code is shown and discussed.

As was described in Section 5.1.2, the Goldak heat distribution needs adjustment of its parameters to find an appropriate numerical solution. By adjusting the parameters, a numerical solution can be found which is in agreement with experimentally found thermal results. In this thesis, shape parameters were fixed and the power efficiency parameter was used to fit the numerical results.

It was found that 2D shell results of the heat analysis were in close agreement with 3D solid element heat analysis. The 2D model was used to determine a good approximate value for the power efficiency parameters. Accordingly, this parameter was used in the 3D model of the heat analysis and, if needed, adjusted to find a good agreement of the thermal results. The 2D shell model was used to get a good estimate of the efficiency parameter in a significantly shorter computational time, compared to the 3D solid elements models (See Table 5.1). Moreover, the use of pc storage is significantly lowered by using the 2D model.

If calibration is focussed on temperature near the weld, not the full 3D model has to be completely finished. This can give an estimate of the Goldak parameters in the 3D model and it will save time. However, for calibration of heat cycles further from the weld more time is needed, since it takes a long time for the temperature cycle to reach its peak value. Simply stated, if 20% of the total computation time is calculated, a reduction of 80% in computation time is achieved during calibration.

Table 5.1: Simulation Performance Overview

	2D	3D	3D - 20%
Number of Degree of Freedom	414	32345	32345
Storage [KiloByte]	25,080	8,078,578	1,615,715
User Time [sec]	760.50	1.35652E+05	27130.4
System Time [sec]	46.800	3167.3	633.46
Total CPU Time [sec]	807.30	1.38819E+05	27,763.8
Wallclock Time [sec]	383	47044	9879.24

It was found that a linear approach to finding the correct welding efficiency parameter leads to acceptable efficiency approximation. The matching of experimental and simulation thermal results by altering the welding efficiency parameter is performed with the following approach (see Figure 5.9):

- Step 1: Choose an initial efficiency parameter (η_0), for example 0.7. Run the analysis.
- Step 2: Analyse the thermal results at a location which corresponds with the location of the thermocouples of the experiment. Record the maximum (peak) temperature reached (T_0). Use the simulation peak temperature with the used heat efficiency parameter and the origin, to linearly inter- or extrapolate for a new heat efficiency parameter, based on the peak temperature of the experiment (T_{exp}). Run a (new) analysis with the new found efficiency parameter (η_1).
- Step 3: Similar to the previous step. But in this case, inter- or extrapolate between the first analysis peak temperature results (T_0) and efficiency parameter (η_0) and the second analysis peak temperature results (T_1) and efficiency parameter (η_1). Again using the experiment peak temperature (T_{exp}). Run the third analysis.
- Step 4: Repeat Step 3 until a sufficient match of peak temperatures between simulation and experiment has been reached.

This matching method is only considering temperature peak results. If curve shapes of the thermal cycle do not match sufficiently after matching of the peak results, it is likely the heat distribution through the material is not simulated well. A change in thermal boundary conditions, thermal material properties or Goldak shape parameters may be needed.

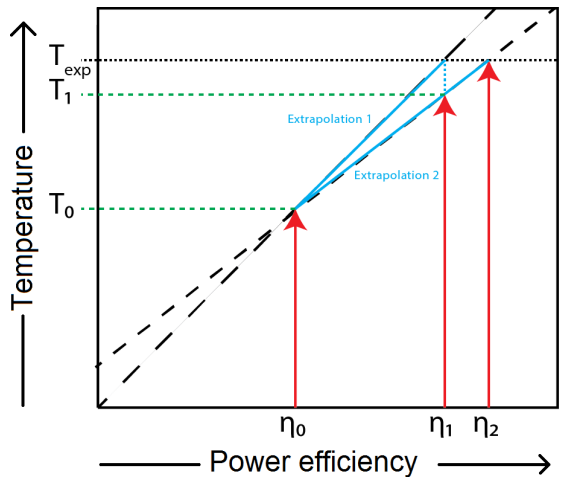

Figure 5.9: Visual representation of the thermal data and weld efficiency fitting approach. This example shows the use of extrapolation only, interpolation can also be used.

5.3.3. Implementation of Thermal Data Database

The evaluation of temperature during a thermal analysis asks for a small work-around, since a temperature data request is unavailable in the heat flux subroutine. To make use of the temperature data an user defined field variable subroutine (USDFLD-subroutine) is added. During the thermal analysis this subroutine is used, but does not specify a specific field variable, therefore not changing material properties during the analysis. Instead, the subroutine is used to request temperature data from the model and analyse whether the element has reached a certain temperature.

To prevent generation of large database files during the analysis of the temperature data, efficiency measures had to be incorporated. A limit is set to the evaluation volume of the weld pool temperature data and elements are marked when the melting temperature has been reached, so these element are further in the analysis excluded in the evaluation routine. See Figure 5.10 for a visual representation of the limited evaluation volume for the element temperature data.

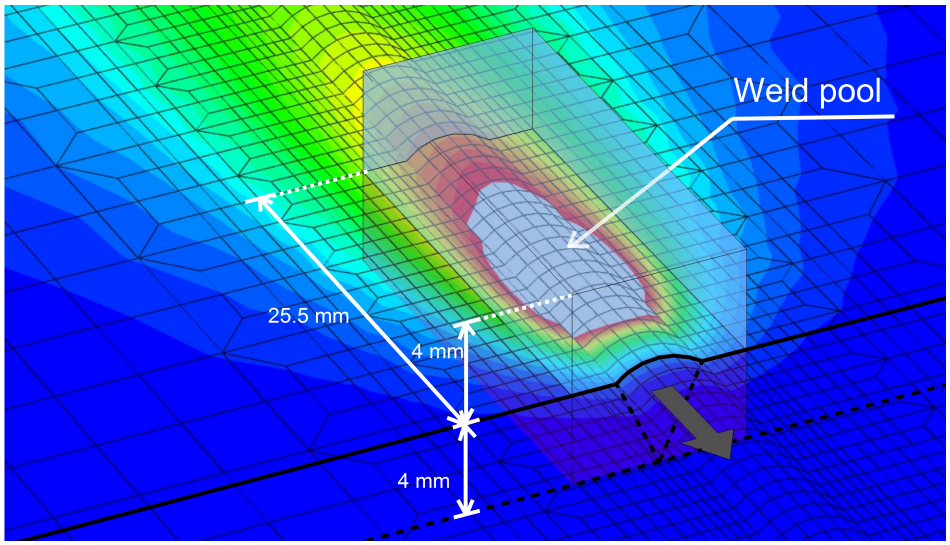

Figure 5.10: For every element within the box, temperature data is recorded. The box translates together with the weld pool, increasing analysis efficiency

5.3.4. Implementation of Element Activation: Material Softening

In this thesis the quiet activation method is used (see Section 5.2.1). Softening of the elements is implement by applying an artificial high temperature on the elements. At high temperatures, the stiffness of the elements is low (see Section 4.2), simulating an in-active element [84]. Elements which present the weld pool will be artificially held at this softening temperature until cooling of the element occurs.

Cooling occurs immediately after the peak temperature of the element has been reached. At this peak, temperature is certain to be higher than the liquidus temperature, since the element activation is only regarded for elements which experience a liquid-to-solid transformation. At this high temperature material stiffness is low, allowing a smooth transition from material properties at softening temperatures to material properties at the current temperature. As soon as the cooling has started, material properties are restored to be dependent on the current temperature of the element (See Figure 5.11).

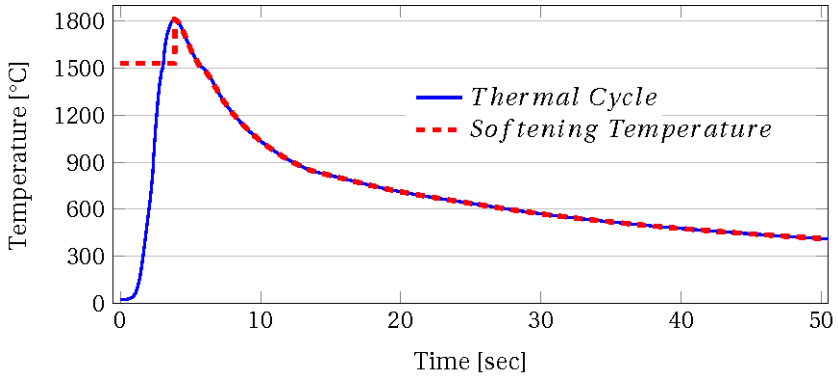

Figure 5.11: A nodal thermal cycle together with the artificial thermal cycle of a weld material element. Artificially high temperature are kept at Softening Temperature to ensure low stiffness during 'in-active' state of the element. In the cooling state under the Softening Temperature, the normal temperature profile will be followed. Note, temperature value of the element due to calculation is not altered. Adopted from [84].

Implementation of a softening temperature in Abaqus requires the use of a USDFLD-subroutine [63]. This subroutine allows the user to control material properties based on the solution of a model, during an analysis. The subroutine for softening of the element can be found in Appendix C.3.1.

5.3.5. Implementation of Element Activation: Thermal Expansion

When element activation is applied in the model, as discussed in Section 5.3.4, the material is activated just after the peak temperature of the element has been reached. In reality, when the solidification of the liquid material happens, it starts off in a zero strain condition, building strains as the material cools down [57]. This zero strain condition has to be implemented in the model to simulate the correct behaviour of element solidification. However, due to relative high temperatures during activation in the model, high thermal strains will be present due to the default thermal expansion definition of Abaqus.

The default equation of thermal expansion used in Abaqus is represented in Equation 5.9. Where θ, θ^0 and θ^I are temperatures at the current time, the reference temperature and the initial temperature, respectively. The thermal coefficient at the initial temperature (α^I) and the current temperature (α). The thermal expansion definition includes a correction regarding the initial temperature and the reference temperature.

$$\varepsilon^{th} = \alpha(\theta - \theta^0) - \alpha^I(\theta^I - \theta^0) \tag{5.9}$$

This forms a problem when element stiffness is restored during re-activation, due to the high temperature, large amount of plastic strains instantly form. This is not representative for a real welding process and furthermore, the sudden increase of stress will lead to numerical instability. Therefore, a different strain definition in the software is required.

An user subroutine is used to implement the required behaviour of the thermal strains during the activation of the elements. An UEXPAN-subroutine [63] is used to describe the thermal strain for each calculation increment, allowing full user control. The subroutine describes the thermal expansion behaviour for all the elements, but applies a cooling-only expansion profile for element which are activated during the analysis (see Section 5.3.1). This way large thermal strains at solidification are avoided and is only build up during the further cooling of the element. The thermal strain builds up during cooling at a temperature below 1000 °C. Above this temperature the mechanical strength is significantly lost, therefore this temperature was taken a the maximum allowable temperature for the thermal strain build up [8, 85, 86].

A more extended overview of the UEXPAN subroutine can be found in Appendix C.3.2.

5.3.6. Implementation of Solid-Solid Phase Transformation

Implementation of the phase transformation can be performed relatively easily once the effect of volumetric changes are known. During the thermal analysis, peak temperatures of the elements are recorded providing a database on which thermal-mechanical behaviour can be based on. A similar approach can be used to record the relevant cooling rate parameters, since the cooling rate can have significant effects on the cooling phase transformation, see Figure 5.5. Similar to the elements which represent the weld pool (Section 5.3.4), this data can be read and used in an UEXPAN subroutine. Different material behaviour curves can be described for different maximum temperatures reached, assigning the relevant expansive behaviour of the material to each separate element.

Whether a phase transformation occurs during heating and cooling of the material is highly dependent on the peak temperature reached [8, 87]. Generally, phase change are considered to occur

when the material has reached a full austenitic phase state. This means that the peak temperature of Ac_3 or higher should have been reached.

Incorporating the phase transformation in the thermal-mechanical analysis have not been applied to the models in this thesis. Harness measurement of the weld, Heat Affected Zone and base material of the experiment performed in this thesis show relative low hardness in the HAZ compared to the base material (see Appendix A). Furthermore, relevant material properties were not obtained in this thesis and therefore the phase transformation was excluded out of the analysis.

However, successful application of the above mentioned suggested approach was achieved by Rikken [88], by using thermal expansion curves obtained from dilatation experiments.

5.3.7. Implementation of Solid–Liquid Phase Transformation

As described in Section 5.3.1, elements which represent the weld pool are only activated during cooling. Using this method, plastic strain build up due to the heating of the elements is prevented, activating the elements without a plastic strain, as if the elements have experienced a plastic strain reset. See Figure 5.12 for visual comparison between this method and the plastic strain reset implementation. Material activation is exactly the same as all the other elements which represent the weld pool, see sections 4.2 and 5.3.4.

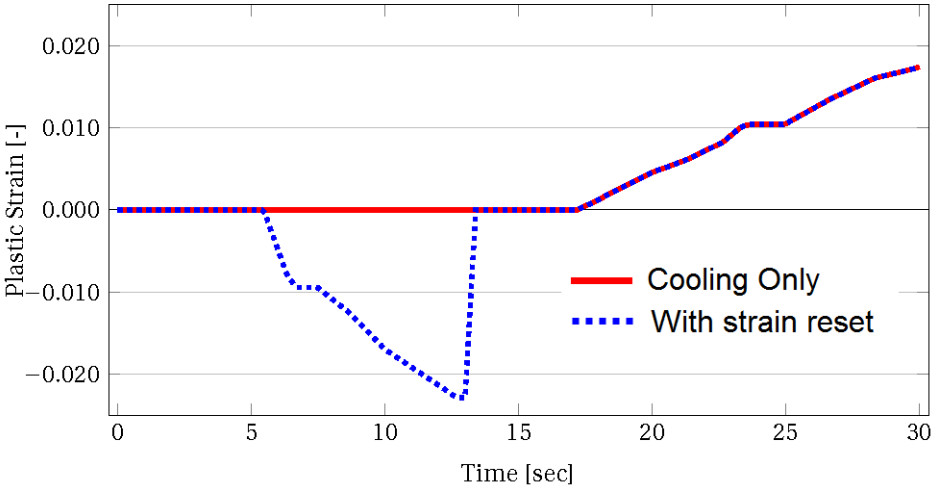

Figure 5.12: The plastic strain build up during the thermal cycle depicted in Figure 5.7 of a bar with strain reset and the plastic build up implemented in this thesis' model.

6

Simulation of Experiment

In this chapter the simulation parameters and results are discussed, simulating the experiments performed at the Material Science and Engineering laboratory of the Delft University of Technology, see Chapter 4 for the set-up of the experiment.

6.1. Meshing

In a heat analysis where relative high temperature gradient are present, a relative dense mesh is required to correctly calculate the simulation results [8]. However, computational time is increased when the number of elements is increased. An optimum solution between simulation results and computational time can be found my means of a mesh sensitivity analysis.

A mesh sensitivity analysis is performed for the elements near the weld, in the welding direction. The analysis shows that by increasing element density above approximately 600 elements per meter, relative stable analysis results are found (see Figure 6.1) where the difference in results is approximately 10 °C. This density is required at the weld, where the maximum temperature gradients are present. From the experiment test results one can see that temperature peak values and temperature gradients decrease very quickly when distance from the weld centre increases. Therefore, density of the elements is reduced in the transverse and longitudinal direction after approximately $8mm$ from the weld centre to decrease computation time of the simulation. In the transition region from fine mesh to coarse mesh, a 2-to-1 ratio transition sections is used to ensure controlled mesh build-up. Figure 6.2 shows the meshing of half the plate, including the transition sections.
Four elements are distributed over the thickness of the plate (See Figure 6.3). This was decided based on previous research [8] and a balance between analysis performance and duration. A thickness of four elements was found to find a sufficient solution to the simulations performed in this thesis. Near the weld element density is increased, using wedge shaped element to be compatible with the triangular shape of the weld.

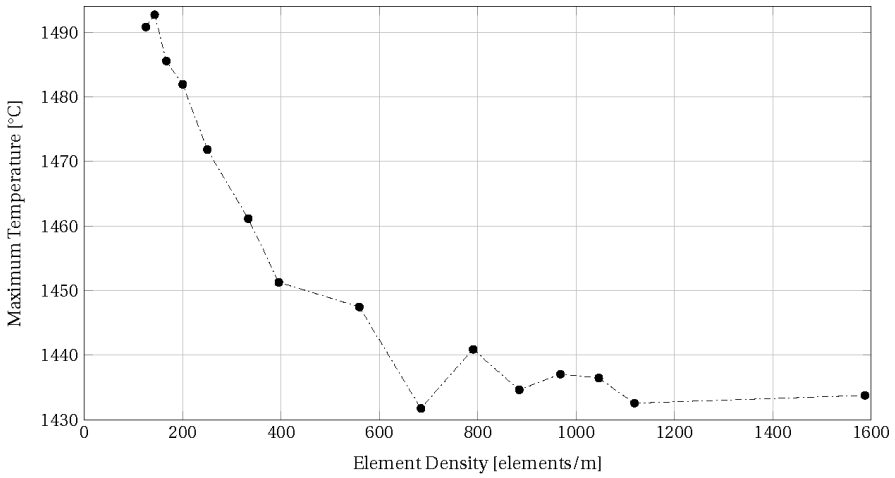

Figure 6.1: The effect of mesh density on the maximum temperature reached in the simulation.

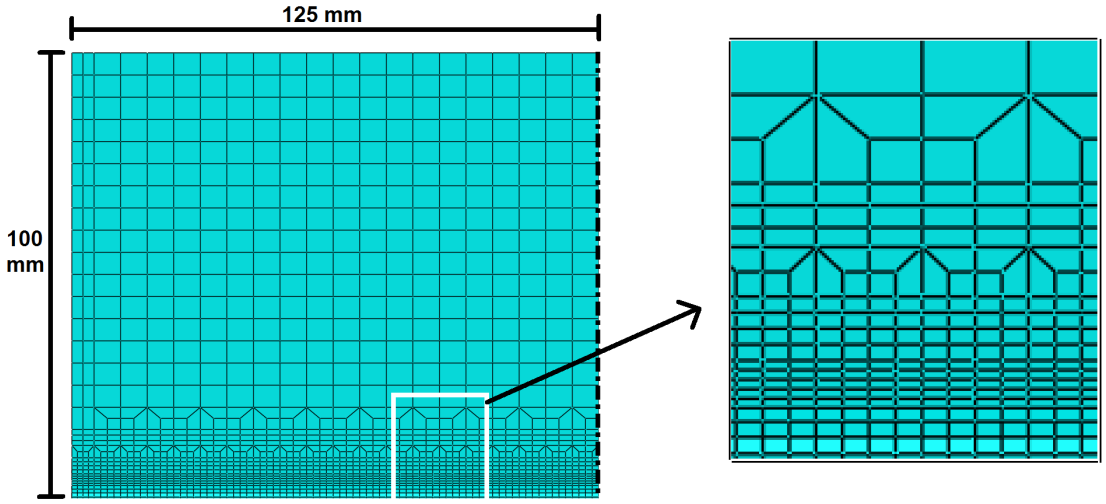

Figure 6.2: Mesh configuration of the model (half-section). The weld is applied at the bottom of the figure, where Mesh density is high.

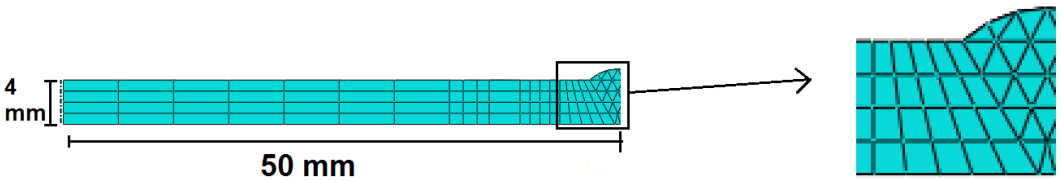

Figure 6.3: Mesh configuration of the model (half-cross-section). The weld is applied at the right of the figure, where Mesh density is high.

6.2. Elements

In this thesis the welding simulation is performed sequentially. The simulation procedure is separated in a heat analysis and a stress analysis. Therefore, in the welding simulation two different types of elements are used, heat and stress solid continuous elements.

The heat elements only hold temperature degree of freedom at the nodes. Both Hexagonal and Wedge shape elements are used in the model. The wedge shaped elements are used to be provide compatibility with the triangular shape of the weld. An 8-node linear heat transfer brick (DC3D9) [63] is used for the hexagonal elements and a 6-node linear heat transfer triangular prism (DC3D6) [63] is used for the wedge shaped element near the weld. See Figures 6.4 and 6.5 for a visual representation of the element.

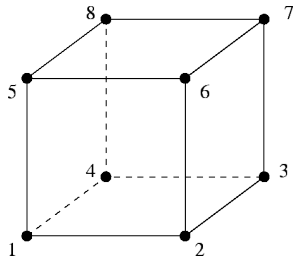

Figure 6.4: A hexagonal shaped element used for the majority of the model in this thesis. [89]

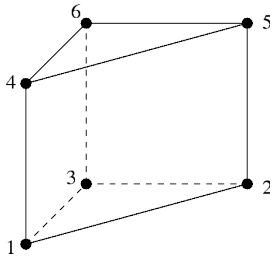

Figure 6.5: A wedge shaped element, used for the triangular shape of the weld. [89]

For the stress analysis, the same mesh as the heat transfer is used. By using the same mesh, no compatibility issues between heat analysis and thermo-mechanical analysis can occur. Furthermore, during the heat analysis, element numbers are recorded to assign separate material behaviour (see Section 5.3.1). Therefore, elements must have the same number-label in both the heat and thermo-mechanical analysis.

In the thermo-mechanical analysis the types of elements are changed to stress based elements. In this analysis the elements make use of temperature-dependent material properties to calculate the stresses. An 8-node linear brick (C3D8) [63] is used for the Hexagonal shaped elements, and a 6-node linear triangular prism (C3D6) [63] element is used for the wedge shaped elements.

6.3. Thermal Heat Flux Parameters

This section will discuss the parameters used for the Goldak heat distribution in the model. Welding power input parameters, derived from the welding power source, are used as the Voltage and Current parameters. As shown in Section 4.4.1 the measured welding power input is approximately 10% higher than the power shown by the power source. Accordingly, a relative high efficiency parameter was expected. Width parameter a of the Goldak shape is set as 90% of half the weld width [43]. Shape parameter c_f is set equal to this size and c_r to two time this size, as many researches used this approximation [8, 19, 43] and found good correlating results. Depth parameter b is set equal to 5 mm, as has been used by comparative research [8]. The welding input fraction is distributed from 0.6 to the front section and 1.4 to the back. The Goldak heat source speed is set equal to the experimental travelling speed of 5 mm/s. After 2D and 3D efficiency parameter calibration, as described in Section 5.3.2, a welding efficiency of 1.0 was found to match thermal results sufficiently. See Table 6.1 for an overview of the different parameters.

Table 6.1: Overview of the Goldak parameters used in this research

Voltage	22.1	V
Current	170.0	A
Efficiency	1.0	-
Width (a)	5.82	mm
Depth (b)	5.0	mm
Front (c_f)	5.82 (= a)	mm
Back (c_r)	11.64 (= 2*a)	mm
Welding Speed	5	mm/s
Front Fraction	0.6	-
Back Fraction	1.4	-

6.4. Thermal Boundary Conditions

All thermal losses of the plate are modelled in an implicit manner. Accordingly, all thermal losses are represented by thermal boundaries and expressed as thermal convection and radiation (see Section 5.1.1). To simulate the experiment as close as possible thermal boundary conditions have been based on the conditions of the plate during welding. The steel on steel contact of the clamping system is assumed to be of high conduction losses. Due to the relative high volume of the clamping plates, no increase of the temperature of the clamping is assumed. An uniform convection of 50 W/m^2K is assumed where the clamping is present. For DIC distortion measurement, paint was applied at the top surface of the freely deformable plate. The painted area is assumed to have a convection coefficient of 20 W/m^2K. At the weld root, ceramic backing was present and a low convection rate is assumed; a convection coefficient of 10 W/m^2K is used. All other surfaces, which are in direct contact with the surrounding air are assumed to have a thermal conductivity coefficient of 20 W/m^2K. All the chosen thermal boundary conditions are assumed based on prior research done in this field [8, 19, 43]. For radiation, a emissivity of 0.9 was used where the welded plates were not in contact with either the clamping or the ceramic bricks [8]. The radiation coefficient parameter may vary significantly in different research, but changing the parameter does not significantly change the stress results in the simulation [19].
Figure 6.6 shows the exact locations of the applied thermal boundary conditions.

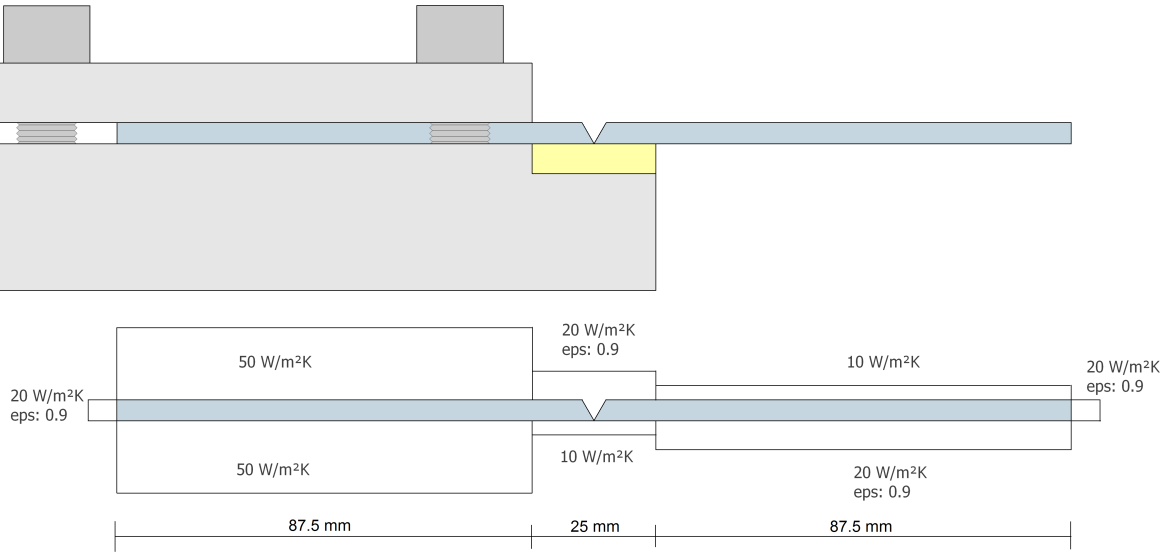

Figure 6.6: The thermal boundary conditions as applied for the experiment model. Convection coefficient are shown, together with the thermal radiation coefficient (eps), when applicable.

6.5. Transient Thermal Results and Comparison

Figure 6.7 and Figure 6.8 present the experiment and FEM results of the thermal analysis. As can be seen in Figure 6.8, thermal measurement and 3D simulation results show an overall sufficient match of results. A maximum difference is found at the thermocouple of 10 mm from the weld centre, where a maximum difference of 30°C is found. The fitting parameter, the welding power efficiency, is found based on a 2D heat analysis (see Section 5.3.2). The maximum difference between 2D and 3D thermal results is an approximate 150°C. The temperatures of FEM and measurement results reach it peak value on the same time; it demonstrates a matching temperature distribution over time towards the transverse direction in the material. The experimental thermal couple measurements close to the weld, at 3 and 5 *mm* from the weld centre, show different peak results. This may be caused by inadequate thermal couple to specimen attachment, or measurements exceeding the measurement capability of the thermocouple. Temperatures in the 2D model are generally higher compared to the 3D model results. This may be explained through the heat losses in the longitudinal direction in the 3D model, the out-of-plane direction in the 2D shell model.

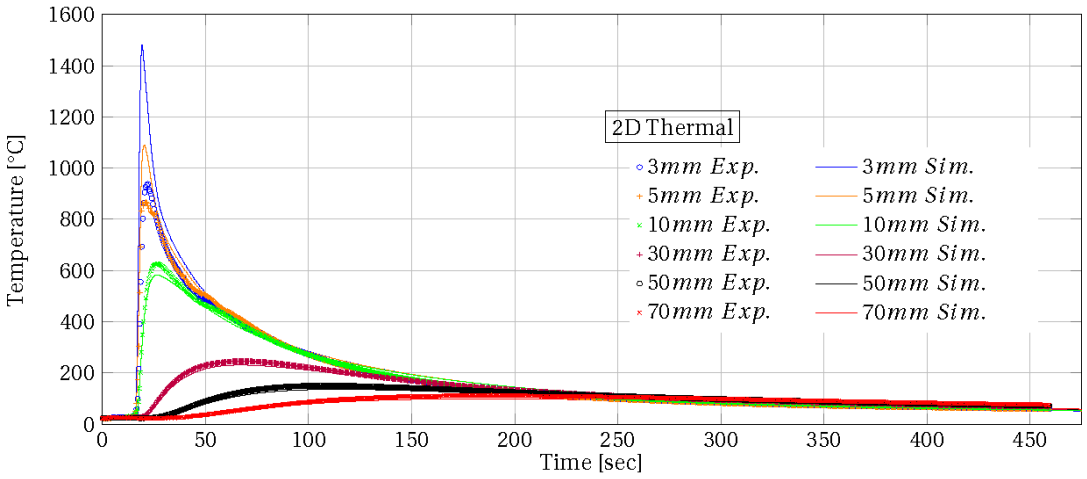

Figure 6.7: The thermal experimental measurement and 2D simulation results compared with each other.

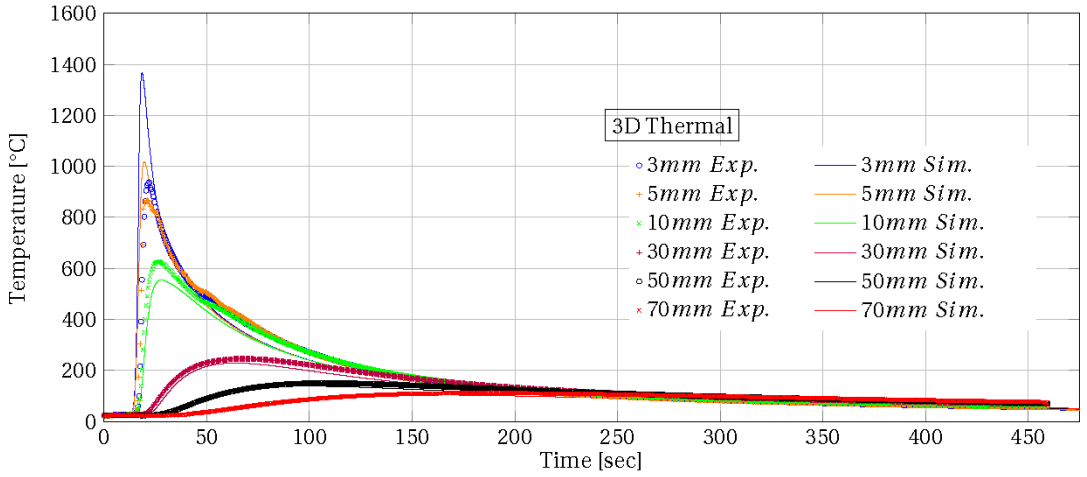

Figure 6.8: The thermal experimental measurement and 3D simulation results compared with each other.

6.6. Distortion Results and Comparison

6.6.1. Transient Deformation Measurement

Comparison of experimental and simulated results show both a similar distortion build up during and after the welding process. Two sections can be distinguished: a relative quick build-up of distortion until approximately 50 seconds and a slower build-up of distortion after these first 50 seconds. The first section of distortion growth corresponds with the welding process and thus the presence of the welding arc. High temperatures are reached and large temperature gradients are present once the arc has passed (See Figure 6.8). The combination of a large temperature gradient and relative high temperature will cause significant distortion in the initial phase, just when the arc has passed.

A sudden change in distortion gradient can be observed at around 50 seconds, the moment when the arc has passed the specimen. The specimen is now absent of the large thermal gradients of the welding arc and thus distortion increase has (rapidly) slowed down. After this moment, strains are slowly building further up in the specimen due to the cooling process. The build-up of longitudinal and transverse stress predominantly define the distortion of the specimen (see Figure 6.12), causing a gradual buckling shape which defines the final distorted plate.

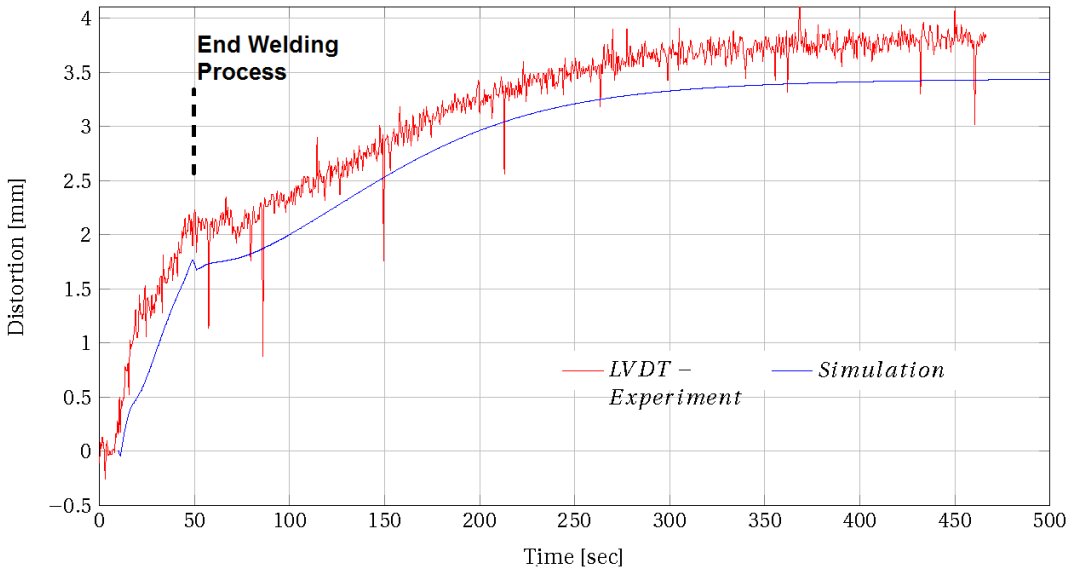

Figure 6.9: The LVDT deformation results compared with transient simulation results of the same location.

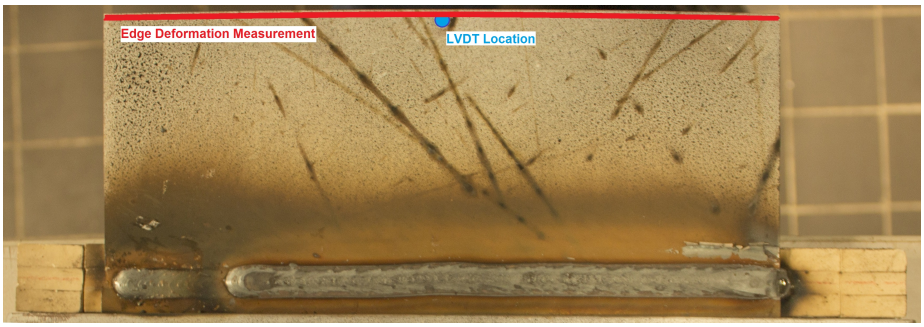

Figure 6.10: The dot indicates the location of LVDT measurement. The line indicates the location of the static deformation measurements.

Figure 6.11 show the comparison between LVDT and simulation distortion results. A large difference at the first 50 seconds of the welding process. A maximum difference of around 60% is found, which is a difference of approximately 0.7 mm. After the first 50 seconds, differences in results stabilise to an approximate 10%, which translate to a difference of approximately 0.4 mm.

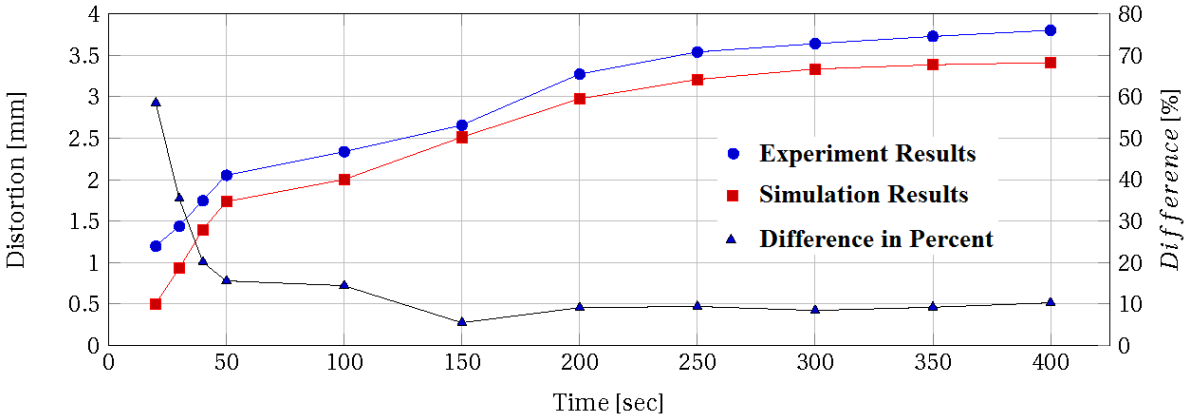

Figure 6.11: LVDT (blue, circle) and Simulation (red, square) results compared with each other. The difference of the results are presented in percentages (black, triangle).

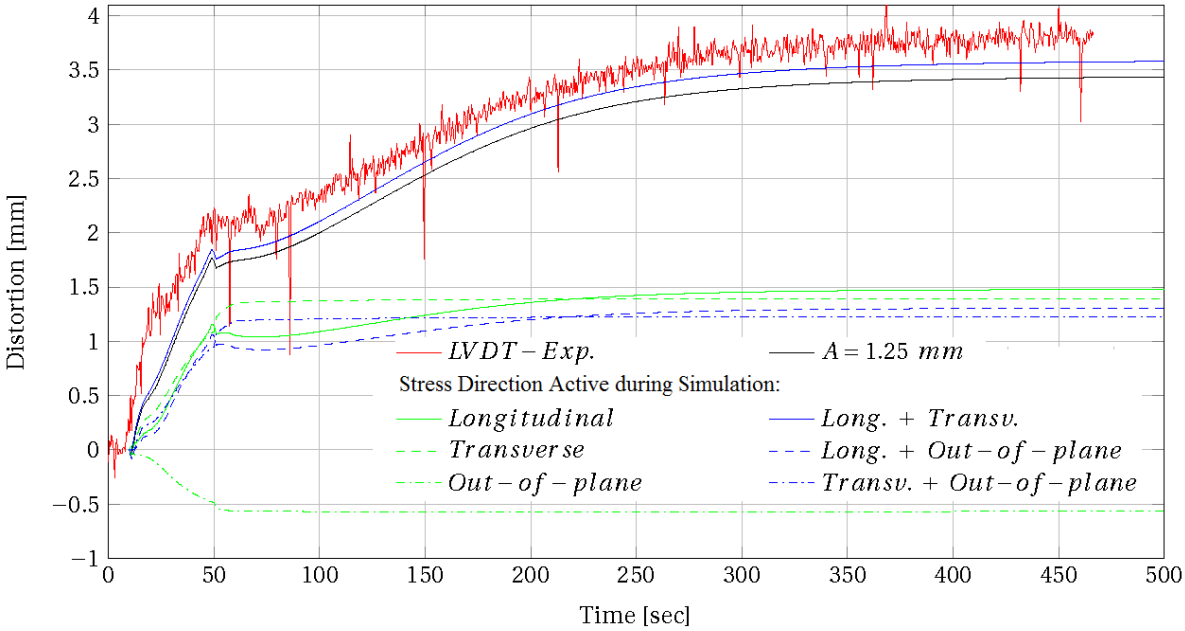

Figure 6.12: Results of transient deformation simulation where the three main stress directions (Longitudinal, Transverse and Out-of-plane) are separately de-activated in the analysis.

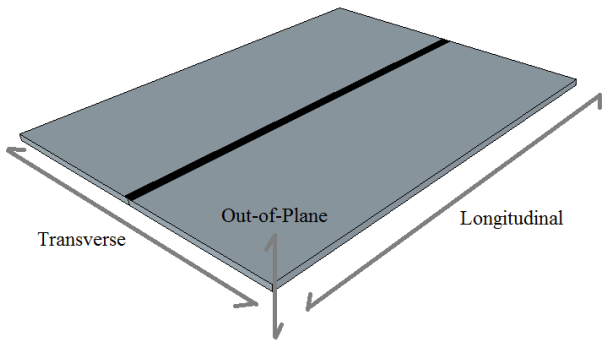

6.6.2. Boundary Condition Uncertainties

An investigation of the constrainment of the plates after welding showed small out-of-plane distortions of the specimen between the clamping plates, approximately 0.1 mm. This is most likely caused by uneven surfaces of the contact areas of the plates in combination with small deflections of the clamping plates.

As a consequence, the anticipated (stiff) boundary conditions of the model showed simulation results which were not in good agreement with experiment distortion results (see Figure 6.13, *full*). Distortion of a freely constrained plate showed distortion results also no agreement, thus a new a boundary condition had to be found.

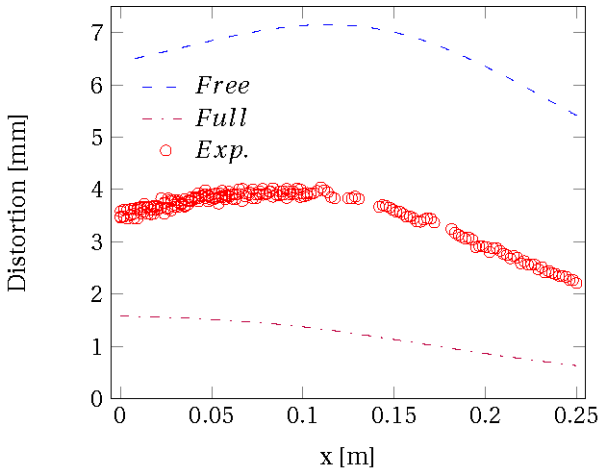

Figure 6.13: Comparison between free constraint, full constrain and experimental data of the welding distortion at the outer edge. A significant influence of the boundary conditions on the final amount of distortion can be observed.

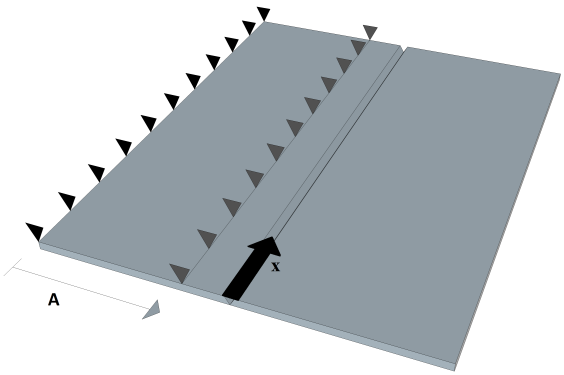

Figure 6.14: Visual representation of the out-of-plane boundary condition of the plate model. Where the free constraint is distance A equal to zero. The full constraint condition is A set equal to the experimental clamp; 86 mm

As a result of the out-of-plane movement of the plate specimen between the clamping plates, boundary conditions were difficult to derive from the experiment. Clamps could not be removed to investigate further, since further experiment on the plate was required. Therefore, boundary conditions were varied by trial-and-error to find matching results between simulation and experiment.

Matching results were found by applying out-of-plane boundary conditions which consist of two fully constrained lines (seen Figure 6.14). One line is placed at the plate edge, as in the experiment close to this edge bolts were present, constraining the plate. The other line is located parallel to this line on the plate model. Distance between the lines is varied to find a good agreement of distortion results (distance A, see Figure 6.14), starting from a distance of 86 mm, similar to the experiment clamp. A good agreement was found with a minimum distance between the lines of $A = 1.25$ mm (see Figure 6.16).

Distortion positive and negative directions, as used in this thesis, can be found in Figure 6.15.

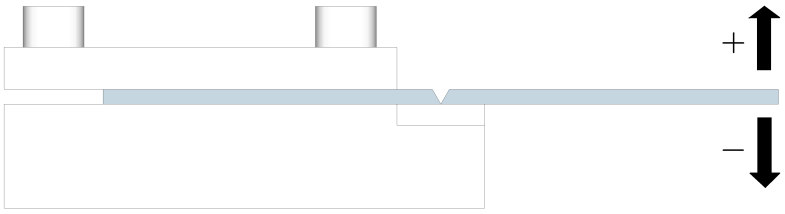

Figure 6.15: Indication of the positive and negative distortion due to the welding process, as used in this thesis.

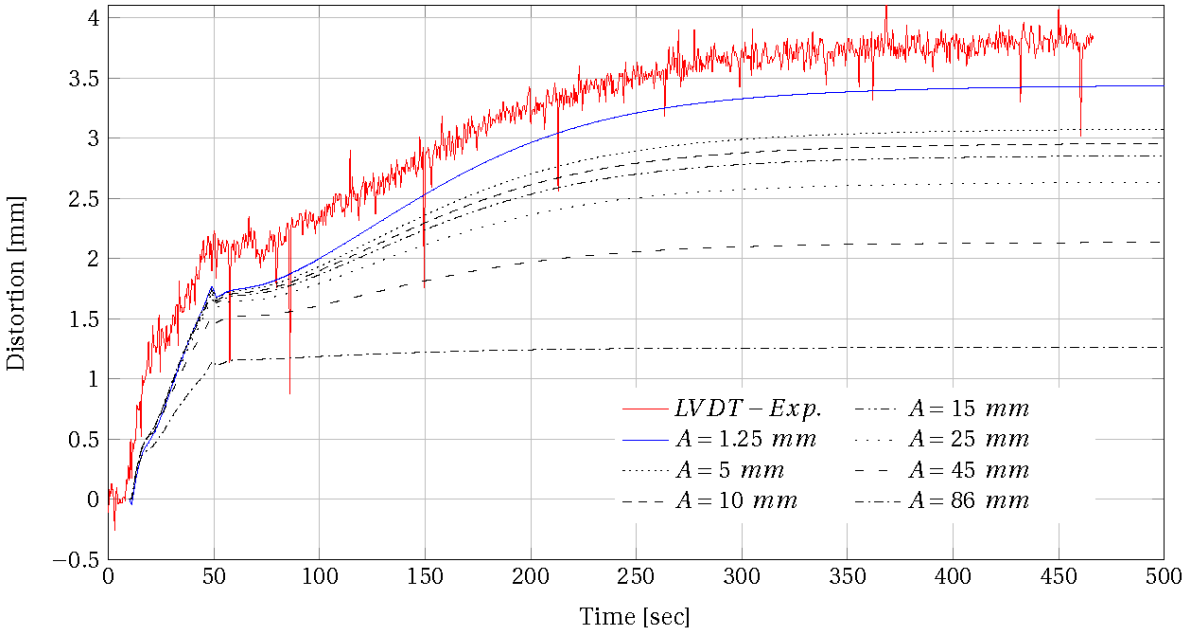

Figure 6.16: Welding distortion results dependent on the boundary conditions, see Figure 6.14 for distance A.

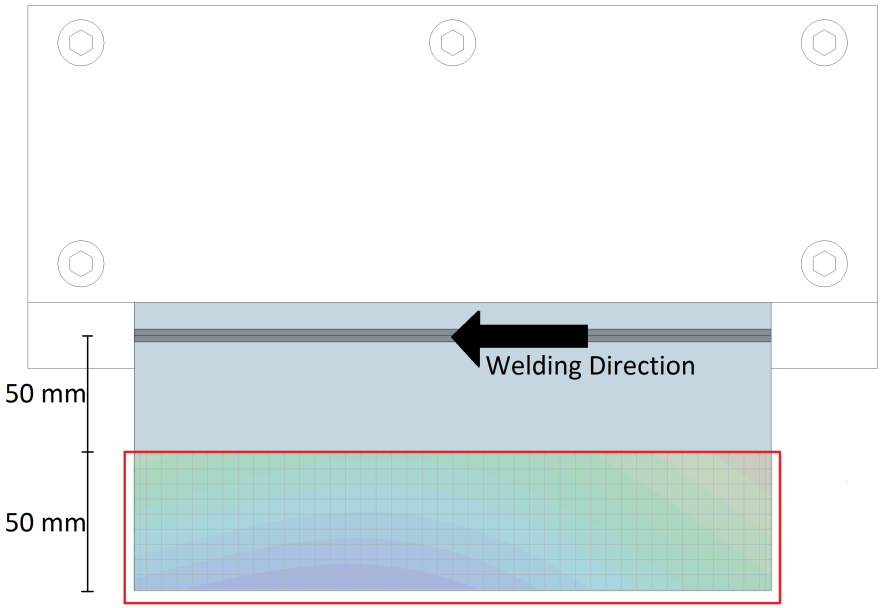

Figure 6.17: Top view of the welding clamp which shows the location of the displacement field results shown in Figures 6.18 and 6.19

6.6.3. Static Distortion Data

In Figures 6.18 and 6.19 show a Finite Element contour plot and the DIC data points, respectively. The measurement area on the plate of these distortion can be found in Figure 6.17. Distortion results of the simulation are a lower than experiment results, as was also observed with the LVDT measurement (see Figure 6.9). An overall agreement between simulation and DIC results is found.

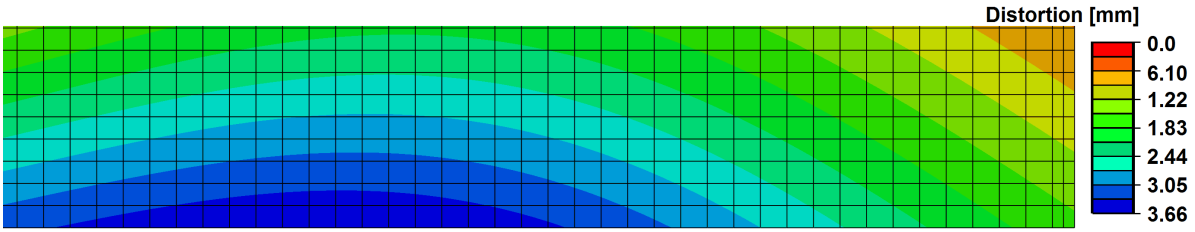

Figure 6.18: Contour plot results of the distortion of the simulation.

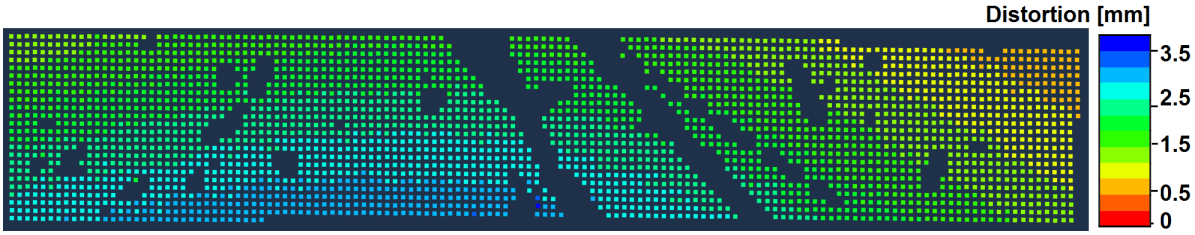

Figure 6.19: Scatter plot of DIC distortion measurement points on the distorted plate. Colours correspond with the legend of the contour plot of Figure 6.18

A further comparison is made by comparing distortion results of DIC, LVT and calliper measurement with the simulation results. A comparison is of the distortion at the longitudinal edge location of the plate (see Figure 6.20). A overall good agreement between experiment measurements is found. Calliper measurement show a maximum difference of approximately 30% for a single measurement point, but overall results are in good agreement. DIC measurement points may seem to spread in the graph, but this is due to the location of the measurement points on the specimen. Finite Element results show similar distortion of the plate.

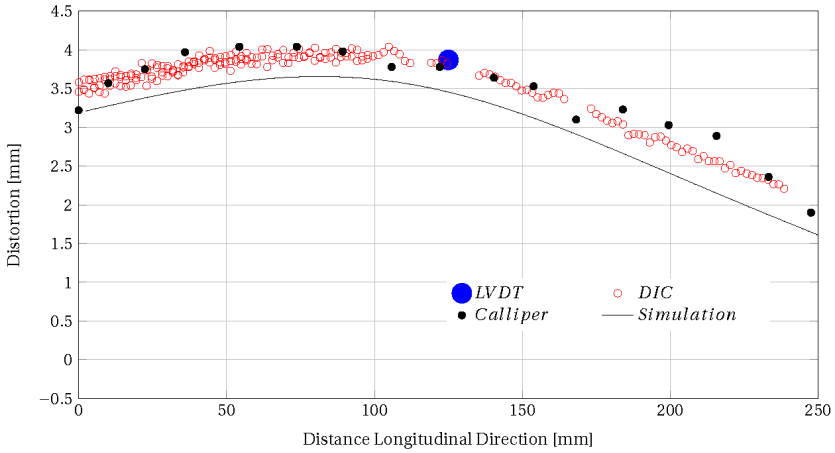

Figure 6.20: Static distortion measurement results of the different distortion measurement methods. See Figure 6.10 for the measurement location.

6.7. Discussion

6.7.1. Activation Moment

A parametric analysis is performed on the moment of activation of the element which represent the weld pool. The parametric analysis in this section will investigate the influence of this start temperature (and thus the amount of thermal strain) on the stress build-up once material stiffness is increasing.

As discussed in Section 5.3.1, elements which represent the weld pool only experience cooling in this model. As cooling of the element is started, temperatures decrease and as a result temperature-dependent Young's modulus is increasing, effectively activating the element. During activation of the element, also the thermal shrinkage start point has to be set (see Section 5.3.5). The amount of thermal shrinkage is dependent on this start temperature since $\epsilon^{th} = \alpha \cdot \Delta T$.

To compare the effects of the thermal strain activation temperature, 20 analyses have been performed ranging from an activation temperature from 100 to 2000 °C. Results can be found in Figures 6.21.

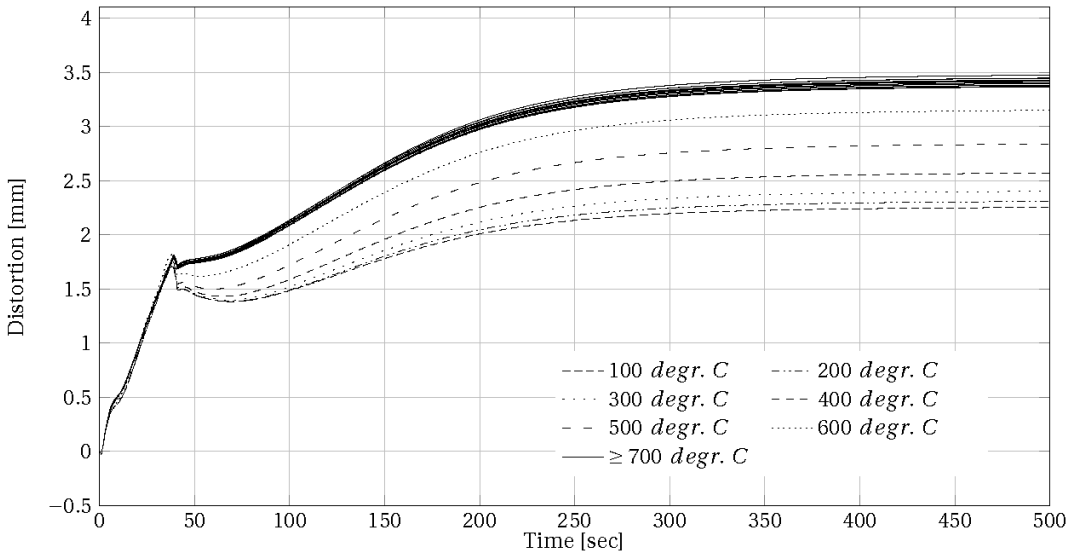

Figure 6.21: The effect of simulation activation temperature on distortion.

Distortion results show relative steady results when activation occurs at a temperature of 700 °C or higher. A further comparison is made between the analyses by comparing the stress results. The compared analyses all experienced a thermal expansion activation temperature of 700 °C or higher, therefore having similar distortion result. The Von Mises stress contour plot is presented in Figure 6.22 together with stress level over two different locations in Figure 6.23 and 6.24. Again, no significant differences in the stress fields can be found.

Distortion and stress results show relative steady results when activation occurs at a temperature of 700 °C or higher. This corresponds with the loss of Young's modulus at this temperature, as used for the material properties in this model (see Figure 4.1). Futhermore, in this model a perfect plastic behaviour is used for the plastic build up. As a consequence, any plastic zone in the model has the same strain and has an similar effect on the model stress results.

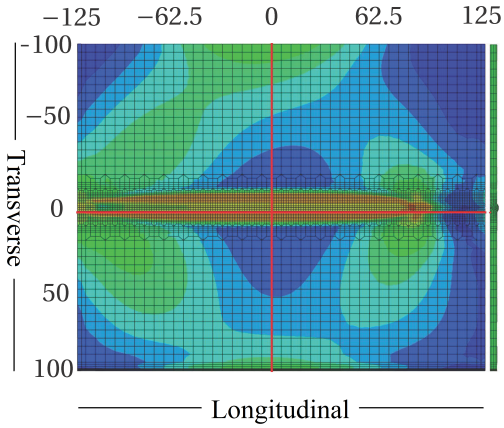

Figure 6.22: Bottom view of the Von Mises stress of the welded plate. The two red lines indicate the location of the stresses in Figure 6.23 and 6.24.

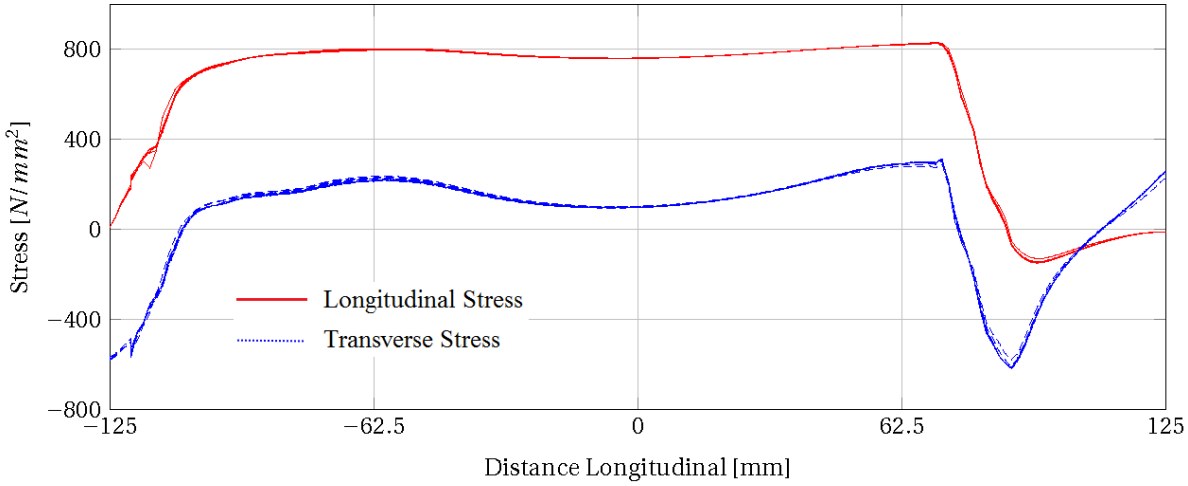

Figure 6.23: Stresses along the vertical red indication line of Figure 6.22. Analyses with activation temperature between 700 and 2000 °C are represented in the figure.

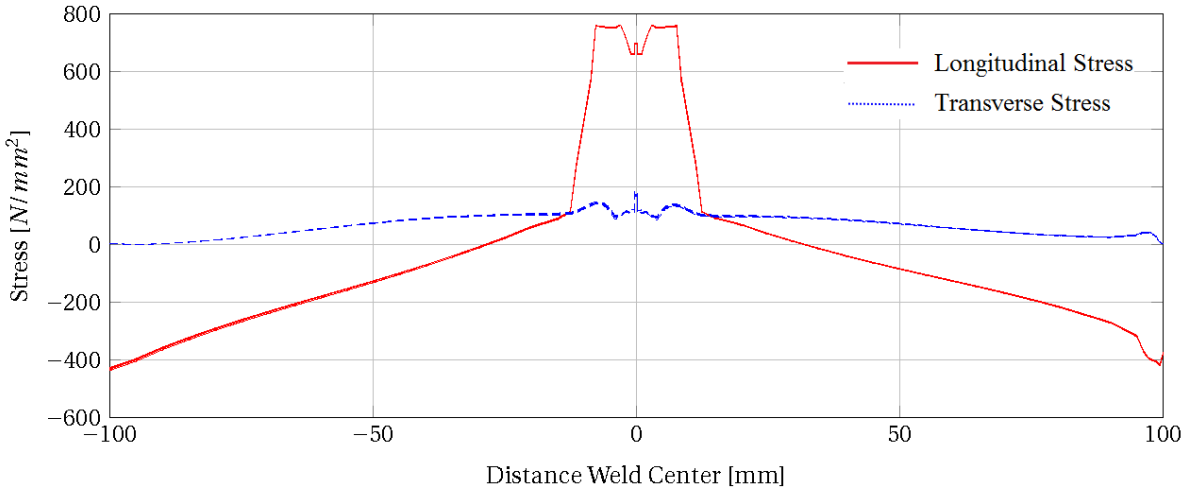

Figure 6.24: Stresses along the horizontal red indication line of Figure 6.22. Analyses with activation temperature between 700 and 2000 °C are represented in the figure.

6.7.2. Investigation of Transverse Thermal Distribution in a 3D model

In Section 6.5, a good agreement was found between 2D and 3D thermal simulation results compared with temperature measurement from the welding experiment. These measurements were based on the thermocouples which were placed transverse on the plate, at a single location in the longitudinal direction of the weld (see Figure 4.5). Since only transverse distribution of temperatures is regarded in the experiment, a simulation investigation is performed to question the variance of the thermal results in the longitudinal direction of the weld. The focus is on peak temperatures reached during the thermal-cycle, at the locations of the thermocouples as placed during the experiment of the initial weld (see Figure 4.5). Transverse temperature at the transverse locations of the weld, as a the weld progresses. Figure 6.25 show the thermal peak results of the 3D model results parallel to the weld, at a fixed distance from the weld centre. A clear stable section of peak temperature results can be found in the figure. Only at the start, where the heat flux is introduced, lower peak values are found. At the end of the weld, where the plate ends, higher temperature peak values are found. Heat cannot dissipate due to a lack of material and thus temperature increases.

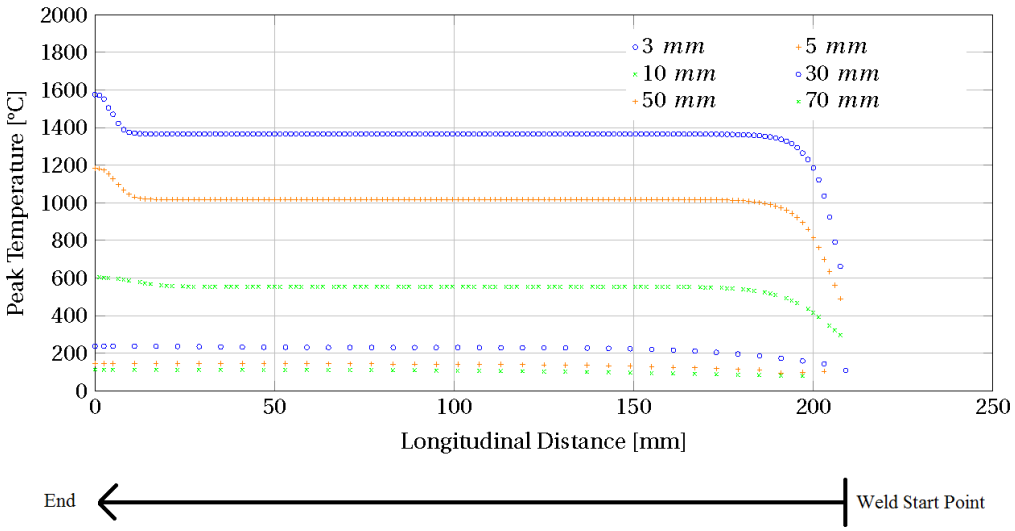

Figure 6.25: The peak temperature values at the location of the thermocouples, at every location along the weld in longitudinal direction.

In the model of this thesis, the factors which can have an significant effect on the thermal results are constant, which contributed to the constant values found in Figure 6.25. The factors are temperature-dependent thermal properties, heat flux, plate geometry and thermal boundary conditions. For a full analysis, further simulation work needs to be performed to investigate the influence of the aforementioned factors, and results have to be verified through experiment. The simulation results show an equilibrium state on the temperature distribution of the transverse direction on the plate. In this model, the equilibrium state is found at approximately 30 mm from the weld start and 25 mm from the end point. Further simulation work needs to be performed to find a possible relation between the heat model influencing factors and the possible equilibrium state of temperature distribution.

6.7.3. Improvement on Clamping Constrainment

Improvement Experiment Clamps

As discussed in Section 6.6.2, out-of-plane movement was observed between the plate and clamps. This caused uncertainties in the simulation model and a fitting boundary conditions had to be found. In this section some suggestions for improvement of the clamps are made.

Improvements can be made by ensuring full surface connectivity between the clamping plates and the specimen. The stiff nature of the steel plates make a full surface contact relatively difficult, since relative small imperfections can lead to separation. A more flat surface can be created by machining the plate surfaces, but small distortion will almost always be present.

By putting pressure on the clamping plates, small openings between surface of the clam and specimen may be removed. However, this applied pressure has to be know, since ultimately the experiment is modelled in FEM software. Considering the used clamping plates in this thesis (see Figure 4.5), the bolts have to be pre-stressed to ensure sufficient pressure on the specimen plate. The pre-stress of the bolts can be determined by calibration of the bolts before the specimen is clamped, such that strain measurement can determine the relation of pre-stress and the torque applied on the bolt [90]. Another approach is by stressing the plates continuously by hydraulic clamps. The portability of the specimen and clamp is then lost, but pressure on the plate can relatively easy be controlled and maintained.

Putting pressure on the plate may induce significant (local) forces, making the clamping plates susceptible for bending. Stiffness of the plates have to be increased. By increasing the plate thickness stiffness is increased, but a more weight efficient solution would be to apply stiffness plates, which can prevent distortion of the clamps.

Improvement Simulation of Clamps

A more explicit simulation of the specimen clamps can aid in defining correct and close to reality boundary conditions. The clamps can be fully modelled in the FEM software, such that stress in the plate are accounted for in the simulation. Another (more implicit) manner of defining the clamps is the use of spring-boundary conditions.

Modelling the clamps explicitly in the model has the advantages that is can take into account the specimen-to-clamp separation, allowing for out-of-plane movement. The in-plane movement can be modelled by friction between clamp and specimen. A significant disadvantage of the full simulation of the clamps is the increase in calculation time of the model. Another disadvantages of this full simulation, especially when considering specimen-to-clamp separation, is that the amount of pre-stress or pressure applied by the clamp of the experiment has to be known. This can be acquired by experiment, by for example determining the pre-stress of the bolts clamps or by use of hydraulic clamps on which the pressure it can apply, can be defined.

The use of spring-boundary conditions on the element will be more computational efficient compared to the full explicit modelling of the clamps. However, the stiffness definition of the springs must be defined to resemble the clamping plate stiffness. A good (analytical) approximation for the spring stiffness definition for, as an example, a specimen clamped between two plates and two

bolts can be using the definition for beam distortion (see Equation 6.1 and Figure 6.26). Using the approximation, a spring stiffness can be derived dependent on the spring location and taking into account the bending of the clamping plates.

$$\delta = \frac{2 \cdot F \cdot a^3 (L-a)^2}{3 \cdot EI(2a+L)^2} \longrightarrow k_{spring} = \frac{F}{\delta} = \frac{3 \cdot EI(2a+L)^2}{2 \cdot a^3 (L-a)^2} \tag{6.1}$$

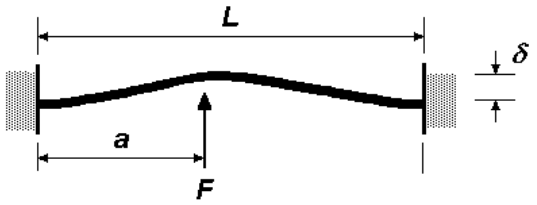

Figure 6.26: Distortion definition of a fixed-fixed beam subjected to a point load which can be used to approximate spring stiffness in out-of-plane direction. [91]

6.7.4. Simulation Results

As was shown in Section 6.6, the final distortion difference of results between experiment and simulation are approximately 0.4 mm, an approximate 10% in difference. Boundary conditions were found which resulted in this distortion, but other factors and choices made in this model can lead to difference in distortion results. In this section these influencing factors are discussed.

The material properties have been acquired by JMatPro software and are expected to not perfect match the material properties of the used specimen. Most importantly the difference in plastic behaviour is expected to be of significant influence. In this thesis the plastic behaviour is assumed to be perfect plastic, no strain hardening occurs. Since the residual stress are dependent on the plastic zones 2.1.1, this choice may be of mayor influence. If (realistic) strain hardening is implemented, it is expected that higher stresses in the plastic zones are reached. This, in turn, will increase the overall residual stresses in the specimen since an equilibrium of stresses is found. This increase of stress will induce more force on the plate which causes distortion, thus more distortion is expected when strain hardening is applied.

The approximated weld pool of the Goldak heat distribution was a different shape compared to the cross-section of the weld made afterwards (see Figure 6.27). In the simulation, the Goldak was altered without looking at the cross-section since this was not available at the time. In the cross-section of the welded plate are more triangular weld pool is found compared with a more trapezoidal weld pool in the simulation. The more triangular shape could induce more distortion due to transverse stresses, since the resulting force is most likely more eccentric from the mid-section of the plate. Comparing the cross-section of the weld further, simulation and experiment show a good agreement of the HAZ.

The Goldak shape parameters can be altered to approximate the shape of the (real) weld pool in the simulation. This was not incorporated in this thesis since the cross-section of the welded plate was made in a later stadium of the thesis, and alternation could not have been examined in the then available time.

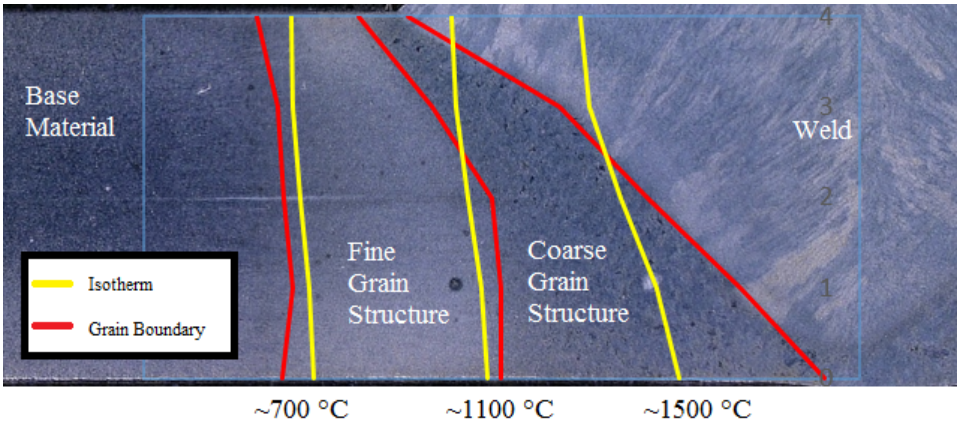

Figure 6.27: Comparison between thermal field (yellow, with temperature of isotherm) and HAZ (red) of the experiment weld. [92, 93]

The cooling only shrinkage of the weld pool can have a significant effect on the welding distortion. As discussed in Section 5.2.1, the activation of the weld pool elements is only during the cooling phase. Thus, heated base material also does not experience any mechanical effects from heating. The lack of expansion during this heating phase of the elements is expected to have relative little effect on the distortion since relative free expansion is possible (see Section 5.3.1). This however, is not verified in this thesis.

7

Repair Welding

In this chapter the different aspects of application and simulation of repair welding is discussed. First an introduction to repair welding is be given, followed by the explanation of the performed experiment. After which the repair weld simulation approach will be discussed, and distortion of experiment and simulation are compared.

7.1. General

Reliable welds in a structure must be achieved to meet Safety Design Criteria. In order to ensure the quality of the weld in a structure, an quality assessment of the weld can be performed [40]. Accordingly, two main quality testing methods can be used: Non-Destructive Testing (NDT) and Destructing Testing (DT). Generally during the fabrication of a steel section NDT measurements are performed, as DT measurements destroy the welds.

After assessment, the weld may not meet specified weld requirements, due to a weld failure. Examples of weld failure are (relative large) inclusions within the weld, or cracking of the weld during or after the weld process. If a failure is found, the choice can be made to perform a weld repair procedure to remove the weld defect and repair weld the removed section. Whether a repair weld can be made can depend on the location and the nature of the defect [94].

Once the choice is made to perform a weld repair procedure, the weld defect has to be removed from the weld. The material removal is commonly performed by a grinding, gouging or a combination of these processes [95]. The grinding process is performed by either an abrasive or non-abrasive machining process. An abrasive machining process makes use of an abrasive medium to remove material, for example a disc grinder. The abrasive material which separates from the disc wheel during grinding may contaminate the welded material and should be cleaned thoroughly.

An example of a non-abrasive method is using a burr-grinder. The grinder head may have shape which helps with the desired shape of the welded section, making for example a groove of a U-shape.

Gouging or arc gouging is the removal of material by forming a small molten metal pool and removing the liquid metal by use of a gas stream. This process introduces relative large amount of heat in the surrounding material. One should take care of this added heat since it can change material properties of the surround material. The formed relative rough edge and slag of the gouging

process can be removed by use of a grinding process after the gouging process, to ensure a smooth finish. [40, 95, 96].

After material removal, the created weld groove is thoroughly cleaned. The groove and surrounding material is checked by use of NDT to ensure that the defect is completely removed and no additional defects have occurred due to the removal process [94]. Once checked, the groove is welded together forming a new connection between the material. After repair welding the weld is again checked by use of NDT, to determine whether the weld qualifies for the weld requirement.

7.2. Experiment

7.2.1. Material Removal Procedure

For the repair procedure experiment the same specimen used for the welding procedure, described in Chapter 4, will be used. As described in Section 4.4, a weld defect was (without intention) created due to a welding malfunction.

The repair procedure is located at the previously describe defect of the weld. Removal start at about 15 mm from the beginning of the weld, to prevent the possibility of separation of the two welded plates due to residual stresses in the weld. The removed groove is of 2 mm depth, half the depth of the plate (see Figure 7.1). The length of the removed material is half length of the weld, approximately 125 mm (see Figure 7.2).

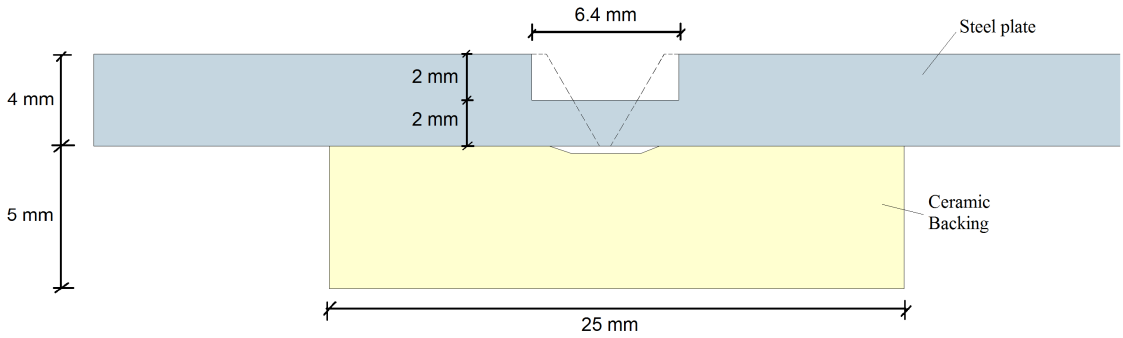

Figure 7.1: The geometry of the removed section. The location of the V-shape butt weld of the initial weld is shown for reference.

A controlled manner of material removal was achieved by use of a milling process (see Figure 7.3). Width and depth can be accurately controlled which ensures constant geometry of the removed gap. Furthermore, the milling process can be performed relatively slow, such that generation of heat, can be mitigated.

First the weld cap was removed, after which the weld was removed. Two end-mills (flat bottomed cutters) of 17.5 and 6.4 mm diameter were used respectively. Each removal was performed as one continuous milling process at a continuous speed of approximately 1 mm/s.

Figure 7.2: Photo of the removed section of the plates. The initial weld was performed from the right to left side of the plate.

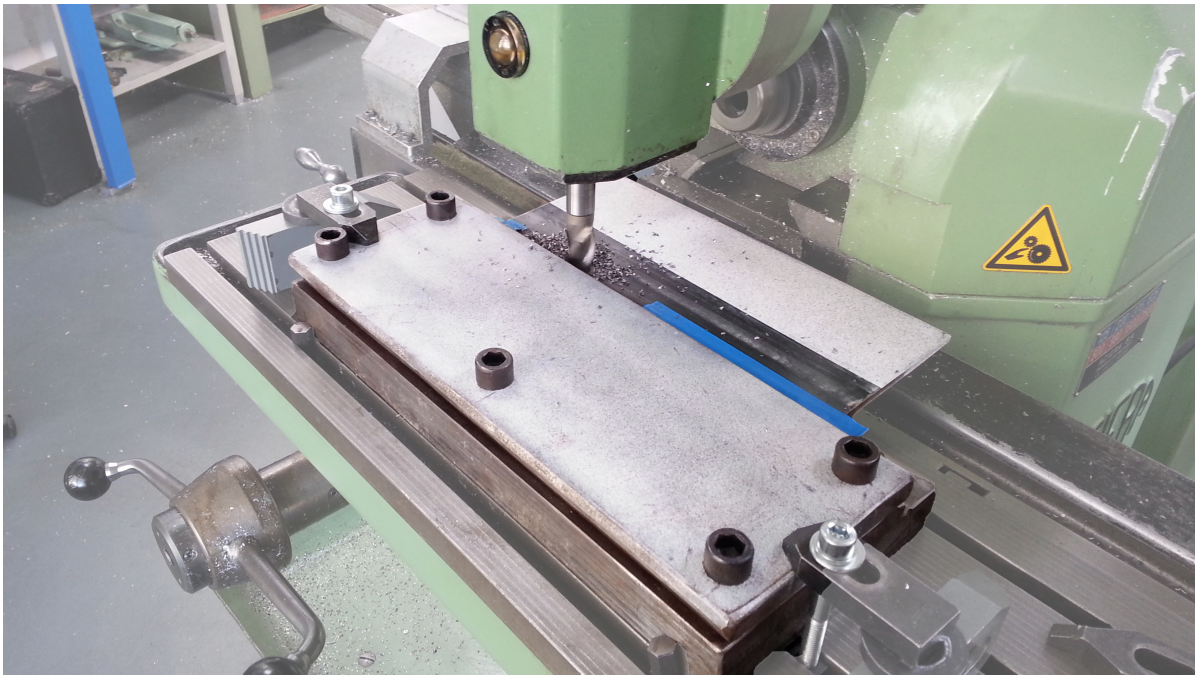

Figure 7.3: Photo of the removal of the section by the milling process.

7.2.2. Distortion Measurement Results

Distortion measurement by Digital Image Correlation (DIC) is performed after the removal process. DIC measurement have been made similar to the condition of measurement as describe in Section 4.4.3. The relative distortion due to removal of weld section can be found in Figure 7.4 and Figure 7.5. The measurement is relative to the distortion after the initial weld.

The distortion results show a relative distortion similar to the negative direction of the (buckling) distortion of the initial weld experiment, see section 6.6.3. Due to this shape of distortion, following the negative buckling curve, the distortion initiated through the removal of the weld material is likely to have a relaxing effect on the stresses which causes the buckling behaviour. These stresses are of compressive nature in the longitudinal direction [43].

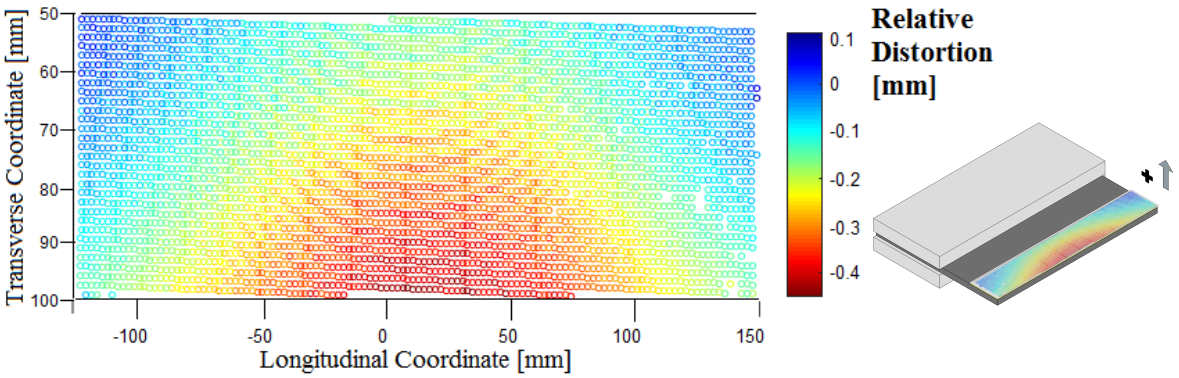

Figure 7.4: DIC distortion results after weld removal. Please note that the displaced is relative to the distorted plate, after welding.

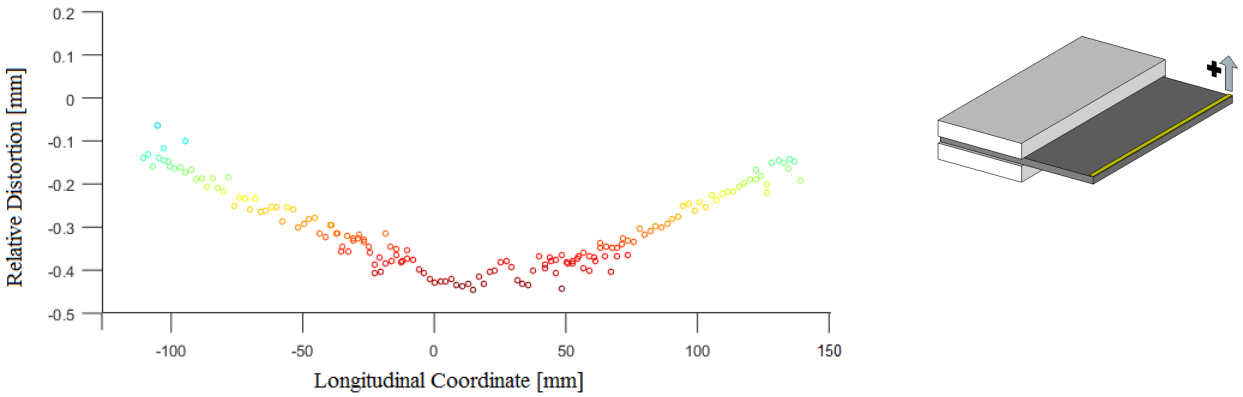

Figure 7.5: DIC distortion results after weld removal. Please note that the displaced is relative to the distorted plate, after weld removal. The results are shown of the outer most edge of the distorted plates, the outer lower edge on Figure 7.4.

7.3. Simulation

The simulation of material removal can be performed in multiple ways, varying from a detailed to a more general approach. An example of a detailed simulation is the simulation of the mechanical interaction between material and removal tool. The fine tearing and cutting process can be modelled, including local effects which appen during the process [97, 98]. Another example is the simulation of the induced effects only, for example with large surface material removal [99, 100]. A large surface material removal process can be simulated, by use of relative simple element de-activation. The heat induced by the process can be simulated by applying a heat flux. Which level of accuracy regarding the simulation is needed depends on the used removal process and the desired information of the simulation.

In this thesis material removal is simulated by a general approach: by element de-activation only. This is possible due to the chosen way of removal in the experiment. Since effects like heat generation during the removal process was kept to a minimum by using the milling process, it is assumed that de-activation of element is sufficient to simulate the weld removal.

7.3.1. Simulation Approach

The de-activation of the element is performed by using the model change function within the Abaqus environment [63]. The model change function allows the user to remove segments of the model, similar to the birth-and-death activation of element as discussed in Section 5.2.1. Abaqus will calculate the re-distribution of stresses within the model to find a new equilibrium stress state.

In the model, first the weld cap was removed after which the weld itself was partially removed at a depth of 2 mm in the material and a total width of 6.4 mm, similar to the experiment (see Figure 7.1).

7.3.2. Simulation Results and Experiment Comparison

Simulation results can be found in Figure 7.7, for comparative reason the relative distortion of the removal procedure is presented. Simulation and experimental results show a clear and significant difference, a maximum difference of 0.35 mm is found an approximate 100% difference in results. The experiment shows a concave shape downwards, while the simulation presents a convex shaped distortion.

As discussed in Section 7.2.1 the distortion of the experiment results may be because of relaxation of stress which induce the buckling shape. This would mean that some stresses where created in the faulty section. A stress where it was assumed zero in the initial weld simulation.

As an example, the same material removal procedure in the simulation is applied to the welded part of the plates (see Figure 7.6). At this location normal weld condition were simulated introducing high stresses in the material. Similar to the initial material removal, the weld is removed from the end of the initial weld until the midsection. Again the cap and half depth of the weld is removed with a total width of 6.4 mm. Distortion results can be found in Figure 7.7. A clear similarly shaped distortion pattern can be seen, resembling the distortion measured after the experiment. The difference between experiment and model results is a maximum of 0.25 mm, an approximate 63% difference compared to experimental results.

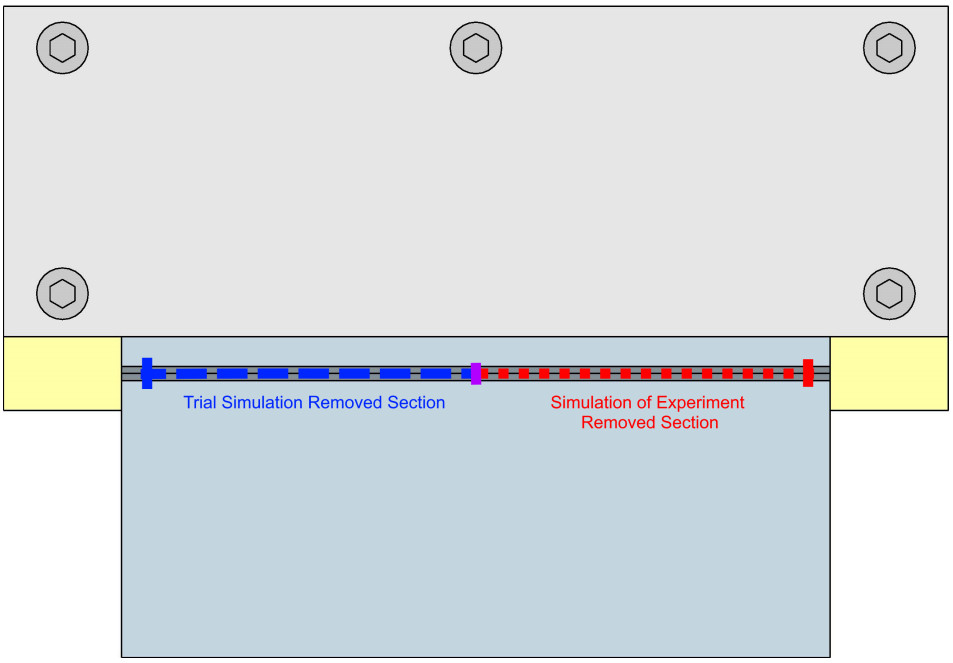

Figure 7.6: Removed section of the experiment and the removed section of the trial simulation.

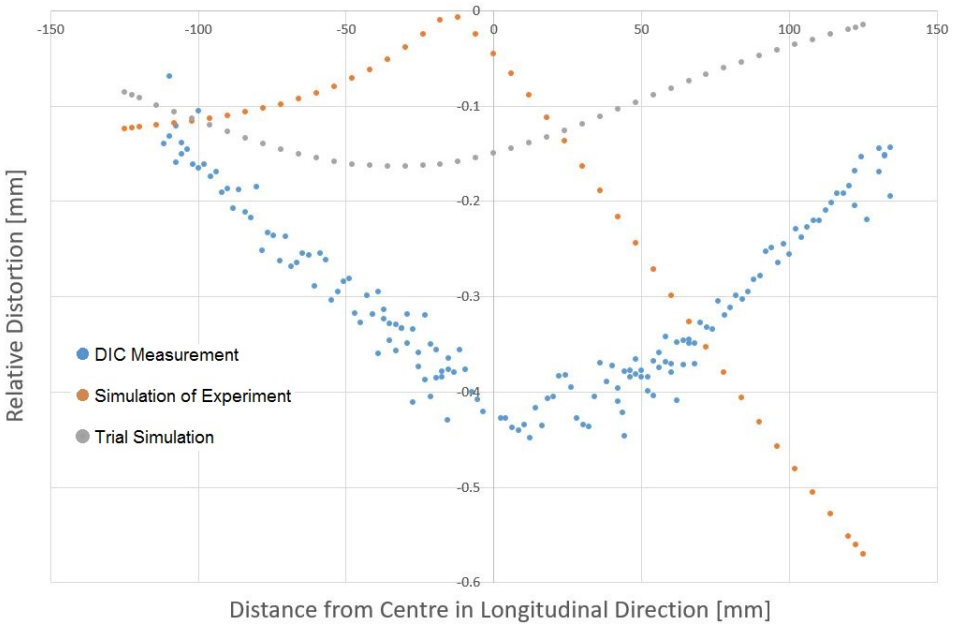

Figure 7.7: Experimental (blue, convex), simulation results of the experiment (orange, concave) and simulation of a example trial simulation, removing the (normally) welded section in the simulation (gray, convex). The trial simulation shows a similar pattern, compared to the experimental results. Both follow the negative shape of the during welding formed buckling shape.

Stress Distribution Change

In Figure 7.10 and Figure 7.9 show stresses over a longitudinal line at the bottom of the plate near the weld, and a transverse line at the middle location of the removed section, at the bottom of the plate. In Figure 7.9 stresses are shown on a transverse line just after the start point of the weld. Noticeable in the longitudinal stresses in the figure near the weld show a clear shift of stresses towards a more compressive stress state.

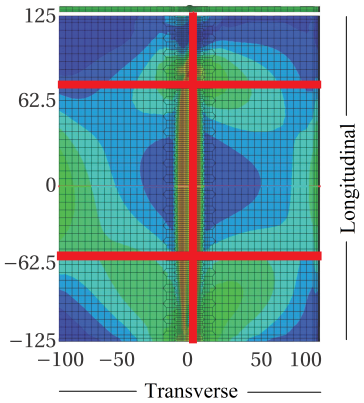

Figure 7.8: The three locations of the shown stress distribution. One longitudinal line, two transverse lines at about 62.5 mm for the experimental removal simulation and approximately −62.5 mm for the example model simulation.

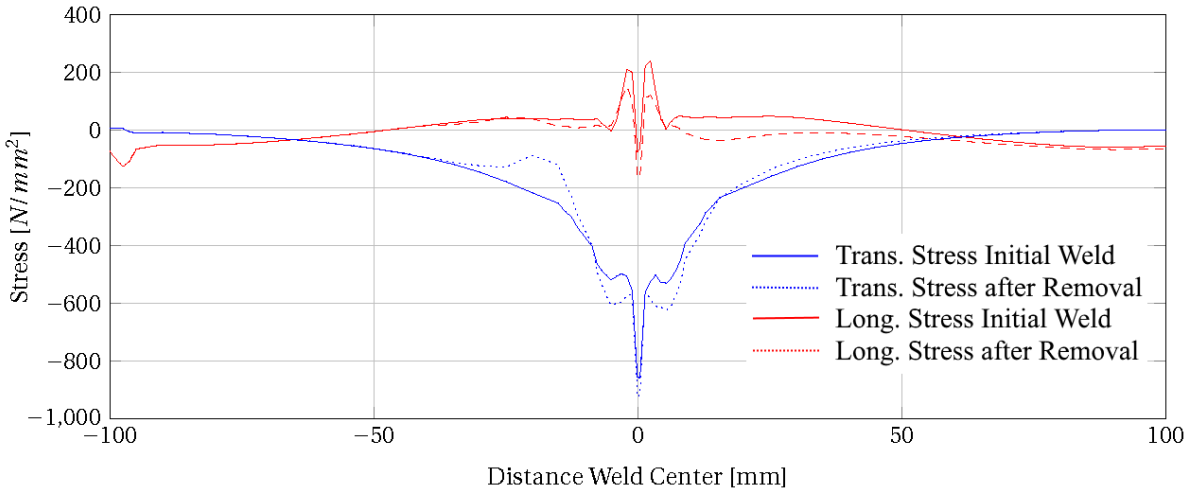

Figure 7.9: Transverse distribution of stresses near the start point of the weld, approximately at the midsection of the removed material section.

Figure 7.11 presents the transverse distribution of stresses at the location of the midsection of removed part. The local effect of the removal on the stress distribution does not seem to have a significant influence, especially when compare with Figure 7.9. This may be because of the more plastic regions surrounding the material at the weld due to the welding process, compared to the location close to the start point of Figure 7.9.

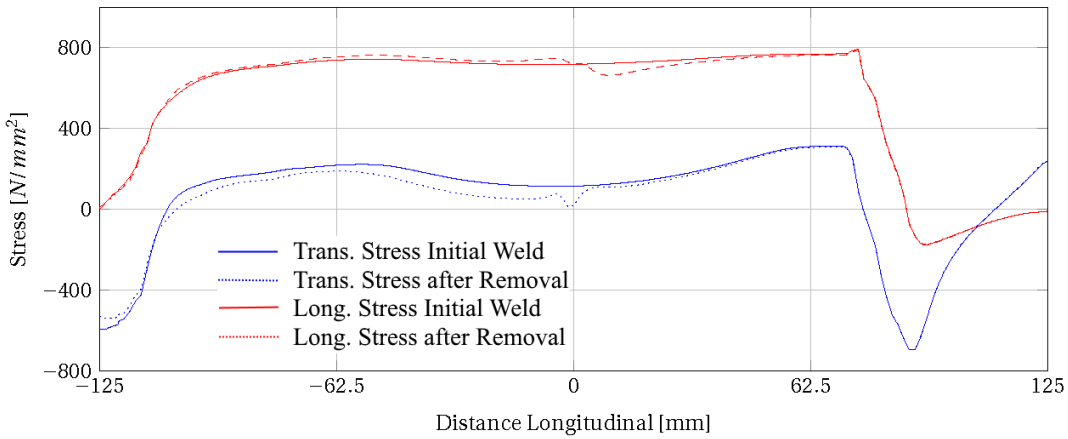

Figure 7.10: Longitudinal distribution of stresses near the weld, at the bottom of the plate.

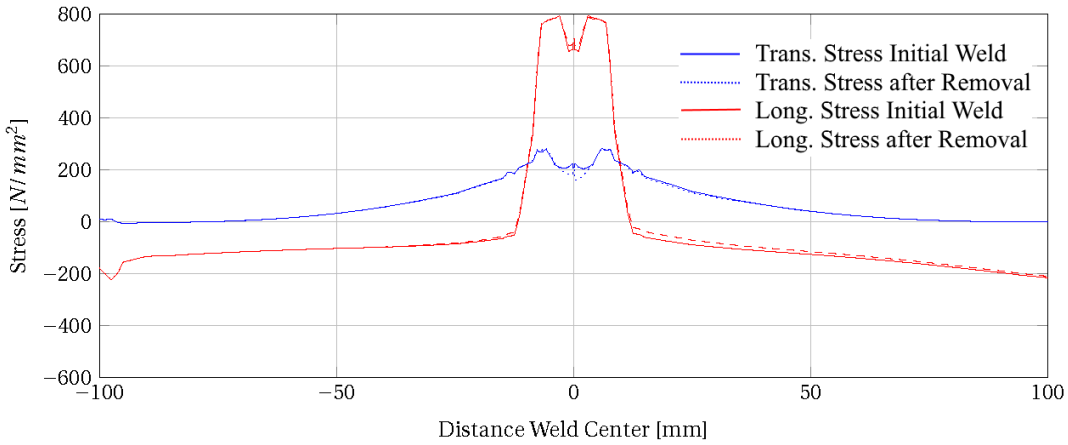

Figure 7.11: Transverse distribution of stresses at the removed part of the example model, approximately at 2/3 of the weld length.

7.4. Chapter Summary

In this Chapter the experimental approach and results of the material removal process of the weld are presented. A section of the weld is removed using a milling process, which is a relative slow and gradual removal process. Therefore, the heat effects due to the removal process are assumed to be negligible Distortion measurement after removal by DIC are presented, showing a decrease of the total buckling curve of the distorted plates.

A simulation approach is presented, using the material change function of the Abaqus software. Simulation results of the material removal does not show comparable results with the distortion data retrieved from the experiment. An additional simulation is performed to verify the assumption of the zero stress state in the first faulty weld section, made earlier in the modelling of the initial weld. As a result it is shown that this assumption was of significant important to the simulation result, causing simulation results which were not comparable with experiment results. And lastly, stress distributions before and after the removal process are shown, to verify that indeed a changes of residual stress occurs once the material is removed.

8

Repair Weld Experiment

In Chapter 7 the experiment and simulation of the partial removal of the weld, which resembles the crack removal of a repair procedure, is discussed. The last step in the repair procedure experiment is execution of the weld repair. Experiment results are discussed in this chapter.

8.1. Welding Specification

The repair weld is performed on the removed section of the weld (see Section 7.2). The removed groove is of a rectangular shape, with a depth of 2 mm and a total width of 6.4 mm (see Figure 8.1).

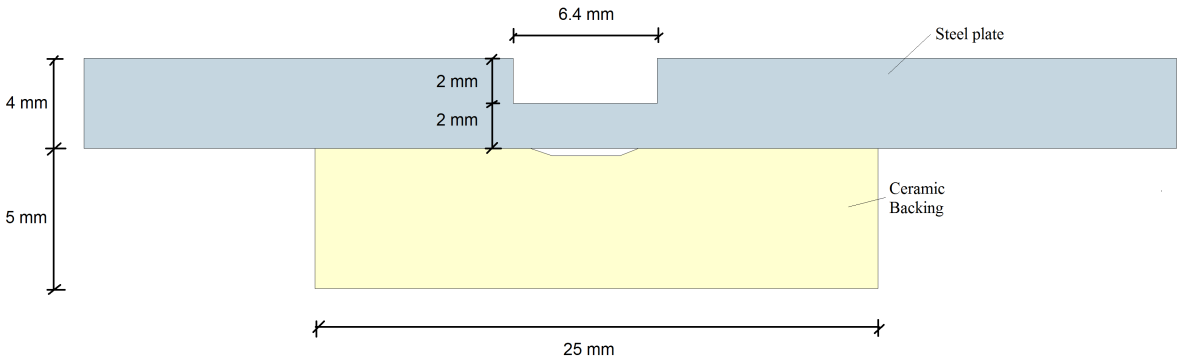

Figure 8.1: The geometry of the repair weld.

Other specifications of the weld are similar as the initial weld (see Section 4.3). Table 8.1 presents an overview of the used welding parameters.

8.1.1. Constrainment

As discussed in Section 4.3.1, the clamping set-up was designed to keep the specimen clamped during the whole repair weld procedure. Thus, the clamping set-up of the specimen is not altered.

8.2. Welding Power Measurement

The welding power was automatically determined by the welding power source. The input parameter for the GMAW power source were the the wire diameter and wire feed speed.

Table 8.1: Overview of the welding specification of the repair weld

Steel Grade	S700MC	
Workpiece Dimension	250 × 100 × 4	mm^3
Welding Process	GMAW	
Weld Transfer Mode	Short-Circuit	
Weld Type	Repair Weld	
Weld Shape	Rectangular-shape	
Contact Tube to Workpiece Distance	15	mm
Weld Gun Angle	10	°
Shielding Cup to Workpiece Distance	7.5	mm
Wire	Böhler UNION NiMoCr	
Wire Classification	ER100S-G	
Wire Diameter	1.2	mm
Wire Feed Speed	5.7	m/min
Shielding Gas	85% Ar - 15% CO2	
Shielding Gas Flow Rate	15	L/min

The welding voltage and current measurements were recorded by a Yokogawa DL750 oscilloscope at a sampling rate of 200 Hz

8.2.1. Welding Power: Voltage and Current

Voltage and current returned from the welding power source is 20.0 V and 233 A, respectively. In the measurement results a big scatter is observed, typical for Short-Circuit welding since during weld metal transport the arc short-circuits, causing a drop in voltage (see Figure 8.2). A zoom of the measurement confirms the Short-Circuit welding [41]. A typical short-, reignition-, arcing- and extinction-period is observed (see Figure 8.3).

8.2.2. Energy Intervals

The welding energy input of the measured voltage and current is compared with the energy input of the voltage and current displayed by the welding power source. 4 successive intervals of 5 second are compared to investigate the differences (see Table 8.2). An average difference of −4.6% was found.

Table 8.2: Overview of welding energy input of 4 successive, 5 second intervals.

Interval [sec]	Total Energy - Measurement [Joule]	Total Energy - Power Source [Joule]	Difference [%]
1.1 - 5.1	22483	23300	~ −3.5
5.1 - 10.1	22220	23300	~ −4.6
10.1 - 15.1	21961	23300	~ −5.7
15.1 - 20.1	22254	23300	~ −4.5
		Average	~ −4.6

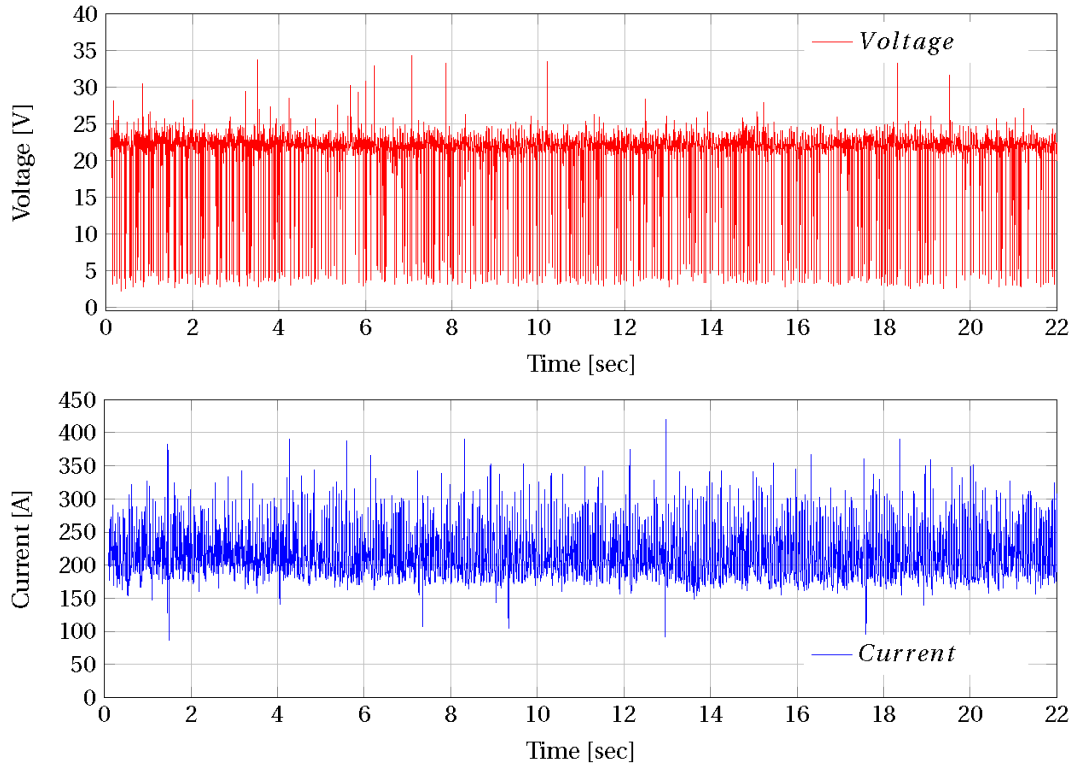

Figure 8.2: Voltage and current measurements during the repair welding process. Measurement was performed at a sample rate of 200 Hz.

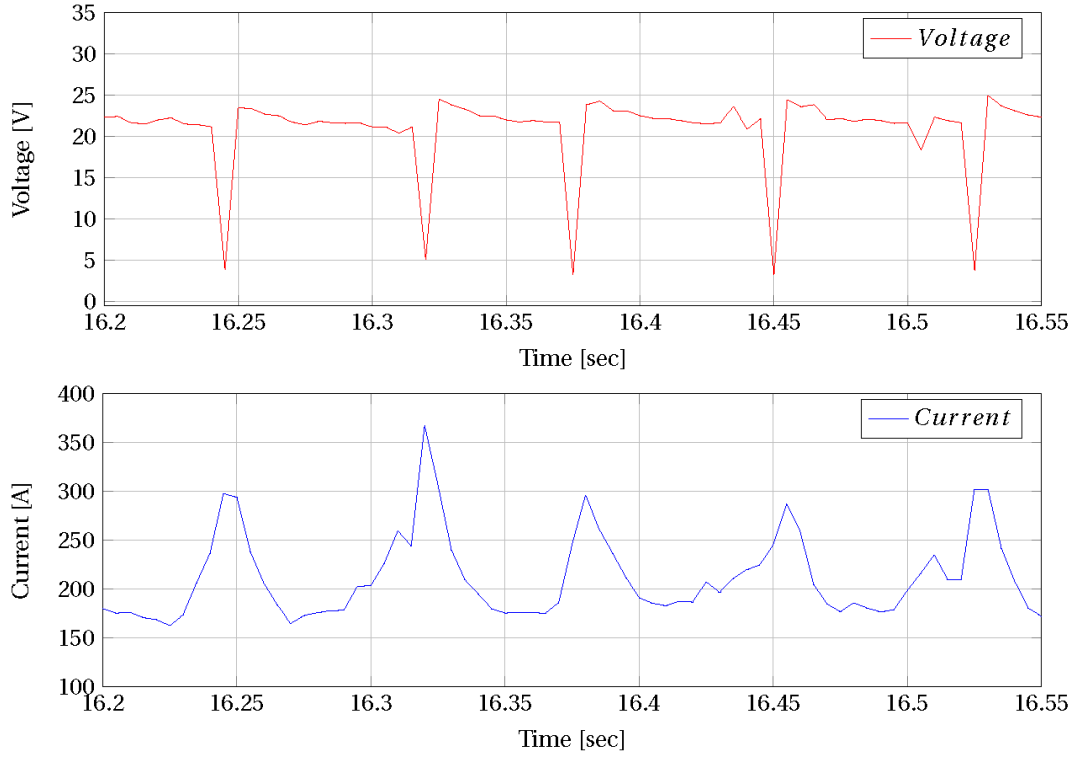

Figure 8.3: Zoom of voltage and current measurements during the repair welding process.

8.3. Temperature Measurement

Six K-type thermocouples were placed on the bottom surface of the plate (see Figure 8.4). These measurement locations were chosen to retrieve data in the transverse direction but also longitudinal direction of the weld. The thermal measurement were recorded by a thermocouple modules in a Yokogawa DL716 oscilloscope at a data sample rate of 2 Hz.

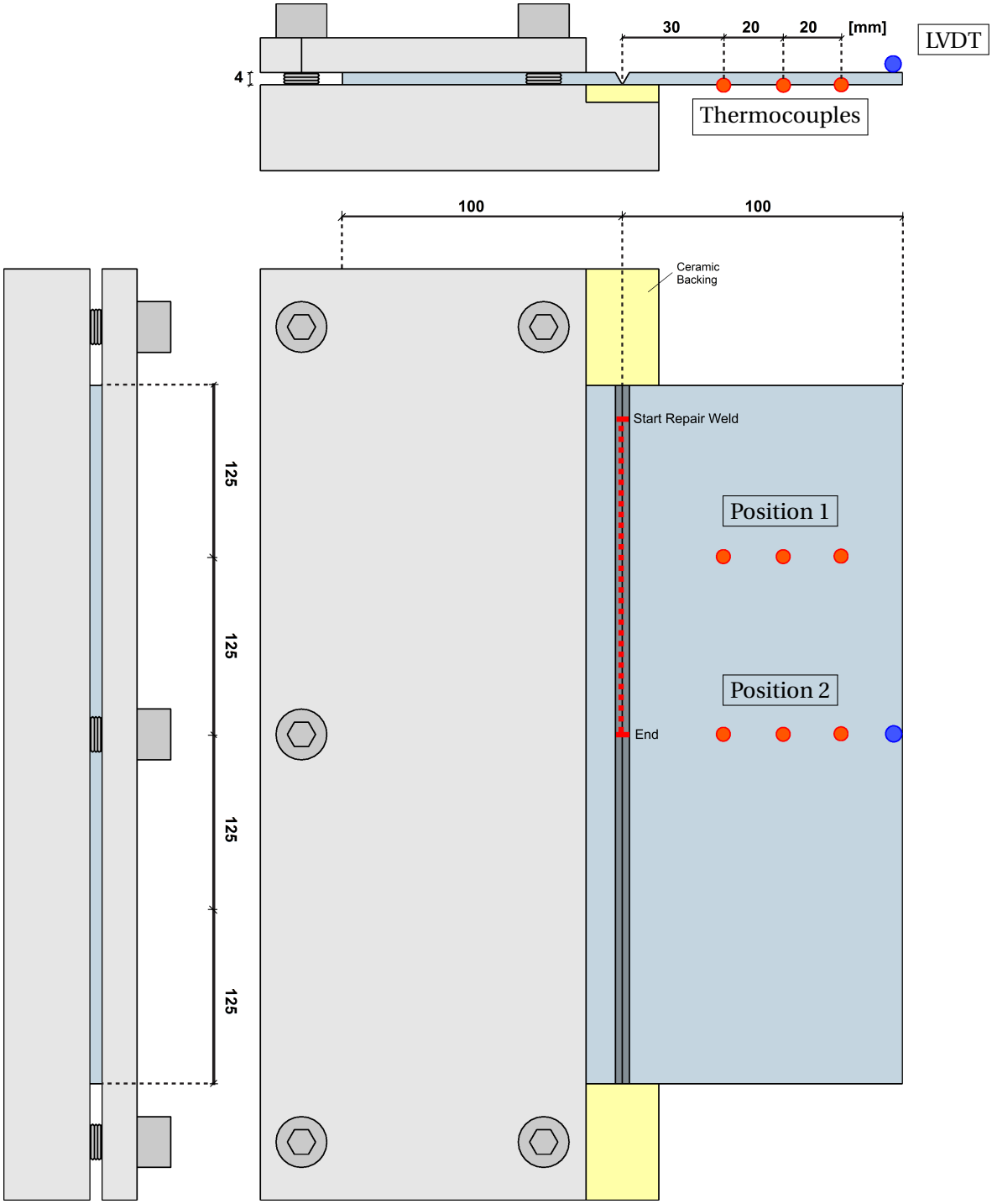

Figure 8.4: Location of thermocouples and LVDT during the weld repair experiment.

8.3.1. Thermal Results

Transient temperature measurement results are presented in Figure 8.5 and Figure 8.6. The first figure shows the measurement of the thermocouple at the mid section of the repair weld in longitudinal direction. The second figure presents the temperature measurement near the end of the repair weld.

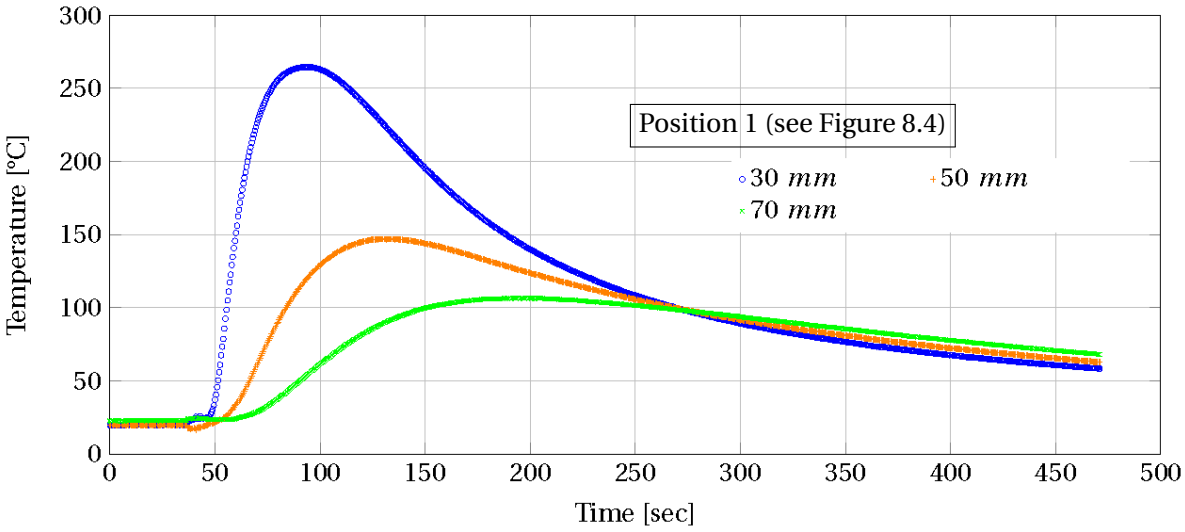

Figure 8.5: Temperature measurement at half length of the weld repair (see Figure 8.4), at quarter length of the plate

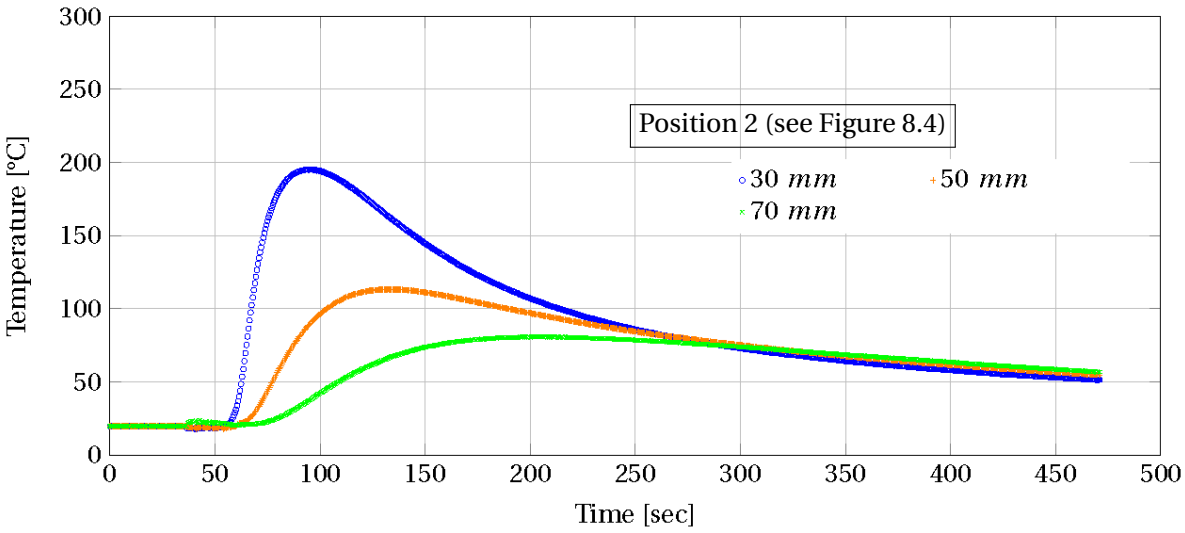

Figure 8.6: Temperature measurement at full length of the weld repair (see Figure 8.4), at half length of the plate.

8.4. Distortion Measurement

8.4.1. LVDT

An LVDT measurement is performed during the repair weld experiment. The measurements were recorded by a Yokogawa DL716 oscilloscope at a data sample rate of 2 Hz. Results of the transient distortion caused by the repair weld are found in Figure 8.7. As was discussed in Section 4.4.3, again the LVDT measurement experience a lot of noise.

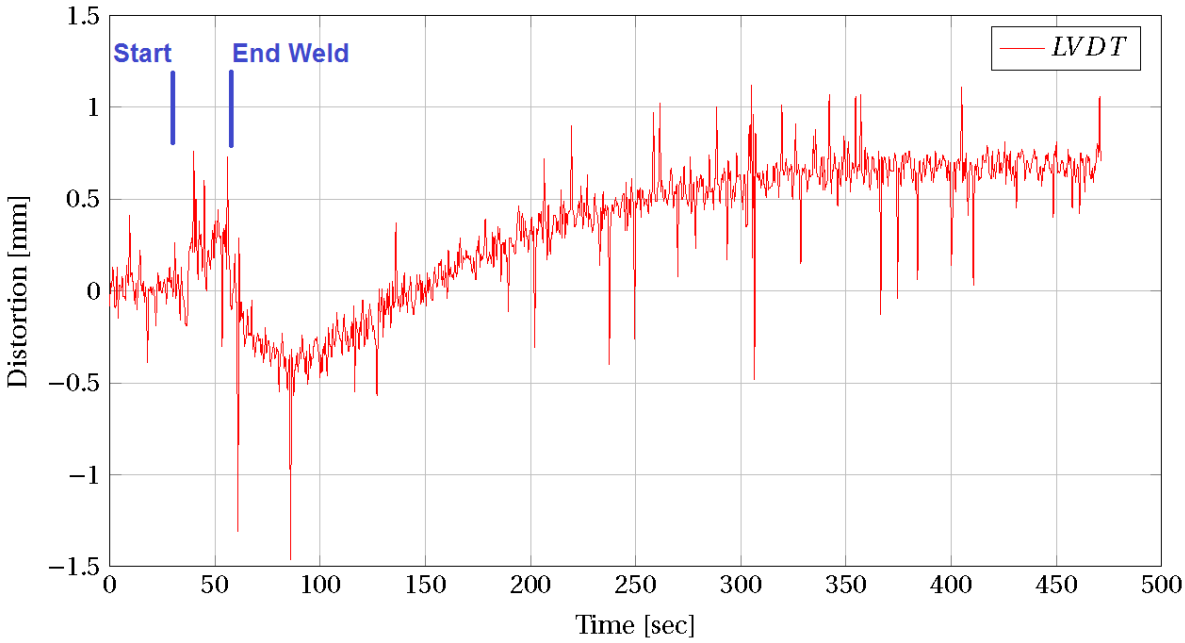

Figure 8.7: LVDT measurement during the repair weld experiment.

As can be seen in the figure, once the weld starts, distortion is increasing. This effect was also observed in the initial weld LVDT measurement (see Figure 6.9). After the weld has been complete, a clear drop can found. It is thought that this distortion behaviour is caused by the re-distribution of residual stress already in the plate due to the initial weld, accompanied by residual stresses due to the repair weld. A final distortion of an approximate 0.67 mm was measured after cooling.

8.4.2. DIC Measurement

DIC measurement of the plate after repair welding are found in Figure 8.8. Results show that distortion results occur relative locally, compared to the initial weld DIC results (see Figure 6.19). This is most likely due to the increased stiffness of the plate after application of the initial weld, and the location and geometry of the welded groove (see Figure 8.1).

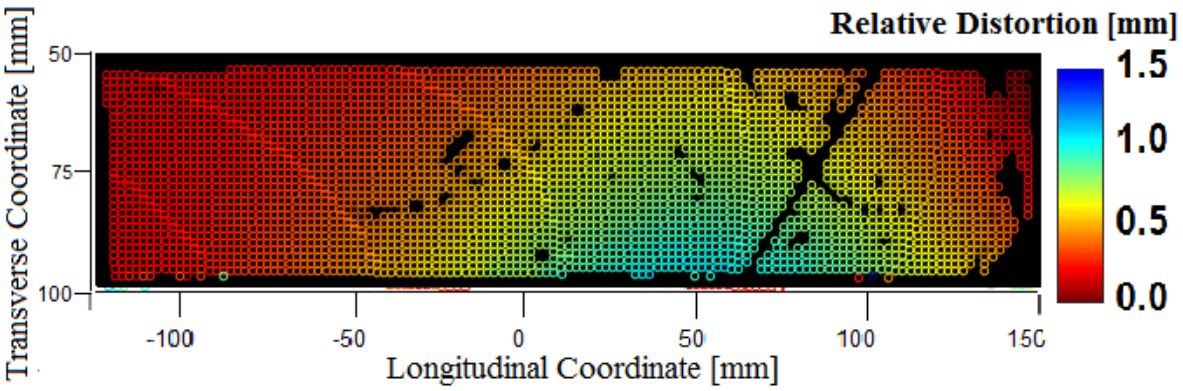

Figure 8.8: DIC measurement after the repair weld. Distortion shown is the distortion relative to the distortion after weld removal.

DIC distortion measurement at the location of the LVDT (see Figure 8.4) resu
0.685 mm, which is in good agreement with the final LVDT distortion results
relative distortions measured by DIC at the outer-edge location of the plate.

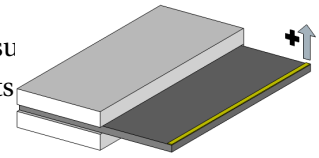

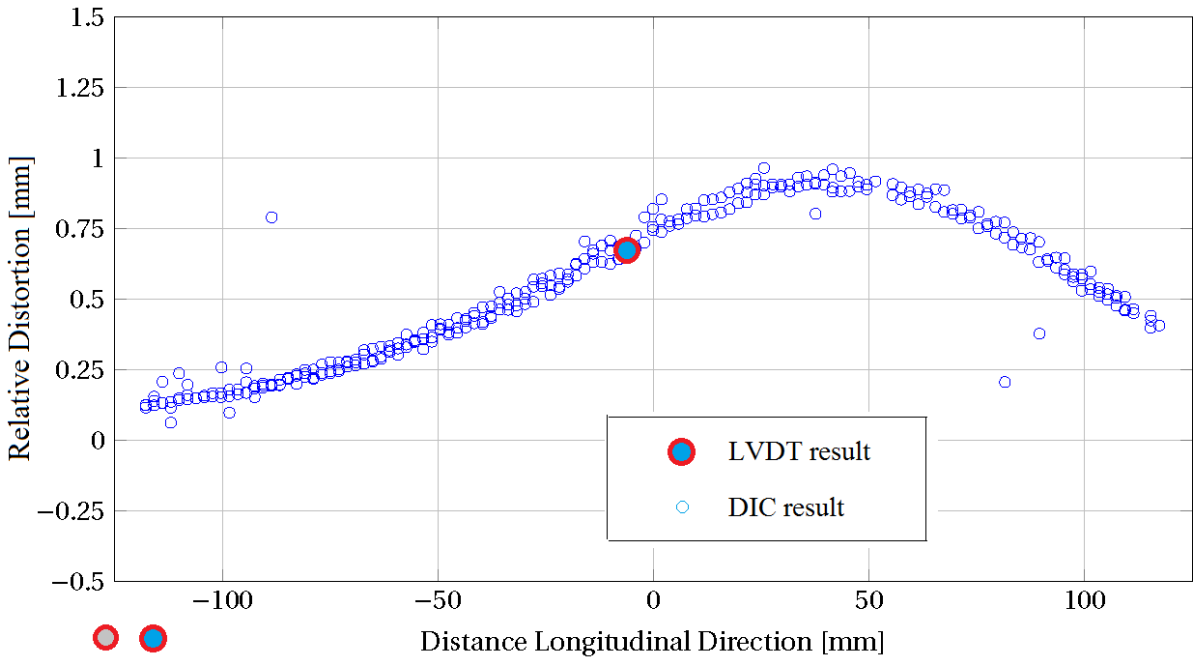

Figure 8.9: DIC distortion results at the edge of the plate, in the longitudinal direction where the weld was present at the right half of this graph.

9

Conclusion and Recommendations

A finite element model is specifically created to predict distortions of a welded connection during an initial welding and a weld reparation. Comparison of experimental results of temperature distribution and distortion to the results obtained from FEM (Finite Element Modelling) model leads to following conclusions:

At the initial welding stage: the FE (Finite Element) model is able to predict temperature development and weld distortions quite accurately. Temperature point measurement results of 10 mm from the weld centre show a maximum scattering in prediction and the experimental results of the plate temperature is 30°C at peak temperature.

At 100 mm from the weld centre, maximum scattering in prediction and the experimental results of the plate deformation after welding is 0.4 mm, which is a deviation of 10% of the total distortion found in experiment.

At the weld defect removal stage: the FE model shows significant discrepancies when comparing the predicted distortion results to experimentally obtained results. At a line 100 mm from the weld the maximum scattering in prediction and the experimental results of the plate deformation is 0.35 mm, which is a deviation of approximately 100% of the total distortion found in experiment.

However, results obtained from the FE model show the same trend of deformation when removal of a normal welded section was performed. At a distance of 100 mm from the weld centre the maximum scattering in prediction and the experimental results of the plate deformation is 0.25 mm, which is a deviation of approximately 63% of the total distortion found in experiment.

Based on the comparison of FE results and performed experiments at the welding stage, a “calibrated” FE model is established to model a weld repair process. The model is calibrated by comparing the distortion during the welding which is measured in experiments to fit the experimentally obtained displacement.

9.1. Thermal Analysis

A thermal analysis due to welding is performed by FEA (Finite Element Analysis) which is used as input for a thermo-mechanical analysis of the plate distortion. The thermal analysis is performed

using a Goldak heat distribution model which is applied and calibrated on a 2D FE model, before being applied on a 3D thermal model. The 2D model is first investigated because it requires less computation time, it is at least 25 times more efficient (see Table 5.1). Results of the 2D model and the 3D model show good agreement, when subjected to the same heat source, with the biggest scattering of 150°C at 3 mm from the weld centre. A mesh sensitivity analysis is performed in the weld vicinity to optimize computation time of the 3D model. The mesh size parallel to the weld is varied and showed that results are dependent of mesh density, see Figure 6.1. The variation of the temperature is relatively constant at dense mesh of about 600 elements per meter.

Results obtained in 3D model show a good agreement with the experimental results. The biggest scattering is 30°C obtained at 10 mm from the weld centre (see Figure 6.8).

Only thermal distribution perpendicular to the weld is possible to obtain from the 2D model. Results of the 3D analysis shows that at 3, 5, 10, 30, 50 and 70 mm distance perpendicular to the weld, the peak values becomes constant in the midsection of the weld, see Figure 6.25. This means that the results of 2D analysis in this model correctly predict the temperature peak values in the region 30 mm from the ends of the weld.

9.2. Thermo-mechanical Analysis

Clamps are used to prevent plate deformation during the welding. However, the distortion is observed, in the range of 0.1 mm, after the experiments. This is a clear indication that the mechanical boundary conditions of the FE model should have a certain displacement stiffness. However, in this model mechanical boundary conditions are modelled by fixed boundary conditions. From comparison of prediction and experimentally obtained distortion results, a sufficient boundary condition with matching distortion results was found (see Figures 6.14 and 6.16).

A transient out-of-plane deformation measured by LVDT and prediction during the initial welding shows the biggest scattering of 0.7 mm, which is a deviation of approximately 60% of the total distortion found in experiment (see Figure 6.11) at the first 20 seconds of the welding process. After cooling of the weld, the difference in model and experiment results if reduced to 0.4 mm, which is approximately 10% of the found experimental distortion results.

Furthermore, a close agreement between surface distortion measurement by DIC (Digital Image Correlation) and FE results are shown in Figures 6.18 and 6.19. Calliper measurements of the distortion of the plate is maximum 30% bigger than FE results, but show an overall good agreement, see Figure 6.20.

An element activation was required to model the liquid-to-solid phase transformation of the molten weld material in the thermo-mechanical analysis, see Section 5.3.1. This activation starts at a 1000°C, from which a thermal shrinkage is initiated. An influence of this start temperature on the distortion of the plate is investigated to determine whether it is a potential important factor to consider in the model. Figure 6.21 has shown that a temperature of 700 degrees or higher, this parameter has no influence. The fact that the start temperature is not important factor could be explained by the assumed perfect plastic model used in FEA.

Furthermore, the elements which represent the weld pool only experience shrinkage during a heat cycle to account for strain reset during liquefaction from solid state of the material, see Section 5.3.7. This requires a subroutine during the heat analysis which records a database of the weld pool element. This database is used in subroutines of the thermo-mechanical analysis to assign this cooling only behaviour.

Combining the results of the thermal and thermo-mechanical analyses indicates that the FEM model is able to determine temperatures and weld distortions quite accurately.

9.3. Recommendations

Based on the performed work in this thesis, the following recommendations are made for future works:

More variation of experimental set-up is necessary to improve validation of the finite element model. The clamping set-up needs improvement to avoid modelling of stiffness in boundary conditions.

Residual stress measurement is needed to investigate the correlation between residual stress and distortion. Results of the thesis show that for a defect or faulty weld section, the measurement of the residual stresses is of great importance.

The relation between the 2D analysis and 3D analysis should be further examined for the heat transfer analysis. A good agreement of 2D and 3D thermal results is found, however in order to draw a general conclusion, an investigation of more variation in weld configuration is needed.

Temperature-dependent material characteristics should be experimentally established to reduce uncertainties of the FEA.

FEA of the full weld repair procedure proved to be beyond the scope of this thesis, since FE work was more time consuming than initially anticipated.

Bibliography

[1] M.M. Pruijssers. *Use of S460 in the Dutch building industry.* Master thesis, Delft University of Technology, 2015.

[2] E. Gogou. *Use of High Strength Steel Grades for Economical Bridge Design.* Master thesis, Delft University of Technology, 2012.

[3] R.J.M. Pijpers. *Fatigue strength of welded connections made of very high strength cast and rolled steels.* Phd. thesis, Delft University of Technology, 2011.

[4] R.J.M. Pijpers, M.H. Kolstein, A. Romeijn, and F.S.K. Bijlaard. Fatigue experiments on very high strength steel base material and transverse butt welds. *Advanced Steel Construction*, 5 (1):14 – 32, 2009.

[5] J.D.M. Costa, J.A.M. Ferreira, and L.P.M. Abrea. Fatigue behaviour of butt welded joints in a high strength steel. *Procedia Engineering*, 2:697 – 705, 2010.

[6] S.J. Maddox. *Fatigue Behaviour of Welded Joints.* Advances in Fatigue Science and Technolgy. Kluwer Academic Publishers, 1989.

[7] G. Totten, M. Howes, and T. Inoue, editors. *Handbook of Residual Stress and Deformation of Steel.* ASM International, Materials Park, USA, 2002.

[8] H. Gao. *Residual Stress Development due to High-Frequency Post Weld Impact Treatments for High-Strength Steels.* PhD thesis, Delft University of Technology, 2014.

[9] C. Ohms. *Residual Stresses in Thick Bi-metallic Fusion Welds: a Neutron Diffraction Study.* PhD thesis, Delft University of Technology, 2013.

[10] J.W.B. Stark and R. Abspoel. *Steel Structures 3: Cold Formed Sections.* TU Delft, 2010.

[11] A. Trudel, M. Brochu, and M. Lévesque. Residual stress effects on the propagation of fatigue cracks in the weld of a ca6nm stainless steel, 2013.

[12] D. Deng and H. Murakawa. Prediction of welding distortion and residual stress in a thin plate butt-welded joint. *Computational Materials Science*, 43:353 – 365, 2008.

[13] Z. Feng, editor. *Processes and mechanisms of welding residual stress and distortion.* Woodhead Publishing Limited and Maney Publishing Limited, Boca Raton, USA, 2005.

[14] A. Suwardono. Transducer, 2014. URL `agussuwardono.blogspot.nl/2014/05/transducer.html`. Accessed: 15th of March, 2016.

[15] Direct Industry. Linear displacement sensor / lvdt / digital, 2017. URL `http://www.directindustry.com/prod/solartron-metrology/product-4818-632058.html`. Accessed: 20th of January, 2017.

[16] LMI Technologies Inc. Gocator 1300 displacement sensor, 2016. URL http://downloads.lmi3d.com/system/files/Gocator/documents/Gocator%201300%20Series/DATASHEET_Gocator_1300_WEB_EN.pdf.

[17] Jenoptik. Laser rangefinders for mobile and stationary systems, 2016. URL http://www.jenoptic.com/products/defense-and-security/laser-rangefinders. Accessed: 26th of February, 2016.

[18] S.H.J. Van Es. *Effect of TIG-dressing on fatigue strength and weld toe geometry of butt welded connections in high strength steel.* Master thesis, Delft University of Technology, 2012.

[19] A.M.A. Pazooki. *Distortion Control during Welding.* PhD thesis, Delft University of Technology, 2014.

[20] Limess Messtechnik and Software GmbH. Dic| digital image correlation. URL http://www.limess.com/download/LIMESS_Leaflet_DIC.pdf. Accessed: 24th of February, 2016.

[21] G. Zhu, Y. Tian and H. Lu, R. Zhang. A review of optical ndt technologies. *Sensors*, 11(8):7773 – 7798, 2011.

[22] Correlated Solutions. Principle of digital image correlation, 2016. URL www.correlatedsolutions.com/digital-image-correlation/. Accessed: 14th of March, 2016.

[23] J.L.W. Carter, M.D. Uchic, and M.J. Mills. Impact of speckle pattern parameters on dic strain resolution calculated from in-situ sem experiments. *Fracture, Fatigue, and Damage Evolution*, 5:119 – 126, 2014.

[24] G.S. Schajer, editor. *Practical Residual Stress Measurement Methods.* John Wiley and Sons Ltd., West Sussex, UK, 2013.

[25] N.S. Rossini, M. Dassisti, K.Y. Benyounis, and A.G. Olabi. Methods of measuring residual stresses in components. *Materials and Design*, 35:572 – 588, 2012.

[26] G.S. Schajer. Relaxation methods for measuring residual stresses: Techniques and opportunities. *Experimental Mechanics*, 50(8):1117 – 1127, 2010.

[27] P. Sarga and F. Menda. Comparison of ring-core method and hole-drilling method used for determining residual stresses. *American Journal of Mechanical Engineering*, 1(7):335 – 338, 2013.

[28] R. Eduardo, M. Cristina, C.J. Luis, G. Julio, and S.J. Manuel. Validation of residual stresses of finite element simulation of multi pass butt-welded plates using the contour method. *Materials Science Forum*, 681:67 – 72, 2011.

[29] Inc. CAMET Research. Quantification of retained austenite. URL camet-lab.com/retained_austenite.html. Accessed: 17th of March, 2016.

[30] A.C. Reardon. *Metallurgy for the Non-Metallurgist.* ASM International, Ohio (USA), 2011.

[31] StackOverflow and NictraSavios. How to code an array of fcc, bcc and hcp lattices in c++, 2017. URL http://stackoverflow.com/questions/20600062/how-to-code-an-array-of-fcc-bcc-and-hcp-lattices-in-c. Accessed: 22th of January, 2017.

[32] N. Bailey. *Weldability of ferritic steels*. Abington Publishing, Cambridge, Englang, 1994. Part of iron-carbon phase diagram.

[33] R.A. Gonzaga, P. Martínez Landa, A. Perez, and P. Villanueva. Mechanical properties dependency of the pearlite content of ductile irons. *Journal of Achievements in Materials and Manufacturing Engineering*, 33(2):150 – 158, 2009.

[34] G. Krauss. Martensite in steel: strength and structure. *Materials Science and Engineering: A*, 273:40 – 57, 1999.

[35] W. Pors, A.M. Gresnigt, and J.C. van Wortel. Constructiestaalsoorten met hoge sterkte. *VM 125*, 2008.

[36] E. Harati, L-E. Svensson, L. Karlsson, and M. Widmark. Effect of high frequency mechanical impact treatment on fatigue strength of welded 1300 mpa yield strength steel. *International Journal of Fatigue*, 92(1):96 – 106, 2016.

[37] O. Hechler, G. Axmann, and B. Donnay. *The right choice of steel - according to the Eurocode -*, pages 22 – 43. Springer, 2009.

[38] N. Hansen. Hall-petch relation and boundary strengthening. *Scripta Materialia*, 51:801 – 806, 2004.

[39] Engineering Archives. Stress-strain diagram, 2008. URL http://www.engineeringarchives.com/les_mom_stressstraindiagram.html. Accessed: 23th of January, 2017.

[40] L. Jeffus. *Welding: Principles and Applications - Seventh Edition*. Delmar, Cengage Learning, Clifton Park, USA, 2012.

[41] G. den Ouden and M.J.M. Hermans. *Welding Technology*. VSSD, Delft, 2009.

[42] J.T. Black and A. Ronald. *DeGarmo's materials and processes in manufacturing*. John Wiley and Sons, 2011.

[43] E.M. Van der Aa. *Local Cooling during Welding: Prediction and Control of Residual Stresses and Buckling Distortion*. PhD thesis, Delft University of Technology, 2007.

[44] J. Wang, S. Rashed, and H. Murakawa. Mechanism investigation of welding induced buckling using inherent deformation method. *Thin-Walled Structures*, 80:109 – 119, 2014.

[45] A. Pilipenko. *Computer simulation of residual stress and distortion of thick plates in multi-electrode submerged arc welding. Their mitigation techniques*. PhD thesis, Norwegian University of Science and Technology (NTNU), 2001.

[46] M. Pirinen. *The effects of welding heat input on the usability of high strength steels in welded structures*. PhD thesis, Lappeenranta University of Technology, 2013.

[47] European Committee for Standardization. Nen-en 10149-2: Hot rolled flat products made of high yield strength steels for cold forming - part 2: Technical delivery conditions for thermomechanically rolled steels, 2013.

[48] J. Górka. Effect of heat treatment on the properties of thermomechanically treated steel. *Machines, Technologies, Materials.*, 2013(12):24 – 27, 2013.

[49] ArcelorMittal. Freightrail: On track for savings. *update - Client Magazine*, (November), 2011.

[50] L. Bracke, N. De Wispelaere, H. Ahmed, and O.E. Gungor. S700mc/grade 100 in heavy gauges: industrialisation at arcelormittal europe. *Revue de Métallurgie*, (108):323 – 330, 2011.

[51] J. Górka. Weldability of thermomechanically treated steels having a high yield point. *Archives of Metallurgy and Materials*, 60(1):469 – 475, 2015.

[52] The Welding Institute (TWI). Is there a restriction on the heat input that can be used for the welding of tmcp (thermo-mechanically controlled processed) steels - if so, why? URL `http://www.twi-global.com/technical-knowledge/faqs/material-faqs/faq-is-there-a-restriction-on-the-heat-input-that-can-be-used\discretionary{-}{}{}for-the-welding-of-tmcp-thermo-mechanically-controlle\discretionary{-}{}{}processed-s/`. Accessed: 15th of February, 2016.

[53] N. Saunders, U.K.Z. Guo, X. Li, A.P. Miodownik, and J. Ph. Schillé. Using jmatpro to model materials properties and behavior. *The Journal of The Minerals*, 55(12):60 – 65, 2003.

[54] J.J. Chyle and M.W. Zimmermann. Ceramic welding back-up strip and method of applying the same, 1959. United States Patent and Trademark Office; US Patent 2 916 001 A.

[55] Böhler Welding Austria GmbH. *Filler Metals Bestseller for Joining Applications.* 2016.

[56] Pico Technologies. URL `https://www.picotech.com/accessories/current-probes-clamps/600-a-current-probe-4mm`. Accessed: 8th of October, 2016.

[57] W. Cheng. *In-plane shrinkage strains and their effects on welding distortion in thin-wall structures.* PhD thesis, The Ohio State University, 2005.

[58] Z. Cao, Z. Yang, and L. Chen. Three-dimensional simulation of transient gma weld pool with free surface. *Welding Journal*, 83:169–S – 176–S, 2004.

[59] Z. Zhang and C. Wu. Effect of fluid flow in the weld pool on the numerical simulation accuracy of the thermal field in hybrid welding. *Journal of Manufacturing Processes*, 20:215 – 223, 2015.

[60] M. Rappaz, S.A. David, J.M. Vitek, and L.A. Boatner. Analysis of solidification microstructures in fe-ni-cr single-crystal welds. *Metallurgical Transactions A*, 21(6):1767 – 1782, 1990.

[61] P. Asadi, M.K.B. Givi, and M. Akbari. Microstructural simulation of friction stir welding using a cellular automaton method: a microstructure prediction of az91 magnesium alloy. *International Journal of Mechanical and Materials Engineering*, 10(20):1 – 14, 2015.

[62] V. Pavlyk and U. Dilthey. Simulation of weld solidification microstructure and its coupling to the macroscopic heat and fluid flow modelling. *Modelling and Simulation in Materials Science and Engineering*, 12(1):S33 – S45, 2004.

[63] Dassault Systemes. Abaqus 6.14 online documentation. 2014. URL `http://abaqus.software.polimi.it/v6.14/index.html`.

[64] Z.S. Spakovszky, E.M. Greitzer, and I.A. Waitz. 16. unified: Thermodynamics and propulsion, 2002. URL `http://web.mit.edu/16.unified/www/FALL/thermodynamics/notes/html`.

[65] R.A. Serway and J.W. Jewett. *Physics for Scientists and Engineers with Modern Physics*. Brooks/Cole Publishing Company, Boston, USA, 9th edition, 2014.

[66] J. Goldak, A. Chakravarti, and M. Bibby. A new finite element model for welding heat sources. *Metallurgical Transactions B*, 15(2):229 – 305, 1984.

[67] H. Pasternak, B. Launert, and T. Krausche. Welding of girders with thick plates - fabrication, measurement and simulation. *Journal of Constructional Steel Research*, 115:407 – 416, 2015.

[68] H. Long, D. Gery, A. Carlier, and P.G. Maropoulos. Prediction of welding distortion in butt joint of thin plates. *Materials and Design*, 30:4126 – 4135, 2009.

[69] M.R.A. Rikken. *Modelling and verification of residual stresses due to welding in a T joint*. Minor thesis, Delft University of Technology, 2015.

[70] M. Shubert, M. Pandheeradi, F. Arnold, and C. Habura. An abaqus extension for welding simulations, 2010.

[71] C. Parmar, C.M. Gill, P.R. Hurrell, and B.M.E. Pellereau. Simulation of a multi-pass groove weld and clad plate using abaqus 2d weld gui and comparison with measurements, 2014.

[72] L-E. Lindgren, H. Runnemalm, and M.O. Näsström. Simulation of multipass welding of a thick plate. *International Journal for Numerical Methods in Engineering*, 44:1301 – 1316, 1999.

[73] A.S. Elmesalamy, H. Abdolvand, J.N. Walsh, J.A. Francis, W. Suder, S. Williams, and L. Li. Measurement and modelling of the residual stresses in autogenous and narrow gap laser welded aisi grade 316l stainless steel plates. *International Journal of Pressure Vessels and Piping*, 147: 64 – 78, 2016.

[74] P. Mollicone, D. Camilleri, and T.G.F. Gray. Procedural influences on non-linear distortions in welded thin-plate fabrication. *Thin-Walled Structures*, 46:1021 – 1034, 2008.

[75] T. Schenk. *Modelling Welding Distortion - Influence of Clamping and Sequencing*. PhD thesis, Delft University of Technology, 2011.

[76] P.J. Withers and H.K.D.H. Bhadeshia. Residual stress part 2 - nature and origins. *Materials science and technology*, 17(4):366 – 375, 2001.

[77] D. Dean, L. Yu, S. Hisashi, and S. Masakazu. Numerical simulation of residual stress and deformation considering phase transformation effect. *Transactions of JWRI*, 32(2):325 – 333, 2003.

[78] M. Wolff and M. Böhm. On the singularity of the leblond model for trip and its influence on numerical calculations. *Journal of materials engineering and performance*, 14(1):119 – 112, 2005.

[79] D. Deng, Y. Tong, N. Ma, and H. Murakawa. Prediction of the residual welding stress in 2.25cr-1mo steel by taking into account the effect of the solid-state phase transformation. *Acta metallurgica Sinica (English Letters)*, 26(3):333 – 339, 2013.

[80] A. Mendizabal, M. San Sebastian, and A. Echeverria. Refining welding modelling for prediction of distortion incorporating mechanical effects of annealing. In T. DebRoy, S.A. David, J. DuPont, T. Koseki, and H.K. Bhadeshia, editors, *Trends in Welding Research*, pages 152 – 157. ASM International, 2012.

[81] S. Yushanov and K.C. Koppenhoefer. Computational modeling of residual stress in welds. In T.A. Siewert and C. Pollock, editors, *Eleventh International Conference on Computer Technology in Welding*, volume NIST Special Publication 973. National Institute of Standards and Technology, 2002.

[82] L-E. Lindgren and E. Hedblom. Modelling of addition of filler material in large deformation analysis of multipass welding. *Communications in Numerical Methods in Engineering*, 17:647 – 657, 2001.

[83] Dassault Systemes. Abaqus 6.14 online documentation: Abaqus user subroutines reference guide. page Chapter 1.1.41 UMAT, 2014.

[84] W.W. Wilkening and J.L. Snow. Analysis of welding-induced residual stresses with the adina system. *Computers and Structures*, 47(4/5):767 – 786, 1993.

[85] J. Outinen and P Mäkeläinen. Mechanical properties of structural steel at elevated temperatures. In *Advances in Steel Structures. Proceedings of the Third International Conference on Advances in Steel Structures*, 2002.

[86] P. Mollicone, D. Camilleri, T.G.F. Gray, and T. Comlekci. Simple thermo-elastic-plastic models for welding distortion simulation. *Journal of Materials Processing Technology*, 176:77 – 86, 2006.

[87] C-H. Lee and K-H. Chang. Finite element simulation of the residual stresses in high strength carbon steel butt weld incorporating solid-state phase transformation. *Computational Materials Science*, 46:1014 – 1022, 2009.

[88] M.R.A. Rikken. *The influence of a residual stress distribution on the fatigue crack growth rate of bead-on-plate welded steel specimens.* Master thesis, Delft University of Technology, 2016.

[89] G. Dhondt. Calculix crunchix user's manual version 2.7, 2014. URL `http://web.mit.edu/calculix_v2.7/CalculiX/ccx_2.7/doc/ccx/ccx.html`. Accessed: 15th of November, 2016.

[90] R.A. Bendigo and J.L. Rumpf. Calibration and installation of high strength bolts. *Fritz Engineering Laboratory Report*, 271, 1959.

[91] R. Elliott. Deflection of beams, 2000. URL http://www.clag.org.uk/beam.html. Accessed: 9th of February, 2017.

[92] A.M. Prokhorov. *The Great Soviet Encyclopedia*. 3 edition, 1969 - 1978.

[93] WeldCor. Encyclopedia of terms, 2013. URL http://www.weldcor.ca/encyclopedia.html?alpha=M&per_page=4. Accessed: 9th of January, 2017.

[94] S.V. Gupte. Inspection and welding repairs of pressure vessels. *The e-Journal of Nondestructive Testing*, 9(7), 2004.

[95] Total Materia. Procedures for repair welding and surfacing, 2004. URL http://www.totalmateria.com/page.aspx?ID=CheckArticle&site=kts&NM=130. Accessed: 10th of January, 2017.

[96] The Welding Institute (TWI). Manual metal arc gouging, 1995. URL http://www.twi-global.com/technical-knowledge/job-knowledge/manual-metal-arc-gouging-010/. Accessed: 9th of January, 2017.

[97] G. Shi, X. Deng, and C. Shet. A finite element study of the effecct of friction in orthogonal metal cutting. *Finite Elements in Analysis and Design*, 38:863 – 883, 2002.

[98] M. Binder, F. Klocke, and B. Doebbeler. An advanced numerical approach on tool wear simulation for tool and process design in metal cutting. *Simulation Modelling Practice and Theory*, 70:65 – 82, 2017.

[99] D.A. Doman, A. Warkentin, and R. Bauer. Finite element modeling approaches in grinding. *International Journal of Machine Tools and Manufacture*, 49:109 – 116, 2009.

[100] C. Sharma, S. Ghosh, and P. Talukdar. Finite element analysis of workpiece temperature during surface grinding of inconel 718 alloy. *5th Internationial and 26th All India Manufacturing Technology, Design and Research Conference (AIMTDR 2014)*, 2014.

[101] Windows 8 - can i disable the memory warning, 2013. URL www.overclock.net/t/1409290/windows-8-can-i-disable-the-memory-warning. Accessed: 10th of June, 2016.

[102] E. Haghighat. How to link intel fortran and abaqus / msc mark, 2015. URL https://youtu.be/ynZYVlMIFmQ. Accessed: 14th of February, 2016.

[103] Templar. How to link abaqus 6.13 with visual studio 2012 and intel fortran composer xe, 2016. URL http://tuoonline.sinaapp.com/?p=131. Accessed: 10th of February, 2016.

[104] V. Nikolaos. Linking abaqus® 6.13/6.12 with intel® fortran compiler and microsoft® visual studio, 2014. URL https://www.researchgate.net/file.PostFileLoader.html?id=57443ce296b7e46eb64deba2&assetKey=AS%3A365233358032897%401464089826204. Accessed: 2nd of February, 2016.

[105] D. Harper and L.M. Stockman, 2014. URL https://www.obliquity.com/computer/fortran/common.html. Accessed: 14th of June, 2016.

A

Material Research

A cross-sectional specimen has been made from the initial single weld, approximately 60 mm from the weld end point, and at the repaired section of the weld, 60 mm from the start of the weld. Specimens where polish and etched.

A.0.1. Visual Inspection

Macro Photography
For the specimen with the initial weld only, a relative wide HAZ can be observed. This is most likely due to the relative thin 4 mm plate. A misalignment is visible and at the right side of the weld root no connection was made between the weld material and the base material.

The repair welded section has larger HAZ compared to the single weld pass specimen. The second pass seems to have covered almost all of the previous weld metal. As boundary between the two weld materials can be found in the root of the weld. The full coverage of the repair weld and the increase in the total HAZ has most likely to with the thin plate elements. The material is relative easily fully molten, making the initial weld almost invisible by the repair weld. See Figure A.2. The difference in weld root is most likely caused due to the misalignment in Figure A.1, there is was relative harder for the weld metal to reach the bottom of the plate.

A clear line can be observed in both the specimens at half depth of the base material. Grain structure analysis show no different grain structures at this location. It is assumed the line originates from the manufacturing process.

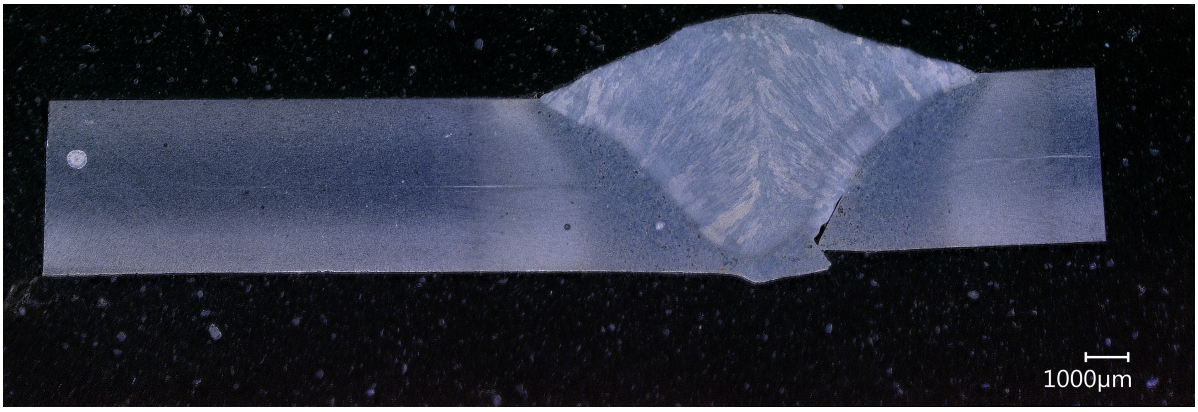

Figure A.1: Cross-sectional specimen of the single pass weld.

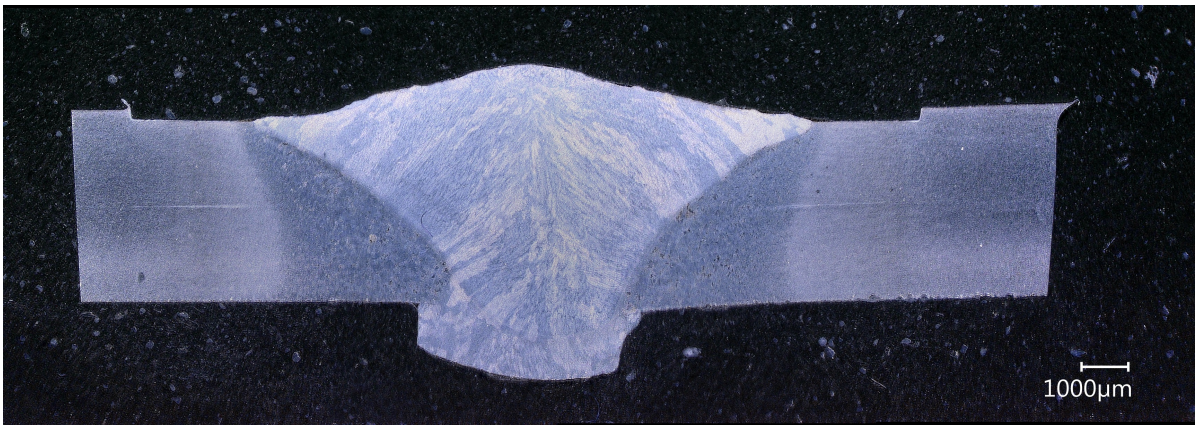

Figure A.2: Cross-sectional specimen of the repaired weld.

Micro Photography
First the single pass specimen is observed. The base material consist out of a fine ferrite structure, as a results of the thermo-mechanical rolling process (Figure A.3 and A.4). A gradual increase of grain size is observed and some Bainite structure is found in the Fine Grained Heat Affected Zone (Figure A.5 and A.6). The Coarse Grained Heat Affected zone show more formation of Bainite and Widmanstätten ferrite (Figure A.7 and A.8). The weld metal consist of an Acicular Ferrite structure A.7 and A.8.

Figure A.3: The base metal structure (x250)

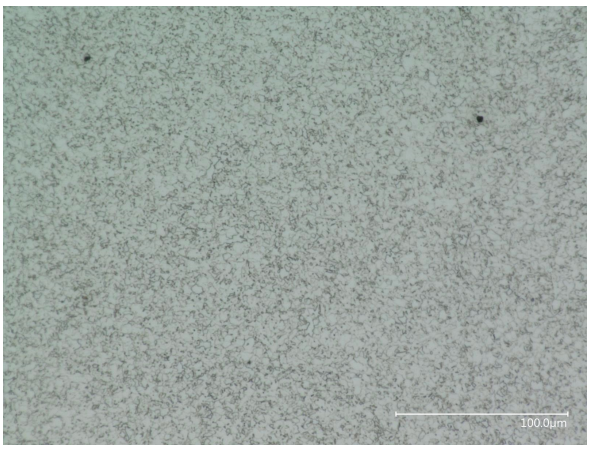

Figure A.4: The base metal structure (x1000)

Figure A.5: Fine grained heat affected zone (x250)

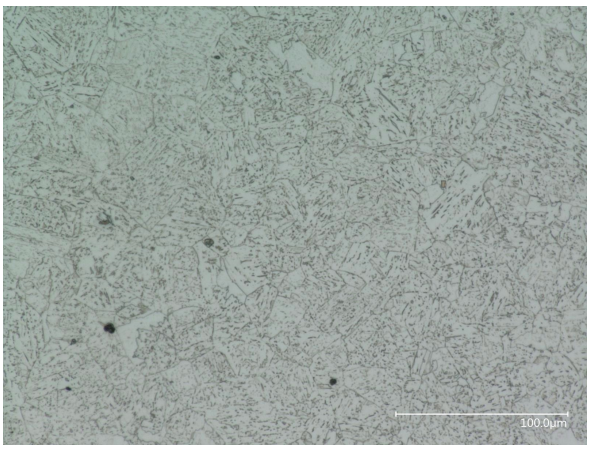

Figure A.6: Fine grained heat affected zone (x1000)

Figure A.7: Near fusion line coarse grain structure (x250).

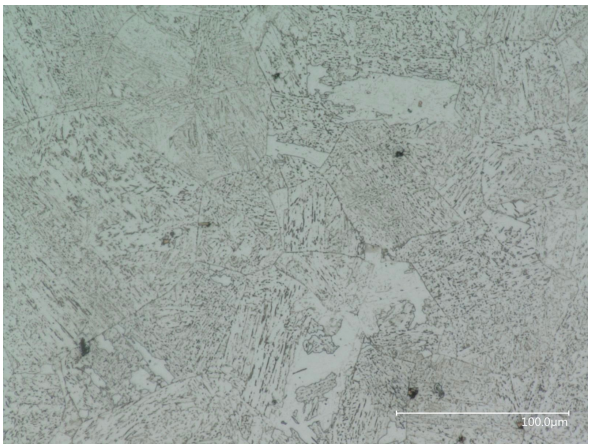

Figure A.8: Near fusion line coarse grain structure (x1000).

Figure A.9: The weld metal (x250).

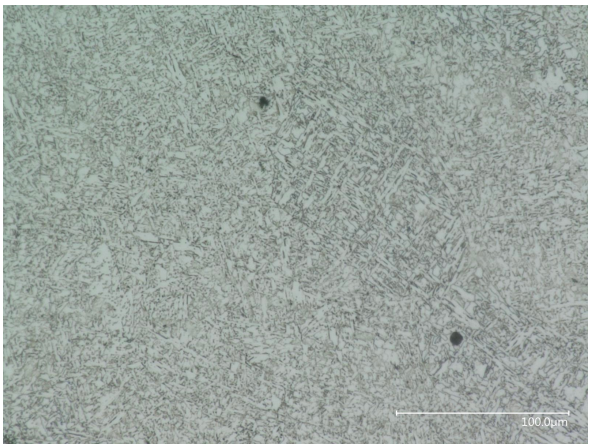

Figure A.10: The weld metal (x1000).

The second specimen, of the repair section, shows no significant changes compared to the single pass welded specimen. A fine grained base metal experiences a gradual grain size increase closer to the weld, forming Bainite structures (Figure A.11, A.12, A.13 and A.14). Closer to the weld in the Coarse Grained Heat Affected zones sections of Bainite and Widmanstätten ferrite can be found (Figure A.15 and A.16). The weld metal is of an acicular ferrite structure (Figure A.17 and A.18).

Figure A.11: The base metal structure (x250)

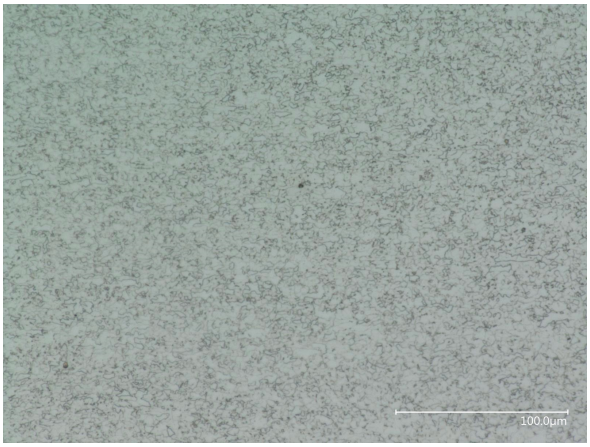

Figure A.12: The base metal structure (x1000)

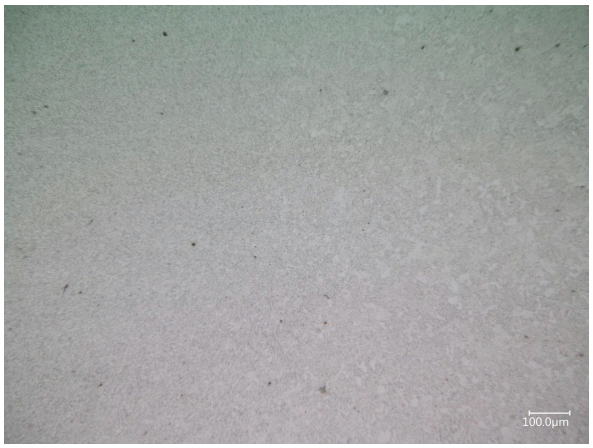

Figure A.13: Fine grained heat affected zone (x250)

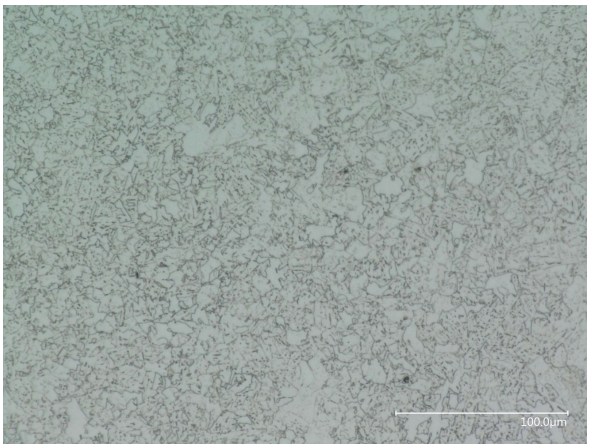

Figure A.14: Fine grained heat affected zone (x1000)

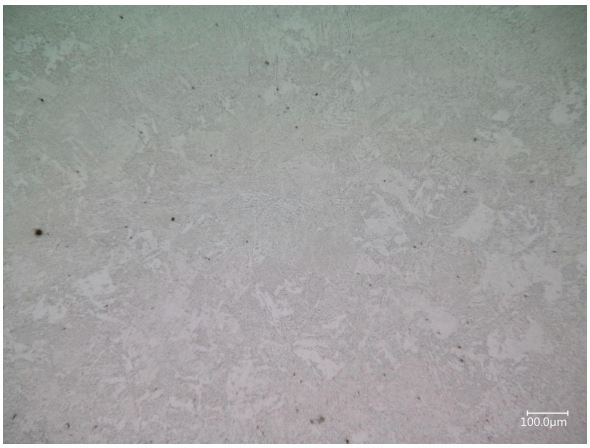

Figure A.15: Near fusion line coarse grain structure (x250).

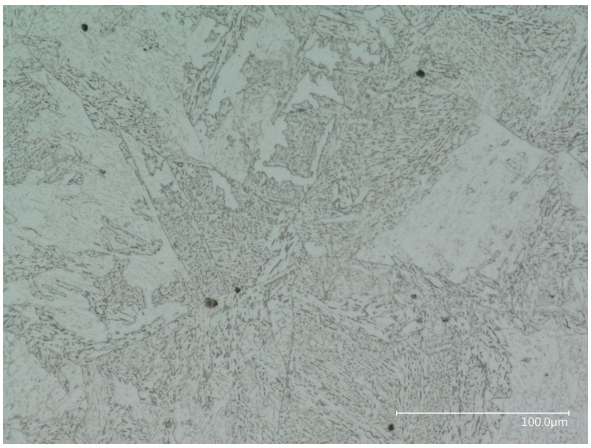

Figure A.16: Near fusion line coarse grain structure (x1000).

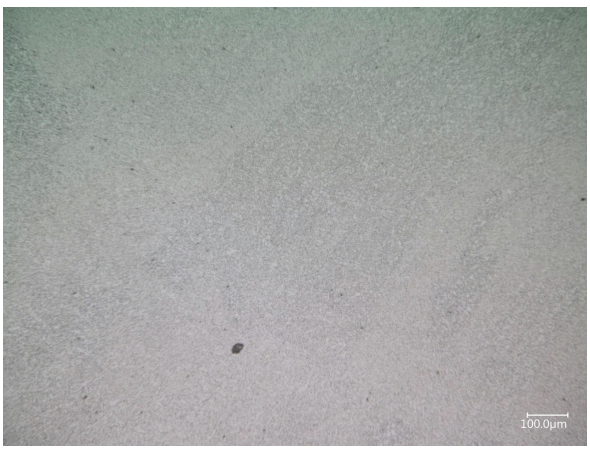

Figure A.17: The weld metal (x250).

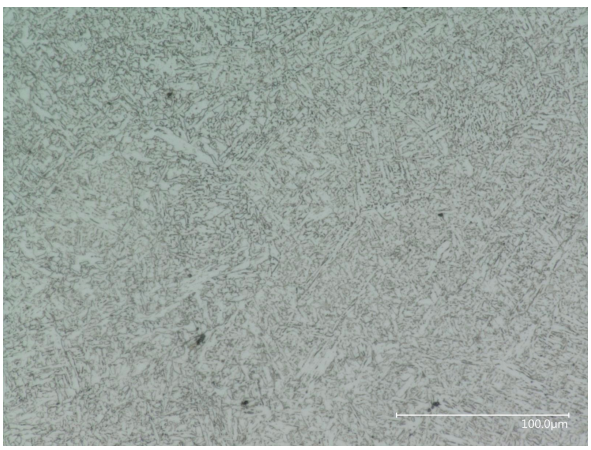

Figure A.18: The weld metal (x1000).

A.0.2. Hardness Measurement

In Figures A.19 and A.20 the hardness measurement over distance transverse over the weld can be found for the single and repaired weld, respective. In both specimen a decrease in hardness can be observed where the base material transitions into the inter-critical HAZ, due to an increase in grain size. An increase of hardness can be observed continuing further towards the weld material. This is most likely due to an increase in presence of the bainite and Widmanstätten structures. An increase in hardness is observed for the repaired specimen when the weld material is reached.

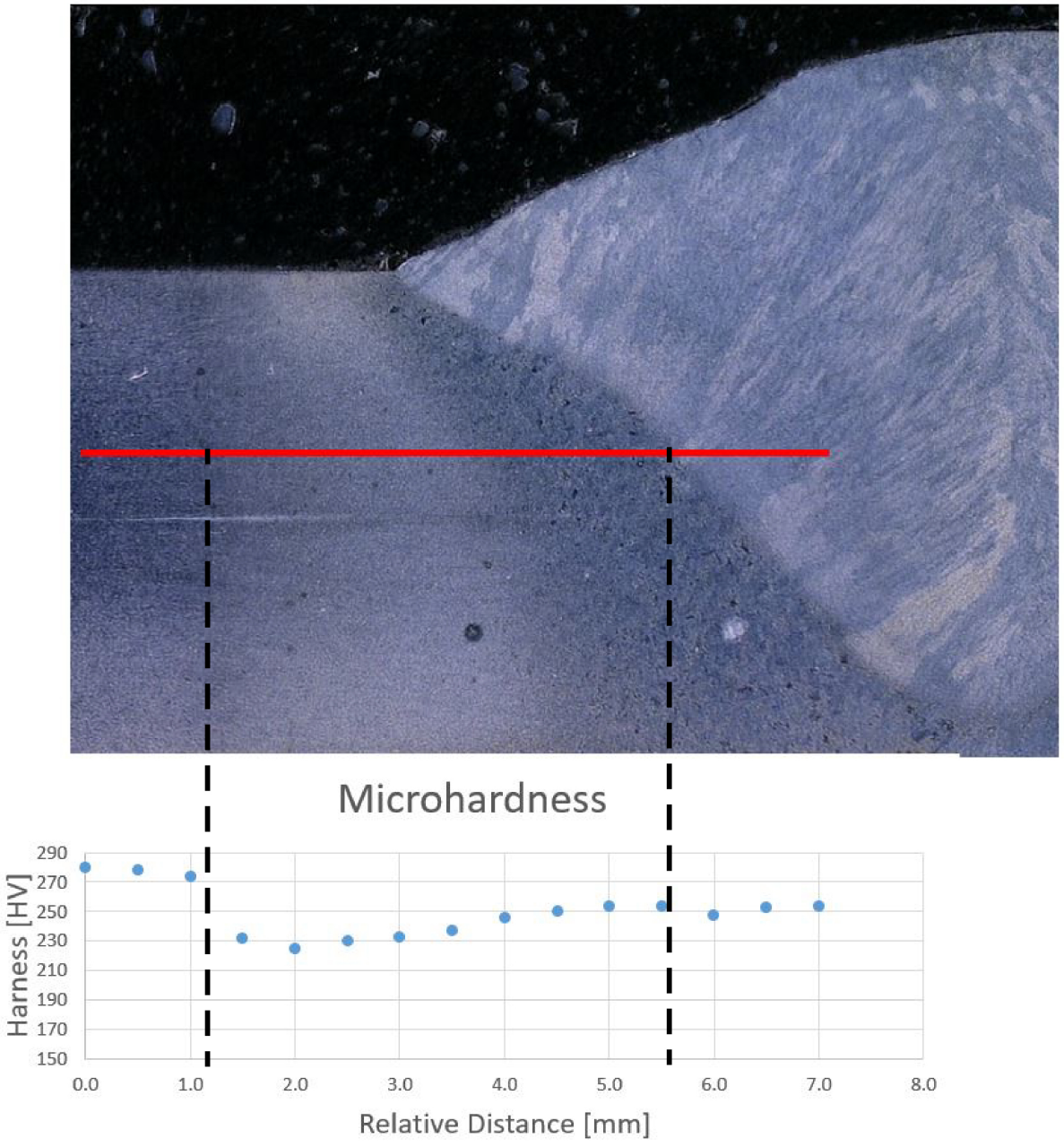

Figure A.19: Cross-section single weld with Hardness measurement points.

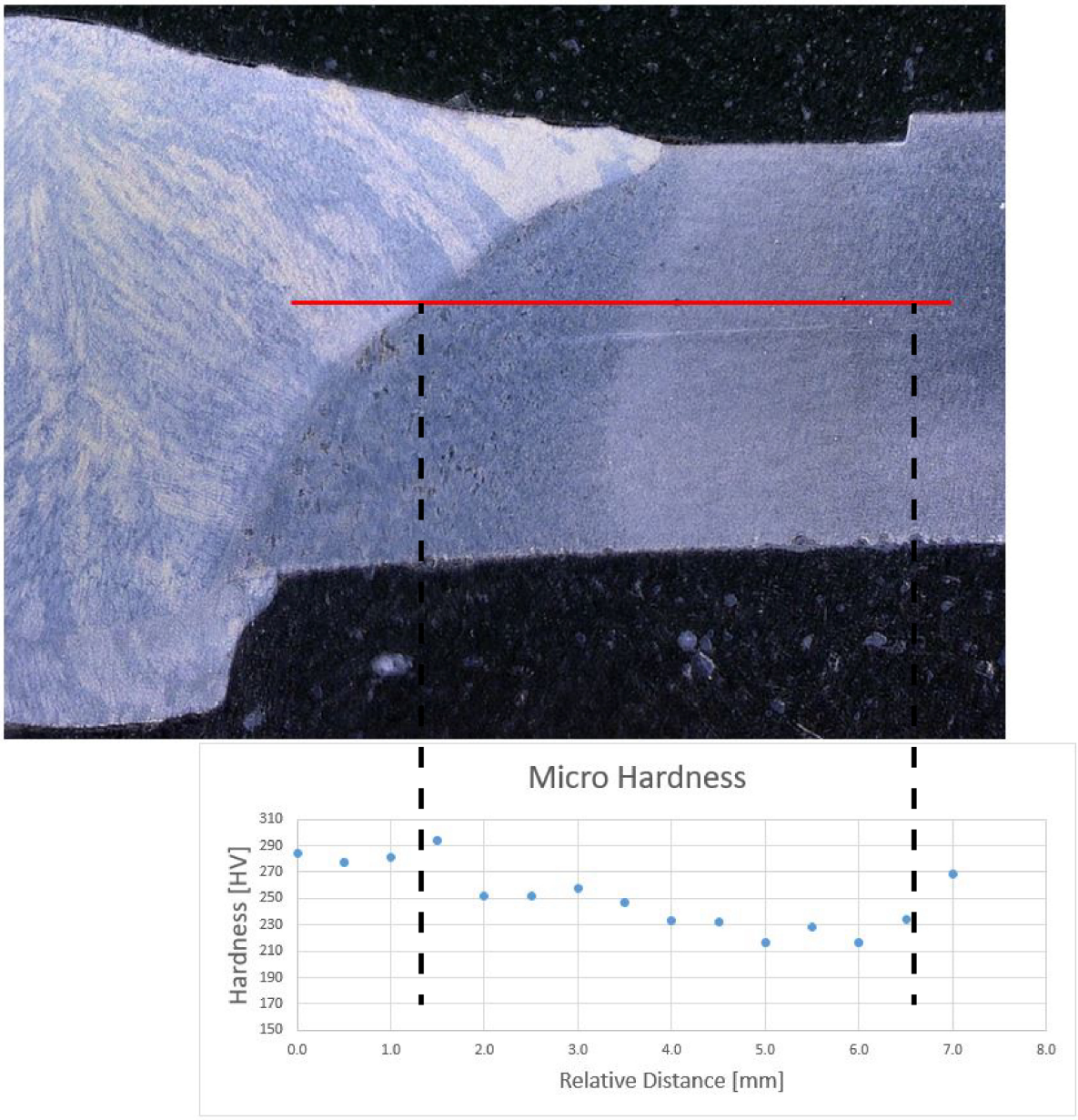

Figure A.20: Cross-section repair weld with Hardness measurement points.

B

Technical Computer Specifications

B.1. PC

These are the specifications of the hardware used to calculate the models in Abaqus. This is presented so the reader can get an idea of the relation between calculation times and computer performance for the models in this thesis.

- CPU: Intel i5-4590
- GPU: MSI/Nvidia GTX 960 4GB
- RAM: 16 GB
- HDD: Models and results were saved on a normal 7200 RPM 1TB Harddisk, also during calculation. Abaqus was installed on a 250GB SSD.

B.2. Software

An overview of what software has been used:

- Abaqus 6.14-1
- Visual Studio 2013 (Windows 10) Visual Studio 2010 (Windows 7)
- Intel Parallel Studio XE 2015 (Used for Fortran Subroutine in Abaqus, this software is a addition to Visual Studio, therefore Visual Studio has to be installed first)
- Linking the Fortran Compiler with Abaqus:
  The following video has provided a clear description for the linkage of the Fortran Compiler provided by the Intel Parallel Studio software with the Abaqus Software: `https://youtu.be/ynZYVlMIFmQ`

  One has to install the following software, to ensure that all the needed library files are present:
  - Microsoft HPC Package

B.3. Tips and Recommendation for running analyses

The following tips and recommendation are used in this thesis to make general calculations and workflow more efficient, and easy. Implementation of these points are not critical for calculation purposes, there are other ways to find solutions. But implementation will mean a more efficient and quick workflow using Abaqus.

- **Disable Windows Resource Exhaustion Detection and Resolution**
  For large computations where a percentage of memory is continuously used (>90%) for a long time, the Windows Operating System may terminate your computation, or rather the whole Abaqus Environment. To prevent this from happening, it is advised to disable 'Windows Resource Exhaustion Detection and Resolution'. To disable, follow the following steps [101]:

  - Click **Start** → Click **Search Box** → Type **gpedit.msc** and press **Enter** → the Local Group Policy Editor will open.
  - In the Navigation Tree: Expand **Computer Configuration** → Expand **Administrative Templates** → Expand **System** → Expand **Troubleshooting and Diagnostics** → Click **Windows Resource Exhaustion Detection and Resolution**
  - In the Console Pane: Right-Click **Configure Scenario Execution Level** and Click **Edit**
  - In the Configure Scenario Execution Level pane: Click **Disabled** to disable the resource exhaustion detection → Click **OK**

  Please Note, when disabled, the system will no longer detect 'memory leak' situations within the Windows Environment; not only Abaqus related processes. Therefore, this function needs to be used with caution.

- **Automatically Running Multiple Analyses Sequentially**
  Running multiple analyses sequentially may be required when a large amount of different analyses have to be run, for example for analyses with different parameters each. By running the analyses automatically and sequentially, no monitoring of job completion is needed, improving calculation and general working efficiency. Abaqus allows to run a Python based script, where jobs can be submitted for calculation. The following Python script can be used to submit multiple jobs in sequence:

```
from job import *

mdb.jobs['FirstInputFileName'].submit(consistencyChecking=off)
mdb.jobs['FirstInputFileName'].waitForCompletion()

mdb.jobs['SecondInputFileName'].submit(consistencyChecking=off
    )
mdb.jobs['SecondInputFileName'].waitForCompletion()
.
.
etc.
.
.
mdb.jobs['LastInputFileName'].submit(consistencyChecking=off)
```

where the name between the brackets: *mdb.jobs['***']* is the input file (.inp) name of the job. The input file has to be created before the script is started. This is done by **Right-Click of a job** in the Abaqus CAE and Click **Write Input**. The *.submit(consistencyChecking=off)* instance will submit the job it is connected to for analysis. The *.waitForCompletion()* instance will hold the script until the current job is either completed, aborted or terminated. When the instance of *.waitForCompletion()* is not called, all the specified jobs will be submitted, running them in parallel. Please Note, while running the Python script within the Abaqus CAE Environment, no access to the Abaqus CAE is possible. Access will continue once the Python script has been fully executed. This is especially relevant when using the *.waitForCompletion()* instance; this will hold the Abaqus CAE into the execution of the Python script. Effectively this will mean you cannot use the Abaqus CAE until the last job of the Python script is submitted.

The Python script can be written in a simple text editor as NotePad and saved as a .py file. This file can be run in the Abaqus CAE by: Clicking **File** in the Menu Bar → Click **Run Script...** → and Choose the appropriate Python (.py) file.

C

Abaqus Fortran Subroutines

This chapter discusses the Fortran language and code used in this thesis for the subroutine. First several problems regarding Fortran are explained. Problems which are regarded time consuming by the writer, and assumed useful to know for first time Abaqus (in combination with Fortran) users. The used subroutines are shown and explained by use of several flowcharts. This will give the reader a quick overview of how the code is constructed.

C.1. Abaqus Fortran

- **Implementation of Fortan with Abaqus**
  To implement Abaqus with Fortran, a separate Fortran Compiler is used. This compiler is used to send the subroutine and return a value. A coupling has to be made between Abaqus and the compiler in the target location of the Abaqus Shortcuts. For more information please check the following sources: [102–104].

- **Share Data between Increments of the Analysis**
  To share data between integration points, the User Dependent State Variable is available within the subroutine environment. This array allows the transfer of variables between increment. The State Variable is specified by using the **STATEV(*)** array, where the asterisk indicates the array index number. Not all subroutines support the use of the state variable, whether it can be used can be checked in the Abaqus Subroutines Reference Manual [63].

- **Multi-core File Read/Write and Data Sharing**
  Errors may occur in multi-core processing when using an Abaqus subroutine when you try to read a file in a subroutine and safe the values in a global variable. Errors may occur due to the parallel read out of the file, sharing read values between parallel subroutines calls.

  To prevent multi-core data share problems, one can refer to OpenMP or MPI [63] implementation. By implementing either into the Fortran code, one can allocate different problems to different processor threads, giving you more control over which core does what. Another solution is to use the Fortran Common Block. This common block allows for an allocated amount of memory to be globally available for the subroutines. During implementation of the common block, it was found that a built up of memory occurred, which eventually resulted in a failure due to inadequate amount of memory available. Commonly, the use of the common

block is discouraged, due to its many possibilities of failure [105]. A working solution was found in allocatable arrays [63]. These arrays can be saved globally and is accessible for any subroutine and safe access during a multi-threaded process is guaranteed.

To prevent read problems during multi-core calculation, the User Defined External Database subroutine (UEXTERNALDB) can be used [63]. The subroutine can be used to set up a database before or after an analysis, increment or step starts or ends. This process is a single core calculation, so safe read or write conditions to a file is guaranteed. The data can be saved in a globally available parameter, sharing the information between the subroutines.

- **Fortran Abaqus Trouble Shooting**
  When a problem occurs within the subroutine environment Abaqus will abort the current job and give an error message in the Message Area of the Abaqus CAE. But no error codes are given regarding what fault has been located within the Fortran Compiler. Error Messages are printed in the .log-file of the job with the similar name. In this .log-file the errors occur which the Fortran Compiler has discovered and code errors can consequently be located. Also useful for trouble shooting is displaying values. When using **WRITE(*,*) 'Any string here'**, a string or value can be written to the same .log file, making the coding in Fortran together with Abaqus easier to trouble shoot.

C.2. Heat Analysis Subroutines

This section explains all the subroutines used in the thermal or heat analyses using a Goldak shape heat density distribution.

C.2.1. Abaqus USDFLD-Subroutine

The User Defined Field Variable (USDFLD) subroutine is used to specify field variables which in turn correspond with a certain material property [63]. Tabulated data in the material property property section is interpolated between the values of the specified field variable distribution, see Chapter 5.3.4. Using this subroutine, material properties can be made solution dependent.

During the heat analysis this subroutine is used to read the element temperature data, since the critical heat analysis subroutine, the DFLUX-subroutine, does not allow for temperature data to be read. Temperature data of elements within a certain coordinate box surrounding the weldpool are read out and saved once the element has reached a temperature above a certain predefined threshold. In this example subroutine, the final parameters used in the analyses are not presented and most likely are different than the parameters presented in this thesis. First the flowchart is shown, than the code itself.

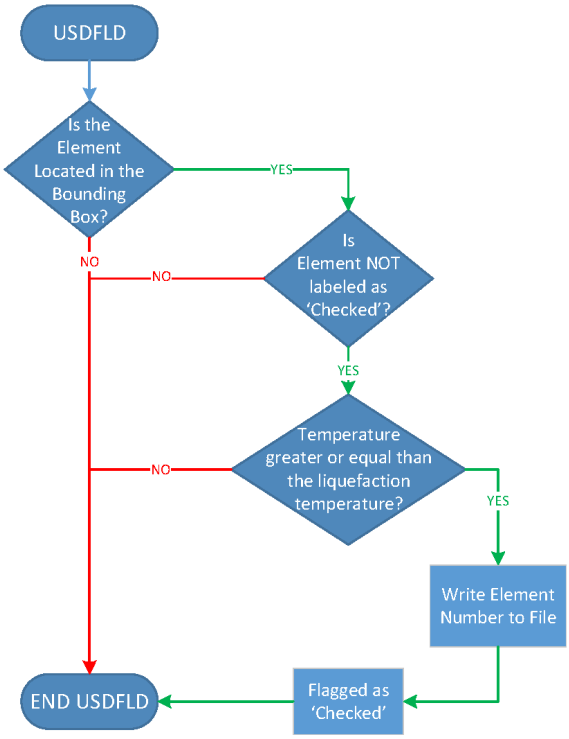
USDFLD
Is the Element Located in the Bounding Box?
YES
NO
Is Element NOT labeled as 'Checked'?
NO
YES
Temperature greater or equal than the liquefaction temperature?
NO
YES
Write Element Number to File
Flagged as 'Checked'
END USDFLD

```
      SUBROUTINE USDFLD(FIELD,STATEV,PNEWDT,DIRECT,T,CELENT,
      1 TIME,DTIME,CMNAME,ORNAME,NFIELD,NSTATV,NOEL,NPT,
      2 LAYER,KSPT,KSTEP,KINC,NDI,NSHR,COORD,JMAC,JMATYP,
      3 MATLAYO,LACCFLA)
C
      INCLUDE 'ABA_PARAM.INC'
C
      CHARACTER*80 CMNAME,ORNAME
      CHARACTER*3  FLGRAY(15)
      DIMENSION FIELD(NFIELD),STATEV(NSTATV),DIRECT(3,3),
      1 T(3,3),TIME(2)
      DIMENSION ARRAY(15),JARRAY(15),JMAC(*),JMATYP(*),COORD(*)
C     !=====================================================
      xx      = COORD(2)      !Transverse Coordinate of the Element.

      ! Heat Flux and Element coordinates are used to define a box
         surrounding
      ! the Heat flux, making the analysis more efficient.
      IF(xx .LE. (0.005) .AND. xx .GE. (-0.005)) THEN
       zz     = COORD(1)              ! Longitudinal Coordinate of the
          Element.
       fLL    = 0.005*TIME(1) - 0.044 ! Longitudinal Coordinate of Heat
          Flux.
       ffLL   = fLL + 0.015           ! Distance in front of Heat Flux
          Coord.
       rfLL   = fLL - 0.025           ! Distance behind Heat Flux
          Coordinate.

       IF(zz .LE. ffLL .AND. zz .GE. rfLL) THEN
        IF(STATEV(1) .NE. (1.0)) THEN
         softTemp     = 1480.0        ! Softening Temperature for
            Material
                                      ! [degree Celsius]

         !A CALL is made to retrieve current Temperature data of the
            element.
         CALL GETVRM('TEMP',ARRAY,JARRAY,FLGRAY,JRCD,JMAC,JMATYP,
         1    MATLAYO,LACCFLA)

         curTemp      = ARRAY(1)      !The current temperature is saved
            as
                                      !curTemp

         ! If the softening Temperature has been exceeded, the element
            is
         ! flagged by setting State Variable equal to 1.0
         IF(curTemp .GE. softTemp) THEN
          ! The specific element number is saved in the analysis .log
             file.
```

```
            ! To be used in the mechanical analysis.
            WRITE(*,'(I5)') NOEL
            STATEV(1)    = 1.0
           ENDIF
          ENDIF
         ENDIF
        ENDIF

C       ================================================

        RETURN
        END
```

C.2.2. Abaqus DFLUX-Subroutine

The Distributed Flux (DFLUX) subroutine allows the user to define a non-uniform heat flux in a heat transfer analysis [63]. In this example subroutine, the final parameters used in the analyses are not presented and most likely are different than the parameters presented in this thesis. See Chapter 5.1.2 for an explanation of the Goldak heat distribution. See Chapter 6.1 for the used parameters in this thesis. No Flow Chart of the code is presented due to the relative clear code (adopted from Gao [8]).

```
        SUBROUTINE DFLUX(FLUX,SOL,JSTEP,JINC,TIME,NOEL,NPT,COORDS,
        1 JLTYP,TEMP,PRESS,SNAME)
        C
        INCLUDE 'ABA_PARAM.INC'
        C
        DIMENSION FLUX(2),TIME(2),COORDS(3)
        CHARACTER*80 SNAME
C       !=====================================================
        pi      = 3.14159       !Define Pi
        FLUX(1) = 0             !To be sure the Flux is zero to start with
            .

        I       = 170.0         !Welding Current [A]
        Vo      = 22.1          !Welding Voltage [V]
        eff     = 0.5221        !Welding Power Efficiency [-]

        Q       = I*Vo*eff      !Welding Power Input [Watt]

        v       = 0.005         !Welding Speed [m/s]
        st      = -0.010        !Starting Point relative to Origin of
           moving
                                !axis. Minus is backwards, Positive
                                   forwards.[m]

        x       = COORDS(1)     !x-axis coordinate of element. Transverse.
        y       = COORDS(2)     !y-axis coordinate of element. Out-of-
           Plane.
        z       = COORDS(3)     !z-axis coordinate of element.
           Longitudinal.
```

```
      t       = TIME(1)       !Current Time [sec]

      a       = 0.003         !Goldak shape parameter x-axis [m]
      b       = 0.005         !Goldak shape parameter y-axis [m]

      IF(z.ge.(v*t+st)) THEN  !Front Flux Heat Distribution
       cf     = 0.003         !Goldak shape parameter z-axis, Front [m]
       ff     = 0.6           !Fraction of Power in Front [-]

       ef     = exp(-3*((x/a)**2+(y/b)**2+((z-v*t-st)/cf)**2))
       FLUX(1)= ((6*sqrt(3.0)*Q*ff)/(a*b*cf*(pi*sqrt(pi))))*ef
      ENDIF

      IF(z.le.(v*t+st)) THEN  !Rear Flux Heat Distribution
       cr     = 0.006         !Goldak shape parameter z-axis, Rear  [m]
       fr     = 1.4           !Fraction of Power in Rear  [-]

       er     = exp(-3*((x/a)**2+(y/b)**2+((z-v*t-st)/cr)**2))
       FLUX(1)= ((6*sqrt(3.0)*Q*fr)/(a*b*cr*(pi*sqrt(pi))))*er
      ENDIF
C     !=====================================================
      RETURN
      END SUBROUTINE DFLUX
```

C.3. Mechanical Analysis Subroutines

This section explains the coding used during the Mechanical Analysis of the welding simulation.

C.3.1. Abaqus USDFLD-Subroutine

The USDFLD-subroutine is used during the mechanical analysis to perform the following four functions: checks which elements melt during the analysis, keeps track of which element is heating or cooling, keeps track of the temperature to activate thermal expansion and allocates user defined material properties. First a flow chart is present, after which the code is presented. In this example subroutine, the final parameters used in the analyses are not presented and most likely are different than the parameters presented in this thesis.

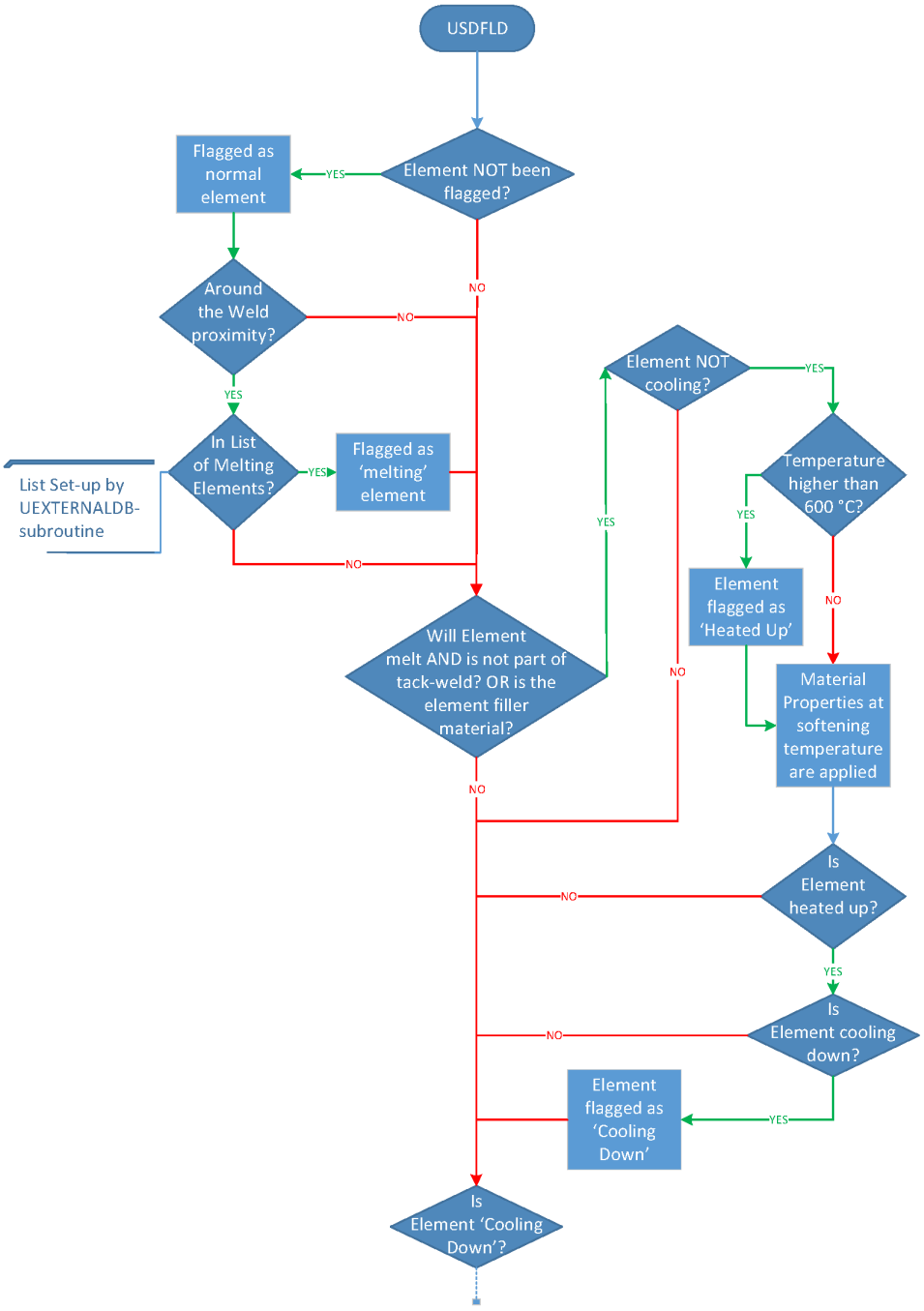

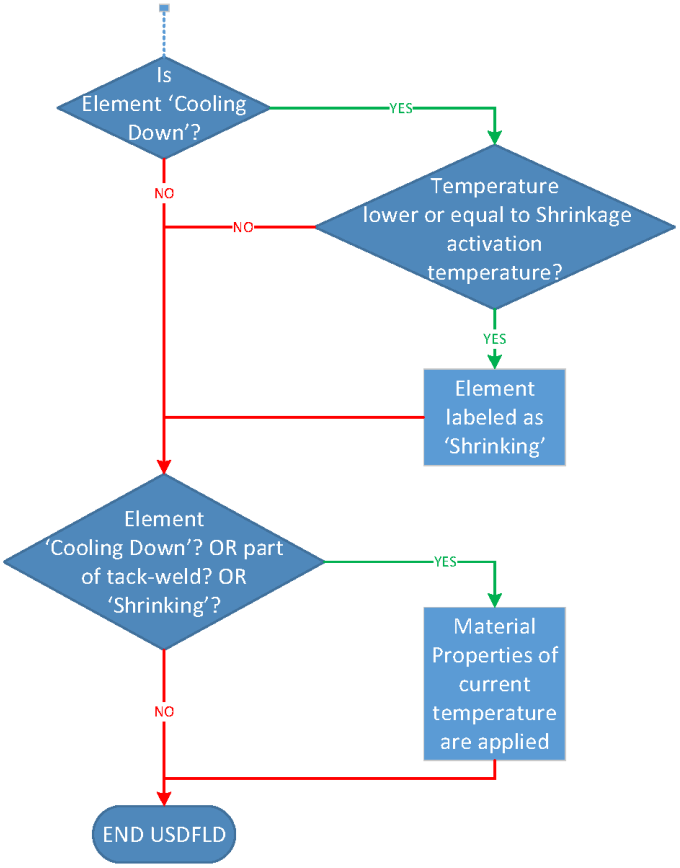
Is Element 'Cooling Down'?
YES
NO
Temperature lower or equal to Shrinkage activation temperature?
NO
YES
Element labeled as 'Shrinking'
Element 'Cooling Down'? OR part of tack-weld? OR 'Shrinking'?
YES
Material Properties of current temperature are applied
NO
END USDFLD

```
      SUBROUTINE USDFLD(FIELD,STATEV,PNEWDT,DIRECT,T,CELENT,
      1 TIME,DTIME,CMNAME,ORNAME,NFIELD,NSTATV,NOEL,NPT,
      2 LAYER,KSPT,KSTEP,KINC,NDI,NSHR,COORD,JMAC,JMATYP,
      3 MATLAYO,LACCFLA)
C
      INCLUDE 'ABA_PARAM.INC'
#INCLUDE <SMAAspUserSubroutines.hdr>     ! Needed to Read Data loaded in
                                         ! UEXTERNALDB-subroutine.
C
      CHARACTER*80 CMNAME,ORNAME
      CHARACTER*3  FLGRAY(15)
      DIMENSION FIELD(NFIELD),STATEV(NSTATV),DIRECT(3,3),
      1 T(3,3),TIME(2)
      DIMENSION ARRAY(15),JARRAY(15),JMAC(*),JMATYP(*),COORD(*)

      INTEGER i,dowh                     ! Initiate integers i and dowh
      INTEGER ar(100000)                 ! Initiate integer array ar()
      POINTER(ptra,ar)                   ! POINTER needed for shared memory
                                         ! allocation
C     !=====================================================

      softTemp        = 2000.0        !Softening Temperature for
         Material
                                         ![degree Celsius]
      actvTemp        = 1000.0        ! Shrinkage activation temperature
                                         ![degree Celsius]

      CALL GETVRM('TEMP',ARRAY,JARRAY,FLGRAY,JRCD,JMAC,JMATYP,
      1       MATLAYO,LACCFLA)         ! A CALL is made to retrieve
         current
                                         ! Temperature data of the element.

      curTemp         = ARRAY(1)      ! Current Temperature is saved as
         curTemp

C     !The following if-statement will determine whether the element
C     !has reached certain condition. Allocating State-Variable STATEV
   (1)
C     !accordingly.

      IF(STATEV(1) .EQ. (0.0)) THEN    ! Check whether element already '
         flagged'
       STATEV(1)      = 2.0            ! Set equal to 2.0 (State Variable
           1), as
                                         ! start (normal element)

       ! Within the specified coordinates, elements are checked to have
          molten
       ! using data from UEXTERNALDB-subroutine data.
       ! When is element is in the data, flagged with a 1.0 in State
```

```
            Variable 1.
          IF(COORD(2) .GE. (-0.005) .AND. COORD(2) .LE. (0.005)) THEN
           dowh          = 0
           i             = 1
           ptra = SMAIntArrayAccess(1)
           DO WHILE(dowh == 0)
            IF(ar(i) .EQ. NOEL) THEN
             STATEV(1)   = 1.0
             dowh        = 1
            ELSE IF((ar(i) .EQ. (-1)) .OR. (ar(i) .EQ. (0))) THEN
             dowh        = 1
            ELSE
             i           = i + 1
            ENDIF
           END DO
          ENDIF
         ENDIF

C        ! According to the allocated STATEV(1), element material behaviour
     will be
C        ! set. Weld Metal (to be deposited), molten base material and not
    molten
C        ! base material.

         ! If material is weldpool but not the tack weld
         IF((STATEV(1) .EQ. (1.0) .AND. CMNAME .NE. 'TACK') .OR. CMNAME .EQ
            . 'MAT-WELD') THEN
          IF(STATEV(3) .NE. (12.5)) THEN ! Element not yet shrinking! Not
             cooling
                                         ! nor uexpan active.
           IF(curTemp .GT. (600.0)) THEN ! Extra check for low temperature
                                         ! shrinkage.
            STATEV(3)    = 23.0          ! Flag: Element is heating up.
           ENDIF

           prevTemp      = STATEV(2)     ! Last known temperature data is
              prevTemp.

           FIELD(1)      = softTemp      ! Current (softened) material
              properties
                                         ! are applied.
           STATEV(2)     = curTemp       ! Current known temperature is
              loaded, to
                                         ! be used in next step for
                                            prevTemp.
           IF(STATEV(3) .EQ. (23.0)) THEN  ! If element is heating up.
            IF(prevTemp .GT. curTemp) THEN ! If previous temperature is
               higher than
                                           ! current temperature (= cooling
                                              ).
             STATEV(3)   = 12.5            ! Flag: Element is cooling
```

```
          ENDIF
         ENDIF
        ENDIF
       ENDIF

C      !
   ------------------------------------------------------------------------



       IF(STATEV(3) .EQ. (12.5)) THEN  ! If element is cooling.
        IF(curTemp .LT. actvTemp) THEN ! If activation temperature has
           been
                                       ! reached during cooling.
         STATEV(3) = 6.25              ! Flag: Shrinkage/Thermal Strain
            is
                                       ! activated in UEXPAN-subroutine.
        ENDIF
       ENDIF

       ! Normal/current Temperature material properties are applied for
          cooling
       ! and tack weld elements.
       IF((STATEV(3) .EQ. (12.5)) .OR. (CMNAME .EQ. 'TACK') .OR. (STATEV
          (3) .EQ. (6.25))) THEN
        FIELD(1)               = curTemp
       ENDIF

C      !=====================================================

       RETURN
       END
```

C.3.2. Abaqus UEXPAN-Subroutine

The UEXPAN-subroutine defines the thermal expansion behaviour of an element. In this model, thermal expansion is active unless the element is part of the weld pool. If it is part of the weldpool, thermal expansion is only activated during the cooling process. The USDFLD-subroutine tracks when the thermal expansion has to be activated, based on the current temperature of the element. First a flow chart is present, after which the code is presented. In this example subroutine, the final parameters used in the analyses are not presented and most likely are different than the parameters presented in this thesis.

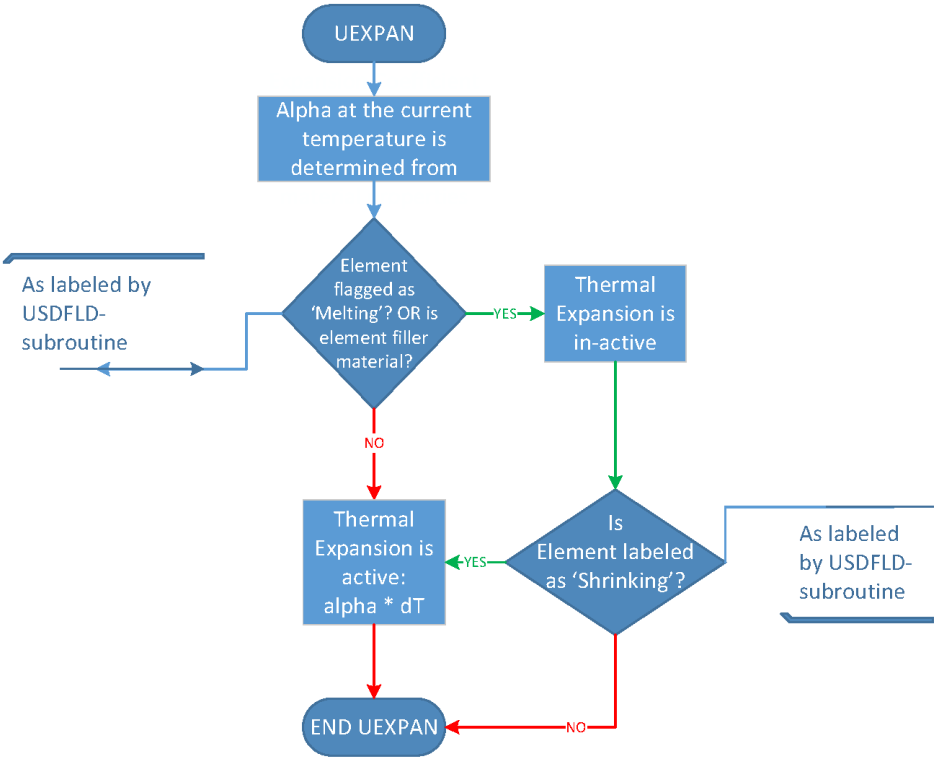
UEXPAN
Alpha at the current temperature is determined from
Element flagged as 'Melting'? OR is element filler material?
YES
Thermal Expansion is in-active
As labeled by USDFLD-subroutine
NO
Thermal Expansion is active: alpha * dT
YES
Is Element labeled as 'Shrinking'?
As labeled by USDFLD-subroutine
END UEXPAN
NO

```
      SUBROUTINE UEXPAN(EXPAN,DEXPANDT,TEMP,TIME,DTIME,PREDEF,
      1 DPRED,STATEV,CMNAME,NSTATV,NOEL)
C
      INCLUDE 'ABA_PARAM.INC'
C
      DIMENSION EXPAN(*),DEXPANDT(*),TEMP(2),TIME(2),PREDEF(*),
      1 DPRED(*),STATEV(NSTATV)
      CHARACTER*80 CMNAME
C     ======================================================
C     ! Interpolation of Thermal Expansion Coeff. Values
C     ! Thermal Expansion Values for S700MC [1/K]

      IF(TEMP(1).le.(16.0)) THEN
       alpha_1        = 0.0000139
      ELSEIF(TEMP(1).gt.(16.0) .AND. TEMP(1).le.(353.0)) THEN
       t1 = 16.0
       a1 = 0.0000139
       t2 = 353.0
       a2 = 0.0000144

       alpha_1        = a1+(TEMP(1)-t1)*(a2-a1)/(t2-t1)
      ELSEIF(TEMP(1).gt.(353.0) .AND. TEMP(1).le.(617.0)) THEN
       t1 = 353.0
       a1 = 0.0000144
       t2 = 617.0
       a2 = 0.0000161

       alpha_1        = a1+(TEMP(1)-t1)*(a2-a1)/(t2-t1)
      ELSEIF(TEMP(1).gt.(617.0) .AND. TEMP(1).le.(805.0)) THEN
       t1 = 617.0
       a1 = 0.0000161
       t2 = 805.0
       a2 = 0.000014

       alpha_1        = a1+(TEMP(1)-t1)*(a2-a1)/(t2-t1)
      ELSE
       alpha_1        = 0.000014
      ENDIF
C     ------------------------------------------------------
C     ! Here the condition of when to apply thermal strain are set
C     ! TempTrans should be the same as thermal analysis output!
      ! If element is 'molten' or element is added weld material
      IF(STATEV(1) .EQ. (1.0) .OR. CMNAME .EQ. 'MAT-WELD') THEN
       EXPAN(1) = 0.0                 ! Expansion is not present
       IF(STATEV(3) .EQ. (6.25)) THEN ! 'Flag' received from the USDFLD-
                                      ! subroutine, to activate
                                         shrinkage.
        EXPAN(1) = alpha_1*TEMP(2)    ! Thermal expansion: alpha * dT
       ENDIF
      ELSE
```

```
          EXPAN(1) = alpha_1*TEMP(2)      ! Thermal expansion: alpha * dT
        ENDIF
C       ===================================================
        RETURN
        END
```

C.3.3. Abaqus UEXTERNALDB-Subroutine

The UEXTERNALDB-subroutine allows for a single-cored process at, for example, the beginning of an analysis step. In this model the UEXTERNALDB-subroutine is used to read out the data-file made by the heat analysis at the beginning of the analysis. First a flow chart is present, after which the code is presented. In this example subroutine, the final parameters used in the analyses are not presented and most likely are different than the parameters presented in this thesis.

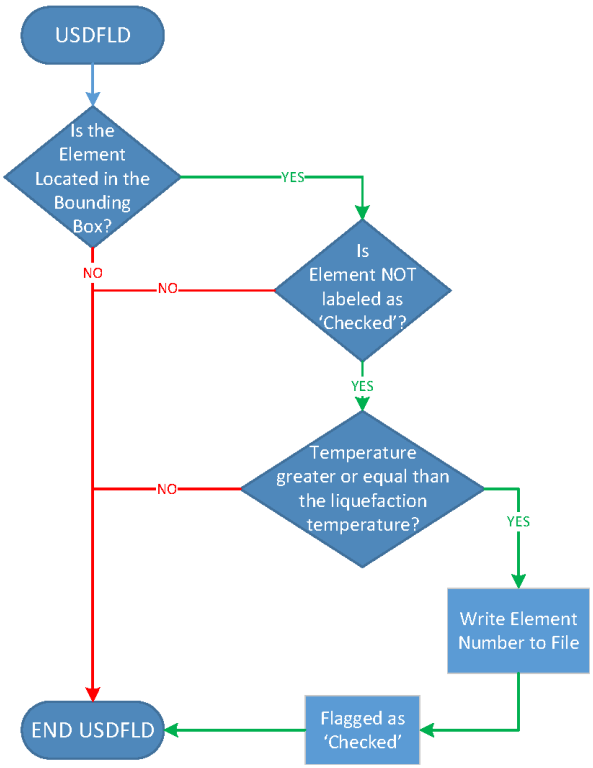

```
      SUBROUTINE UEXTERNALDB(LOP,LRESTART,TIME,DTIME,KSTEP,KINC)
C
      INCLUDE 'ABA_PARAM.INC'
#INCLUDE <SMAAspUserSubroutines.hdr>  ! Needed to Share Data to other
   subroutines.
C
      DIMENSION TIME(2)

      INTEGER i               ! Initiate integer i
      INTEGER ar(100000)      ! Initiate Integer Array
      POINTER(ptra,ar)        ! POINTER needed for shared memory
         allocation

C     ============================================================
C     Is used to initialise at the beginning of the analysis
C     a database, read from a file which contains the elements
C     which reached a certain specified temperature.

      IF(LOP .EQ. 0) THEN     ! Checks whether at beginning of the
         analysis.
       OPEN(UNIT = 8, FILE = "D:\\SIMULIA\\TEMP\\Tom-3D-Heat-Open-Write-
          Long.txt")                ! Open the list of Element number
          which have reach
                               ! the softening Temperature.

       ! Create a global array with ID=1, SIZE=100000 and INITVAL=-1 (
          Initial
       ! Value)
       ptra   = SMAIntArrayCreate(1,100000,-1)        ! POINTER Data
          Specified.
       i      = 1

       ! This WHILE loop saves the data from the text-file to a global
          array.
       DO WHILE (ios == 0)
        READ(8,'(I5)',IOSTAT=ios) ar(i)
        IF(ar(i) .eq. (0)) THEN
         ios  = 0
        ENDIF
        i     = i + 1
       END DO

       CLOSE(UNIT = 8)

      ENDIF

C     ============================================================
      RETURN
      END
```

D

How-to: Heat and Sequential Stress Analysis

From own experience, it was found that information on how to implement a Heat Transfer and subsequent Stress analysis in the Abaqus Software environment, was generally lacking. A lot of information is available from the Abaqus Manuals, but it is not clear for people just starting to work within Abaqus.

This chapter will provide an explanation on how to perform a basic heat transfer analysis, including the use of an user defined subroutine. Furthermore, a procedure will be described of the stress analysis based on the heat transfer analysis.

D.1. Heat Transfer Analysis

This section provides a procedure to perform a heat transfer analysis within the Abaqus Environment. All steps have been performed within the Abaqus CAE. Abaqus 6.14 was used for the procedure, the interface may be different when using older or newer versions.

The method used is one of a heat flux thermal analysis. The heat flux represent an energy distribution, where during the analysis the temperature increase, due to the addition of this energy is determined.

A basic knowledge of Abaqus is assumed, only specific Heat Transfer analysis aspects will be discussed. Basic functions within the Abaqus CAE, as for example how to make a part, are widely discussed in literature and can easily be found on the internet.

All the following specified values are giving in SI Units, using meters. As long as specified units are consistent, any system of measurement is possible, Abaqus does not use predefined unit values.

The heat transfer procedure within Abaqus is as follows:

1. Edit model attributes

- Where:
  Menu Bar: Click **Model** → Click **Edit Attributes** → Choose your model.
  Within the now opened 'Edit Model Attributes' dialog window, see 'Physical Constants'.
- Values:
  Absolute zero temperature: -273.15 (when using degree Celsius, 0 when using degree Kelvin)
  Stefan-Boltzmann constant: $5.67E-008$
- Why:
  The Absolute Zero Temperature attribute has to be set to determine whether the specified temperatures further in the model are based on degree Kelvin, Celsius or other temperature scales.

  The Stefan-Boltzmann constant is needed to calculate the radiation heat losses.

2. Create a Part
   - Create the part which will be subjected to the heat flux, any shape is possible.
3. Create Part Mesh
   - When meshing the part, elements have to be assigned a different element type than the default.
   - Where: (when in the Mesh Module)
     Menu Bar: Click **Mesh** → Click **Element Type..** Within the now opened 'Element Type' dialog window, see 'Family'.
   - Values:
     Family: Heat Transfer
   - Why:
     To let Abaqus know you will going to calculate heat transfer only.
4. Create Material

   For a heat transfer analysis using a heat flux the following material properties have to be defined:
   - Density - Under General in 'Edit Material' dialog box
   - Conductivity - Under Thermal in 'Edit Material' dialog box
   - Specific Heat - Under Thermal in 'Edit Material' dialog box
5. Create Section
   - Create the section at which the material can be assigned to.
6. Assign Section
   - Assign the section to the appropriate part(s)
7. Create Instance

- When creating the instance for the model, care should be taken on the location of the origin of axis system.
- Why:
  The origin of the instance corresponds with the coordinates used in the heat flux subroutine. It is advised to place the origin in the most convenient way, in such manner scripting in the subroutine may be reduced.

8. Edit the initial Step

   - Create a Predefined Field - Temperature
     - Where:
       - ◇ In the model tree, expand 'Steps' and expand 'Initial'.
       - ◇ Right-click 'Predefined Fields'.
       - ◇ Click **Create...** in the dropdown menu.
       - ◇ In the 'Create Predefined Field' dialog box, see 'Category'.
       - ◇ Click the radio button 'Other'.
       - ◇ Select the 'Temperature' type in 'Types for Selected Step'.
     - Values:
       Distribution: Direct specification
       Section variation: Constant through region
       Magnitude: The initial temperature of your model, commonly room temperature.
     - Why:
       By default, Abaqus will used 0 degrees as the initial temperature. This will lead to a mismatch in temperature measurement when comparing simulation results to experimental thermal results.

9. Create a new Step

   - In the 'Create Step' dialog box, click the 'Heat transfer' procedure.
   - Edit the created Step
     - Where:
       Under the 'Basic' tab.
     - Value:
       Time period: The length of your analysis in seconds. This is the time which is simulated. Thus; when a real experiment of 50 seconds long is simulated, 50 seconds (or more, for analysing the cooling behaviour) should be used.

     - Where:
       Under the 'Incrementation' tab.
     - Value:
       Max. allowable temperature change per increment: set a small enough value, so ΔT is not too large. This particularly relevant when using this thermal analysis for a mechanical analysis.

       Choose appropriate 'increment size' parameters. Which is highly model-dependent.

10. Edit created Step

    - Create a Load
      - Only thermal loads are possible, select 'Body heat flux' in the 'Create Load' dialog box.
        Select the whole model to apply the load on.
      - Values:
        Distribution: User-defined
        Magnitude: 1
      - Why:
        This allows for a heat flux distribution using a DFLUX subroutine.
        The magnitude is the multiplication factor of the subroutine
    - Create Interaction
      - Convection and Conduction Losses
        - Where:
          In 'Create Interaction' dialog box, click 'Surface film condition'.
          Select the appropriate surface which the film conditions is applied on.
        - Values:
          Film coefficient: values suitable for your welding condition and material.
          Sink temperature: The reference temperature on which the heat losses will be calculated, commonly room temperature.
        - Why:
          Surface film condition represents the heat losses due to convection and/or conduction of the surface area. See Section 6.4.
      - Radiation Losses
        - Where:
          In 'Create Interaction' dialog box, click 'Surface radiation'.
          Select the appropriate surface which the radiation is applied on.
        - Values:
          Emissivity: value suitable for your welding condition and material.
          Ambient temperature: The reference temperature on which the heat losses will be calculated, commonly room temperature.
        - Why:
          Surface radiation represents the heat losses due to convection and/or conduction of the surface area. See Section 6.4.
    - Edit Field Output Request
      - Check the checkboxes: Nodal Temperature (NT) and Element temperature (TEMP) to output the temperature data sufficiently.

11. Create a Job

    - Edit Job
      - Where:
        In the 'Edit Job' dialog box, see the 'General' tab.

  - Values:
    User subroutine file: insert the location of the fortran-file for the subroutines used.
  - Why:
    This is how Abaqus knows where the subroutine file is located.

12. Submit and Run the Job

D.2. Sequential Stress Analysis

This section provides a procedure to perform a sequential stress analysis within the Abaqus Environment. All steps have been performed within the Abaqus CAE. Abaqus 6.14 was used for the procedure, the interface may be different when using older or newer versions.

The method used is one of a stress analysis, which originates from an applied thermal history. A basic knowledge of Abaqus is assumed, basic functions, as for example how to make a part, are widely discussed in literature and can easily be found on the internet.

All the following specified values are giving in SI Units, using meters. As long as specified units are consistent, any system of measurement is possible, Abaqus does not use predefined unit values.

The sequential stress procedure within Abaqus is as follows:

1. Copy the Heat Transfer Model Why:
   The parts and most importantly the elements have to be the same numbering in the sequential stress analysis. This way the correct thermal behaviour can be assigned to the correct element.

2. Edit Part Mesh

   - Where: Similar to Step 3, the Element Type is changed.
     See 'Family' in 'Element Type' dialog window
   - Value: Family: 3D Stress
   - Why: Now stresses have to be calculated, so 3D stress elements are needed

3. Create Material

   For a stress analysis based on thermal input the following material properties have to be defined:

   - Elastic - Under Mechanical and Elasticity in 'Edit Material' dialog box
   - Plastic- Under Mechanical and Plasticity in 'Edit Material' dialog box
   - Expansion - Under Mechanical in 'Edit Material' dialog box

4. Create Section

   - Create the section at which the material can be assigned to.

5. Assign Section

   - Assign the section to the appropriate part(s)

6. Assign Section
    - Assign the section to the appropriate part(s)
7. Re-generate the Instance
8. Create Boundary Conditions
    - Create Displacement/Rotation Boundary Conditions in the 'Initial' Step.
9. Delete Heat Transfer Step and Create New Step
    - In the 'Create Step' dialog box, click the 'Static, General' procedure.
    - Edit the created Step
        - Where:
          Under the 'Basic' tab.
        - Value:
          Time period: Set equal to the length of the heat transfer analysis. Any other number will results in a difference of time scale, which is no problem for the simulation, but may be of inconvenience when comparing to transient experimental results.

        - Where:
          Under the 'Incrementation' tab
          Choose appropriate 'increment size' parameters. Which is highly model-dependent.
10. Edit created Step
    - Create New Predefined Field
        - Similar to Step 8 of the heat analysis procedure, create new Temperature Predefined Field.Only thermal loads are possible, select 'Body heat flux' in the 'Create Load' dialog box.
          Select the whole model to apply the load on.
        - Values:
          Distribution: From results or output database file
          File name: the heat transfer output database file (.odb-file)
          Begin step: the step you want to read out, this case: 1 Begin increment: the starting increment, from the start: 1 End step: the step you want to end on, this case only step 1 has to be used, so: 1 End increment: the ending increment, in this case we want to have all the increment of the steps, which corresponds with setting it to: 0
        - Why:
          This allows the model to read out the thermal history data from the heat transfer procedure, to calculate the mechanical behaviour due to this temperature distribution.
    - Edit Field Output Request
        - Check the desired output information for the stress analysis.
11. Create a Job

- Create the job for the stress analysis, no subroutines required for basic analysis.

12. Submit and Run the Job